The Intriguing Chemistry of NGC 6302

A thesis submitted to The University of Manchester for the degree of
Doctor of Philosophy
in the Faculty of Engineering and Physical Sciences

2014

Kerry Hebden

School of Physics and Astronomy

Contents

List of Figures

List of Tables

The University of Manchester

ABSTRACT OF THESIS submitted by Kerry Hebden
for the Degree of Doctor of Philosophy and entitled
The Intriguing Chemistry of NGC 6302. January 2014

The hostile circumstellar environment of an emerging protoplanetary nebula (PPN) and its transformation to a planetary nebula (PN) is an area of active observation and yet, many uncertainties still exist, not least in explanations of molecular abundances. Additionally, the combination of extreme radiation fields, X-rays and high velocity shocks may also drive interesting and possible novel chemical reactions and pathways. Thorough molecular surveys on PNe are minimal and in-depth modelling of specific sources to explain observed molecular abundances, are also limited in the literature. Modelling of species such as H_2O within a PN, have yet to be explored in detail at all. This thesis describes observations of NGC 6302, a young butterfly PN with possibly the highest identified central mass of any known PN (~2-3 $M_\odot$), which have recently been undertaken at the SMA. Image maps and spectra for a number of molecular species were obtained in order to provide further insights into chemical behaviour within a PN. Observational results have been compared with detailed modelling to ascertain the role of various environmental factors on the chemistry within NGC 6302. It was found that an outflow could possibly be responsible for enhanced emission for HCO^+, HCN and SiO. Species such as ^{13}CS and $^{29}SiC_2$ are also enhanced in the direction of the bi-polar lobes. N_2H^+ is confined to the dense torus, with CN also displaying little enhancement beyond the CO emission. Models suggest that whilst SO_2 is abundant in low oxygen abundances but nitrogen-enriched dense clouds, H_2O can be produced efficiently in all environments. It was also found that in standard models, H_2O reactions proceed differently to H_2O formation in dense-cloud models and circumstellar envelopes.

Declaration

I declare that no portion of the work referred to in the thesis has been submitted in support of an application for another degree or qualification of this or any other university or other institute of learning.

Copyright Statement

I find I'm so excited, I can barely sit still or hold a thought in my head. I think it's the excitement only a free man can feel, a free man at the start of a long journey whose conclusion is uncertain....

– Red, The Shawshank Redemption

Dedication

To Maya, my own little star and to Mike, for his never-failing support.

Acknowledgements

Had someone told me a few years ago, that by the time I completed my PhD i would have a 2 ½ year old daughter, I would not have believed them! But here we are and here she is! I would not have got this far without the help of many people, pre− and post−maternity leave. I would especially like to thank my supervisor for putting up with all of my daft questions/suggestions and mistakes. In no particular order, I would also like to thank the usual suspects for their help, support, cups of coffee and pints of beer over the years: Ana, Liz, Nicolas, Claire, Jenny, Czarek, Danny, Nadya, Róisin, Christina, Mark, Libby, Paul and Jaime.

And last, but by no means least, I would like to thank my family, in particular Mike and Mum & Pete for looking after Maya, whilst I completed my thesis (and for that little trip when i went observing...). Your help has made this thesis possible.

I would also like to thank STFC for funding this PhD and the Submillimeter Array for the observations obtained for this thesis. The SMA is a joint project between the Smithsonian Astrophysical Observatory and the Academia Sinica Institute of Astronomy and Astrophysics and is funded by the Smithsonian Institution and the Academia Sinica.

This thesis was typeset with LaTeX.

Supporting Publications

Chemical Evolution in NGC 6302

Hebden, K.; Fuller, G. A, Asymmetric Planetary Nebulae 5 conference, 2010

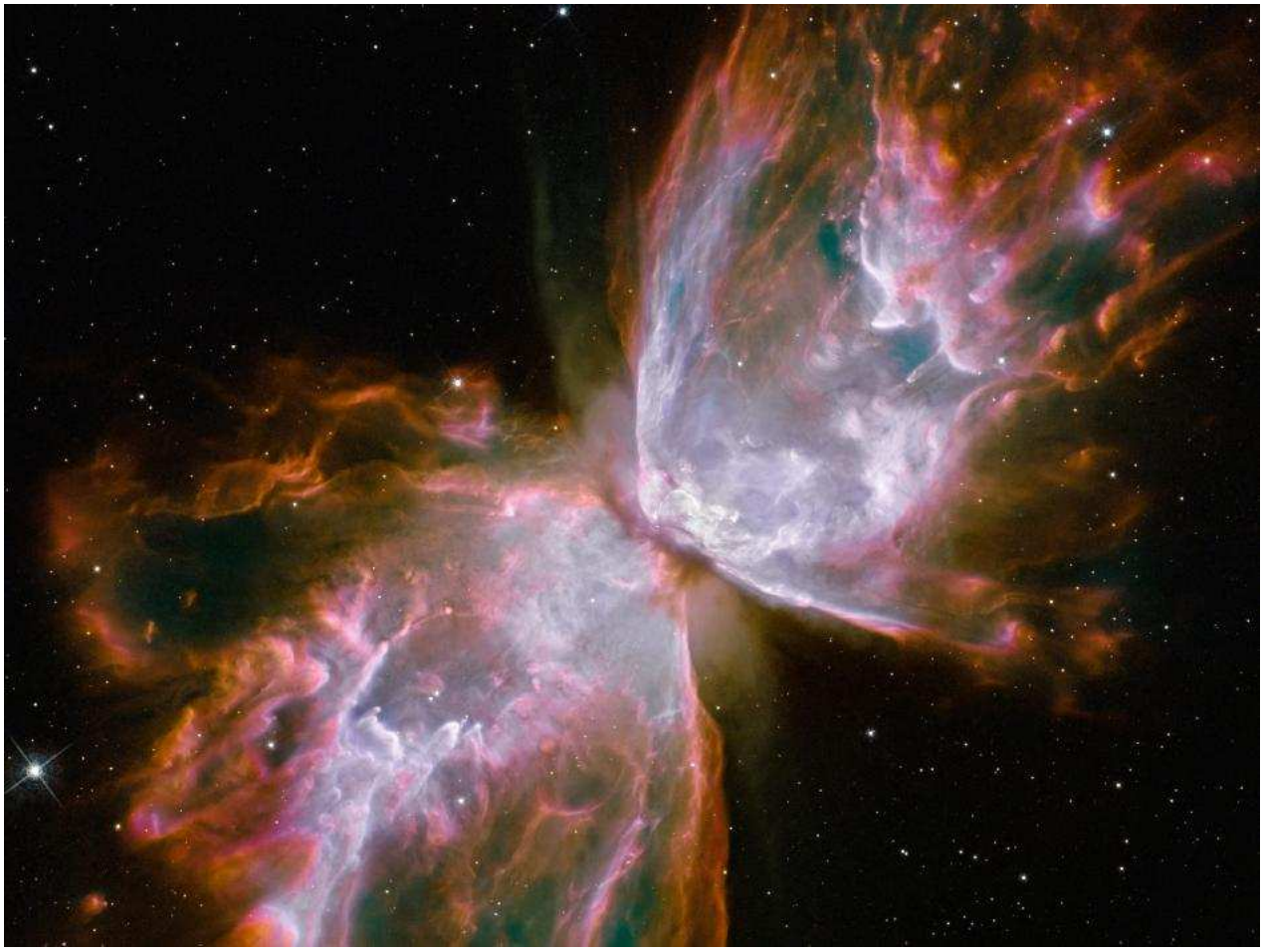

Figure 1: NGC 6302 - the Butterfly Nebula. Credit: NASA

1

Introduction

1.1 PN and their Evolution; A Brief Review

Number 27 is the name assigned to the first recorded planetary nebula (PN) observed by Charles Messier in 1764, in his catalogue of nebulous objects. Whilst Herschel first considered the idea that PN could derive their energy from a nearby star in 1791, it was over a century later before progress on the analysis of PN was made. With spectroscopy, the distinction between PNe and other gaseous clouds became more apparent, as the spectra of PN were differentiated from stellar spectra. In the optical region, spontaneous emissions from the various excited states of different ions ands atoms dominate PN spectra. This is in contrast to a stellar spectrum which (in the optical) is usually identified as a continuum with absorption lines. The broadness of the PN spectral lines were subsequently interpreted by Charles Perrine in 1929, to account for expansion of the nebula rather than rotation of the PN (Kwok 2007).

A link between red giants as the progenitors of PN, was first suggested by I Shklovsky in 1956 and expanded upon by G Abell and P Goldreich in 1966 (Kwok 2007). Shklovsky proposed that PN are an intermediate phase between red giants and white dwarfs and hence must be rapidly evolving. Using the escape velocities of red giants and the ex-

pansion velocities of PN, Abell and Goldreich supported this view, by arguing that PN are the ejected envelopes of red giants. They further suggested that given the total number of galactic PN of 6×10^4, and with a lifetime of 2×10^4 yr, that around 3 PN per year must be forming. As the number of stars leaving the main sequence is of a similar rate, Abell and Goldreich proposed that nearly all low-mass stars should go through the PN phase (Kwok 2007).

It is now established that PN represent the spectacular remnants of a low-intermediate mass star as it approaches the final phase of its existence, that of a white dwarf. The preceding asymptotic giant branch (AGB) and proto-planetary nebula (PPN) phase will shape and characterise the nebula through mass-loss, winds and photon interaction. This interaction between radiation and matter is studied within a straightforward system, as all of the energy of the nebula is derived from a single source. This can provide for intriguing domains in which to observe differing phenomena, such as photodominated regions (PDRs); created in the neutral gas via interaction with ultraviolet (UV) radiation. Nonetheless, it is the evolution of the star and its transition from AGB to PN that determines the physical and chemical conditions of the nebula and therefore whether a rich and varied chemistry is permitted in such objects.

1.1.1 In the Beginning

To progress to post main-sequence status, a star will experience a shift in hydrogen burning, whereby core hydrogen becomes depleted, whilst hydrogen shell burning around the core increases. Hydrogen burning in the shell produces helium which falls to the core, this continues to heat up and contract as its mass increases. The star now moves to the base of the red giant branch (RGB). The increasing energy outflow from the core of the star through contraction, heats the surrounding material sufficiently to continue thermonuclear reactions. The envelope of the red giant is convectively unstable, with the extent of the convective envelope reaching from near the hydrogen-

burning shell to the surface (Prialnik 2009). Mixing of the hydrogen-burning products within the envelope are transported to the surface, where abundance variations are observed along the RGB. In low-mass stars ($\lesssim 1.8$ $M_{\odot}$,), the He core is strongly degenerate. When temperatures rise sufficiently to ignite helium, the stars experience a helium flash due to the thermal instability of nuclear burning in the degenerate material. In contrast, He ignition proceeds quietly in intermediate-mass stars ($\lesssim 8$ $M_{\odot}$), when the central temperature reaches 10^8 K (Prialnik 2009). When core helium is depleted, helium burning within it subsides, quenching convection within the inner core (Prialnik 2009). Helium burning continues however in a shell at the C-O boundary.

For an intermediate-mass star, the asymptotic giant branch (AGB) stage of stellar evolution therefore consists of an electron-degenerate carbon-oxygen core which has undergone successive H and He shell burning. Devoid of energy sources, the C-O core will follow a similar evolutionary course to that of the helium core; the core will contract and heat up, resulting in an expanding, cooling envelope. The expanding star becomes redder and continues to climb up the AGB on the Hertzsprung-Russell (H−R) diagram towards higher luminosities and lower effective temperatures (Prialnik 2009).

During this phase, substantial mass loss events with rates up to $\sim 10^{-4}$ $M_{\odot}$ yr^{-1} occur due to expansion of the stars envelope, which culminates in a weakened surface gravity (Kwok 2011). The cool outer layers of giant and supergiant stars allow the coalescence of atoms into molecules, which subsequently form tiny dust particles and are accelerated by radiation pressure that drives the stellar winds. Typical wind rates are $\sim 10^{-6}$ $M_{\odot}$ yr^{-1} (Prialnik 2009). The point at which a star leaves the AGB is dependant on the intensity of the stellar wind and the envelope mass after core-helium burning. A further wind, coined the superwind, also marks the exit of life on the AGB. The superwind is key in preventing core growth from reaching its maximum potential for the AGB star, through intensive mass-loss episodes depleting the envelope mass (Prialnik 2009).

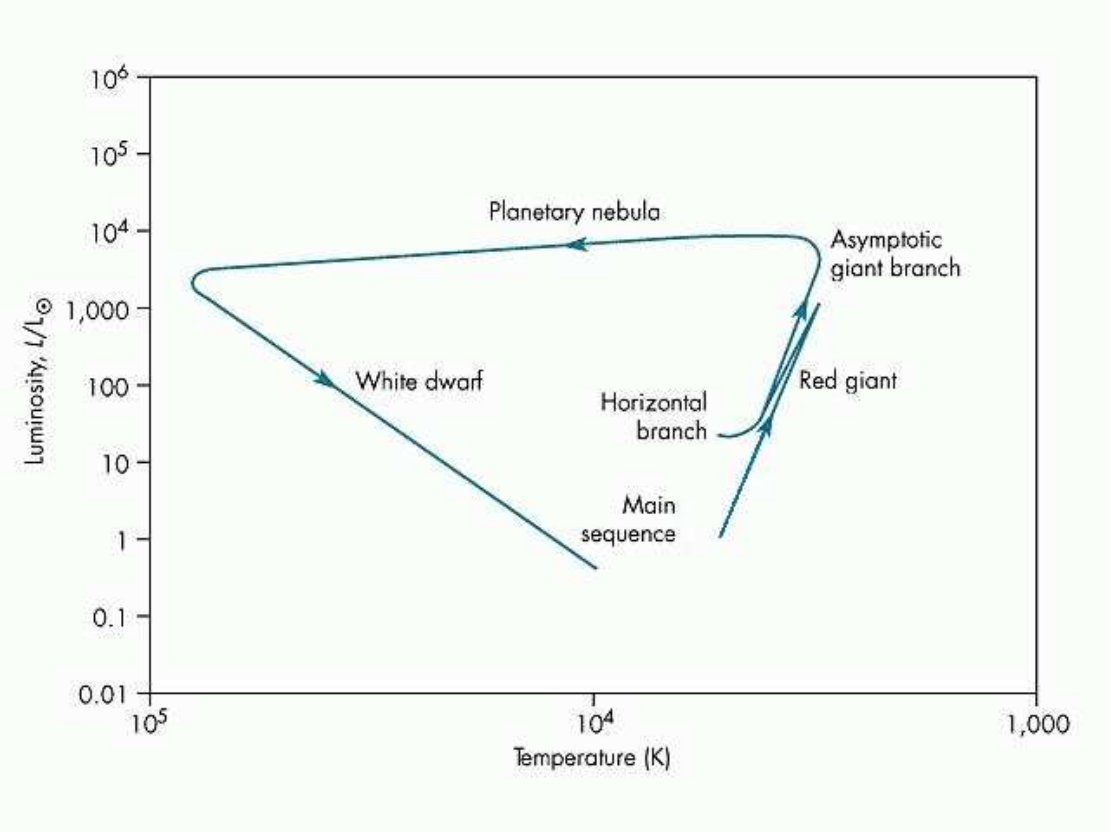

Figure 1.1: Hertzsprung-Russell diagram showing the evolution of a 3 $M_\odot$ star from zero age main sequence (ZAMS) to its final white dwarf stage. Figure from Kwok (2007).

1.1.2 In the Middle

PN are preceded by a protoplanetary nebula (PPN) phase which corresponds to the first few hundred years of the nebula's existence before it matures as a PN. What constitutes a PPN is perhaps a matter of debate, however Kwok (2007) states that observationally, a PPN should show strong infrared excesses and circumstellar CO emission. Additional PPN properties include the detachment of the dust envelope from the stellar photosphere and completion of the large-scale mass-loss phase of the AGB. PPN central stars are expected to have effective temperatures between AGB and the central star of a planetary nebula (CSPN) and hence are not hot enough to emit substantial quantities of Lyman continuum photons to ionise the remnant AGB envelope (Kwok 2007).

When the central star *is* hot enough, further mass loss produced via radiation pressure on resonance lines is initiated. The terminal velocity of wind formed as a result is higher, as the radius of the star is much smaller than it was in the earlier AGB phase. Interaction of this new high-speed wind and the residual AGB wind, sweeps up the ejected material into a shell-like structure to form the PN. The Lyman continuum photon output from the central star will significantly change as the central star rapidly evolves throughout the short-lived PN stage. The UV flux is initially absorbed by dust in the nebula and re-emitted as infrared (IR) radiation. When temperatures of the CSPN reaches $\gtrsim$ 30, 000 K, UV ionised atoms provide a pool of energy for the collisional excitation of heavy atoms such as carbon, oxygen and nitrogen via ejected electrons. Consequently, the rich emission-line spectrum observed in the visible is from spontaneous emission of the various excited states of different ions and atoms (Kwok 2007).

Continued nuclear burning removes what remains of the thinning hydrogen envelope. As such, the high temperatures required for nuclear burning can no longer be maintained when the shell decreases below a critical mass (10^{-3}–10^{-4} $M_{\odot}$). With a diminishing fuel source, the PNs lifetime is finite ($\sim 10^4$–10^5 yr) (Prialnik 2009). As the luminosity of the central star drops and the nebula disperses, the final stage for nonmassive stars culminates with ‘the cooling track’.

1.1.3 In the End

Devoid of its H/He layers, the CSPN now derives its energy from gravitational contraction, until hydrostatic equilibrium is maintained between gravitational attraction and an electron-degenerate gas pressure. Whilst a degenerate electron gas is efficient at conducting heat, its heat capacity is negligible, instead thermal energy stored by ions is responsible for the radiation emitted at the surface. The interior structure of

a white dwarf (WD) is thus of an isothermal, homogenous gas, with negligible radiation pressure which cools via electron conduction in the electron-degenerate core. An outer layer exists due to a decreasing density toward the surface, where electrons at the surface boundary cease to be degenerate (Kwok 2007). After a prolonged period of producing energy from internal heat alone, the star will eventually fade into anonymity until it becomes a black dwarf and ceases to shine.

PN, therefore, are not simply ejected AGB envelopes expanding into the surrounding interstellar medium (ISM). They are a complex mix of material from mass loss events, rearranged over a long period of time due to the interacting stellar winds. PNe are identified spectroscopically: a strong emission line spectrum with no (or very little) continuum and by morphology, which provide for stunning visual observations.

1.2 PN General Chemistry

From the AGB phase to late PN evolution, millimeter and submillimeter-wave observations have confirmed a rich, complex chemistry with the identification of over 60 different chemical compounds, including anionic species (Kwok 2011). The majority of these species have been observed in carbon-rich CSE in the prototypical carbon star IRC + 10216, however with the advent of surveys utilising instruments such as HIFI aboard the *Herschel* Space Observatory[1], oxygen-rich and S-star chemistry (C/O ~ 1) are now being examined (Justtanont et al. 2010), (Justtanont et al. 2012).

PPN/PN also harbour a variety of solid-state species, the most prevalent being amorphous silicates and silicon carbide, with aromatic species first appearing in PPN. Regardless of the intrinsic C/O ratio, all PPN and PN exhibit a strong infrared continuum (between 3 and 200 μm), often associated with the remnant dust envelope from the

[1] *Herschel* is an ESA space observatory with science instruments provided by European-led Principal Investigator consortia and with important participation from NASA

AGB phase. Often, however, spectral energy distributions (SEDs) for a higher temperature dust continuum are required to account for a 'warm' component shortward of 5 μm. An excess in emission between $2 - 5$ μm is suggested to be a product of post-AGB evolution (Kwok 2011). A number of further attributes commonly found in the infrared spectra of PPNs and PNs are; (i) Aromatic features at 3.3, 6.2, 7.7, 8.6 and 11.3 μm (ii) aliphatic features at 3.4 and 6.9 μm and (iii) unidentified broad emission features at 21 and 30 μm.

Between 1 μm and 1 cm, planetary nebula are generally optically thin, nonetheless, rotational transitions of common molecules such as CO, can produce optically thick emission lines superimposed upon the dust continuum (Kwok 2007). The rotational states of molecules have much smaller energy separations (compared with electronic states), thus transitions occur in the millimeter-wave region. For diatomic molecules, energy levels of the rotational states can be represented by the rigid body approximation $E_J = hBJ(J + 1)$, where h is the Planck constant, J is the rotational quantum number and B is the rotational constant, specified as $B = h/8\pi^2 I$ (and I is the moment of inertia). This is discussed in Chapter 4. However, the significance of molecules observed in PN implies survival beyond the onset of photoionisation.

Differing chemical species observed at each stage from post-AGB to PN, indicate that molecular synthesis is occurring within relatively short timescales of several hundred years. Speculation as to the manner of this formation is the subject of many reviews. Hasegawa et al. (2000) who modelled the neutral shell and stellar wind region of NGC 7027, state that all but H_2 and CO remain from the AGB phase (H_2 and CO both self-shield from UV dissociation) thus favouring the reformation of molecules during the PN stage. Hasegawa et al. (2000) favour a hot gas chemistry in which simple molecules such as CH, CH^+ and OH are abundantly formed at 800K. This is in contrast to a growing number of authors (see for example Huggins et al. (1992); Redman et al. (2003); Ali et al. (2001)) who prefer preservation of molecular species via inhomogeneous

clumps imaged in PN. The clumping hypothesis is also favoured by Bachiller et al. (1997) who advocates their necessity for molecular survival. The dilution of molecular material as a PN evolves is not thought to affect the density of the clumps.

A few studies have been conducted to ascertain if any chemical evolutionary trends from the AGB to PN phase are apparent (for observations see for example Bachiller et al. (1997), Josselin and Bachiller (2003), Howe et al. (1992) and Ali et al. (2001) for modelling comparisons). Bachiller et al. (1997) observed 7 objects at different stages in development (from PPN to evolved PNe), in order to determine molecular abundances and any molecular evolutionary effects. All the objects were described as having several common features including density enhancements towards an equatorial plane and C/O ratios > 1. Bachiller et al. (1997) concluded that clear trends could be discerned whereby SO, SiO, SiC_2, HC_3N and CS decrease dramatically with increasing age, suggesting that these species should not be detected in PNe. The weak or non detected emission of gaseous Si-bearing species in PN is attributed to depletion onto grains. Abundances of species such as CN, HNC, HCN and HCO^+ however, were seen to increase substantially, enhanced by photoionisation from the increasing stellar radiation (UV radiation field: $\chi \sim 10^5$ in average interstellar field units). Bachiller et al. (1997) suggest that the CN/HCN abundance ratios can be utilised as a tracer for the increasing UV radiation field, as photodissociation of HCN increases the abundances of CN.

In observations of NGC 7027, a relatively young and dense PN, by Zhang et al. (2008) detected a total of 67 spectral lines including 21 molecular lines. Zhang et al. (2008) found general agreement with these trends, such as an absence of Si bearing molecules. CS was also not detected and was suggested to have been destroyed by shocks. Zhang et al. (2008) also found a low CN/HCN ratio, which did not correlate with the theoretical expectation of HCN photodissociating into CN in a strong UV environment. Instead it was suggested that the reaction $CN + H_2 \rightarrow HCN + H$ is unexpectedly efficient

and accounts for the low CN abundances. These purported evolutionary sequences by Bachiller et al. (1997) and Zhang et al. (2008) are, however, based on observations taken from a small subset of PPN/PN, most of which are extensively studied objects.

The question of trends however, has recently been addressed by Edwards and Ziurys (2013) who have observed a number of species in the molecular-rich Red Spider Nebula (NGC 6537). Molecular species observed by Edwards and Ziurys (2013) were detected in a warm, dense gas (T_K ~60−70 K and n(H_2) ~1−8 x 10^5 cm^{-3}) and along with the usual suspects (CO, CN, HCN, HNC and HCO^+) SO, N_2H^+, CCH, H_2CO, and CS were also detected in this source. NGC 6537 bears a strong resemblance to NGC 6302; it is young ~1600 yr old, hot ($T_\star$ ~1.5 − 2.5 x 10^5 K) has a large-mass progenitor star (~ 6 $M_\odot$), and with a C/O ratio of 0.95, it is slightly oxygen-rich. Edwards and Ziurys (2013) conclude that whilst these conditions are comparable to previously studied PN (like NGC 7027), with the detection of species such as CS, SO, and H_2CO, molecular abundances do not follow an evolutionary trend, but are instead controlled by the physical and chemical properties of the PN and its progenitor star.

1.3 PN Environments: PDRs, XDRs and Shock Fronts

Photon-dominated regions (PDRs), which can also be defined as photo-dissociation regions, are broadly recognised as neutral regions where far-ultraviolet (FUV; 6 – 13.6 eV) radiation dominates the gas heating and thus determines the chemical complexity (Tielens and Hollenbach 1985). Whilst initially associated with regions separating molecular and ionised gas near hot young O and B stars, PDRs are now associated with many interstellar environments, including PNe, as FUV radiation from the central star is the controlling heat source. Within a PDR, dust absorption and scattering limit the FUV photon penetration depth, whilst photoelectric emission of electrons from grain surfaces primarily heats the gas.

Photopumping of H_2 in the atomic zone is another important heating mechanism within a PDR. Absorption of an FUV photon followed by radiative decay can leave H_2 with excess vibrational energy, which is subsequently emitted as a near-IR photon. Equivalently, collisions with other species can de-excite the molecule thus heating the gas. Cooling occurs predominantly via abundant atomic and ionic fine-structure lines such as [CII] 158 μm line and [OI] 63μm (Tielens and Hollenbach 1985). The framework of a PDR is represented by a layered structure of differing chemical zones and is illustrated schematically in Fig 1.2. PDRs are thus primarily characterised by a thin (Δ A_V < 0.1) transition zone where the penetrating FUV photons ionise hydrogen to create a HII/HI interface. Photons with energies less than 13.6 eV will ionise carbon and dissociate H_2. At around $A_V \simeq 2$, H_2 self shielding occurs followed by a rapid transition from H to H_2 with H_2 dominating the composition. Deeper within the cloud, ionised carbon recombines to form CO when the carbon-ionising flux drops sufficiently. Recombination of O_2 occurs at greater depths in the cloud.

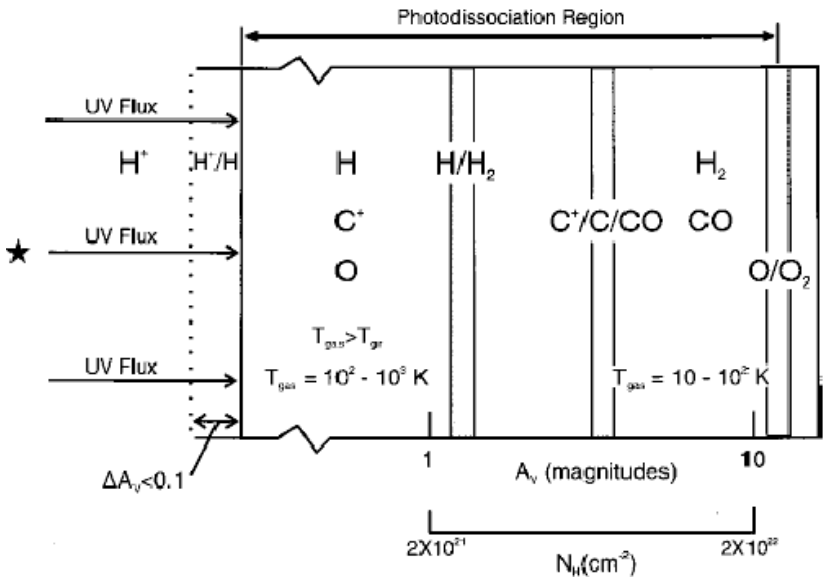

Figure 1.2: Schematic interpretation of the structure of a photon dominated region (PDR). The PDR extends from the H^+/H transition region through to the O/O_2 boundary. Adapted from Tielens (2005).

X-ray dominated regions (XDRs) on the other hand, are dominated by keV X-rays which control the gas heating and chemistry. However in an XDR, photons are attenuated less easily and it is photoionisation of heavy elements rather than dust particles that limit penetration (Sternberg 2005). XDRs are typically prominent near intense X-ray sources such as active galactic nuclei (AGN) or PNe with hot central stars. 'Hot bubbles', jets and collimated outflows, phenomena prevalent in PNe, are also potential sources of diffuse X-Rays and have been identified in recent PNe X-ray surveys by the Chandra X-ray Observatory and XMM-Newton (Kastner 2007). Gas in the rim of these hot bubbles is shocked and superheated as a result of the collision between the remnant ejected AGB gas and the fast wind of the evolving white dwarf and subsequently driven out at supersonic speeds forming an overpressurised bubble. A handful of PNe have also been observed with diffuse X-rays emanating from collimated outflows and jets. Despite the scarcity of these types of PNe, they have been attributed with potential molecule-rich, dusty central tori; a possible location for the confinement and channelling of X-ray emitting outflows and associated shocks (Kastner 2007).

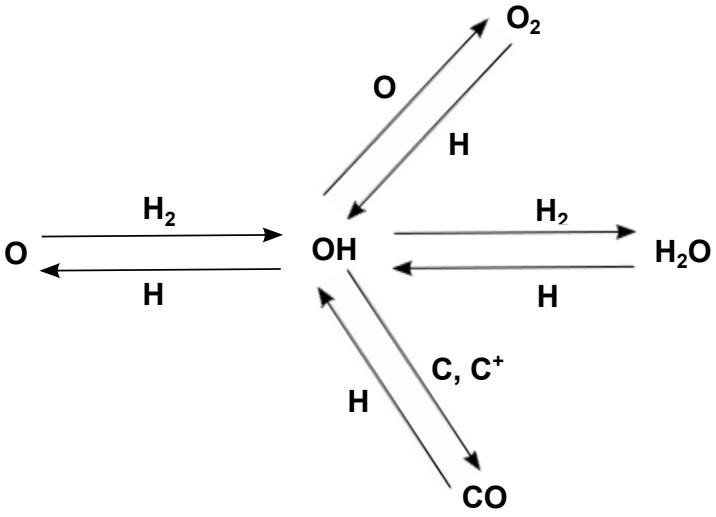

Figure 1.3: Important reactions involving carbon and oxygen in shock chemistry. Figure adapted from Tielens (2005).

In a series of recent papers by Meijerink and Spaans (2005) (see also Meijerink et al. (2006) and Meijerink et al. (2007)) the authors implement a number of models to differentiate between PDRs and XDRs and between XDRs and cosmic ray irradiated gas and discuss chemical differences between these environments. For the first scenario (PDRs versus XDRs) the code is implemented for a semi-infinite slab geometry which is irradiated from one side. An elaborate chemistry is used utilising reaction rates from the UMIST database[2], (excluding photo-ionisation rates for XDRs) with treatment of H_2 formation, destruction and excitation and the addition of reactions with PAHs. It is assumed that ionisation from X-ray photons leads to double-ionised species through the ejection of an Auger electron, thus species such as C^{2+}, N^{2+}, S^{2+}, O^{2+} and Fe^{2+} are included in the chemistry. For full details of the chemistry, heating and cooling processes, see the appendix in Meijerink and Spaans (2005).

In direct comparison between the PDR and XDR models, Meijerink and Spaans (2005) found a number of differences between the two. For instance in the PDR models CH^+ and CH_2^+ are more abundant than their neutral counterparts CH and CH_2, whilst conversely, the reverse is true for XDR models. Similarly CN is three orders of magnitude more abundant than CN^+ in XDRs, whereas for PDRs both species are equally abundant. In general, abundances of neutral and ionised species at the cloud edge are enhanced in XDRs compared with PDRs. It is noted by the authors that the thermal structure in XDRs are more gradual compared with a stratified structure seen in PDRs. As a result, the transition from atomic to molecular hydrogen and of C^+ to C and CO are smoother compared to PDRs.

At the cloud edge in PDR models all carbon is in C^+, whilst in XDR models carbon in this region is largely neutral. Meijerink and Spaans (2005) conclude that column density ratios for select species provide good PDR/XDR discriminators. For example, XDRs show larger ratios for HOC^+/HCO^+ ranging from 10^{-4} ($n \sim 10^6$ cm^{-3}) to 0.6 (n

[2]http://www.udfa.net/

$\sim 10^4$ cm^{-3}) whereas the ratios range from 10^{-7} to 10^{-5} for PDRs. Similarly NO/CO column density ratios in XDRs are 10^{-4} ($n \sim 10^6$ cm^{-3}) to 10^{-3} ($n \sim 10^4$ cm^{-3}) compared to 10^{-6} to 10^{-5} for PDRs. Whilst the models are constructed to be representative of conditions in galactic centres, the irradiation conditions are typical for PDRs like the Orion Bar and so useful comparisons can be made with environments in PNe.

Shocks are produced when the bulk fluid velocity of a gas exceeds the local sound velocity. The resulting supersonic compression produces a shock wave which heats and compresses the gas. The sound speed in neutral interstellar gas is only 0.3 km s^{-1} at $T = 10$ K and rises to 1 km s^{-1} at $T = 100$ K, consequently many interstellar phenomena such as bi-polar outflows from proto-stars and expanding HII regions (30 to 200 km s^{-1} and $\gtrsim 10$ km s^{-1} respectively) surpass this velocity (Kellermann and Verschuur 1988). The wind speeds of CSPN are observed to be much higher than the sound speed, which, if cooling is not efficient, can produce very high temperature gas in the postshock region.

Shocks can have an intriguing effect on chemistry, which can proceed rapidly in the hot shock-heated gas. Water for example is expected to be highly abundant, as all available oxygen is expected to form water in post-shock gas above 250 K. This is demonstrated by Draine et al. (1983) who through modelling shocks in molecular clouds, show that H_2O is not especially abundant in pre-shock gas, however, at densities $n_H \gtrsim 10^4$ cm^{-3} and with shock speeds $v_s \gtrsim 10$ km s^{-1} endothermic reactions with O and OH rapidly produce H_2O, which also acts as a major coolant.

Carbon as well as oxygen is of particular importance in shocked gas as the elevated temperatures allow for reactions to proceed with considerable activation barriers (0.1 − 1 eV). Figure 1.3 summarises the C and O chemistry involved in these reactions. The OH produced in Fig. 1.3 can also react with atomic sulphur to produce SO and SO_2 and with silicon, if present, to form SiO. SiO is frequently observed in the Galactic

centre region (for example see Martin-Pintado et al. (1997)) and its association with areas of high temperatures and outflows suggest that the dominant mechanism for releasing SiO into the gas phase, is through grain erosion and destruction (Huettemeister et al. 1998). Upon cooling of the shocked gas, chemistry typically evolves to that of dark clouds and is dominated by ion-molecule reactions.

1.4 NGC 6302

NGC 6302 is a relatively young PN showing a strong symmetric (butterfly) morphology, which harbours a massive expanding torus oriented in the north-south direction, the front of which is coincident with a dark absorption lane. This dark equatorial lane separates two huge bipolar lobes perpendicular to the central dense structure, which has a significant extinction gradient running north to south (Matsuura et al. 2005). The lobes exhibit high velocity knots (> 20 km s^{-1}) within a complex but somewhat fragmented structure and the system as a whole is inclined at an angle of $\sim 45^{\circ}$ with respect to the line of sight. It is surmised to be one of the highest ionised known PN, with a central star temperature of $> 200,000$ K (Casassus et al. 2000). Until recently, its central star had remained hidden behind the dense dust and molecular disk of the PN (Szyszka et al. 2009).

The kinematics and mass loss and evolution of NGC 6302 has been thoroughly discussed by Peretto et al. (2007), Dinh-V-Trung et al. (2008) and Wright et al. (2011). Through analysis of the CO emission, Peretto et al. (2007) determine an expansion velocity of the central torus of 8 km s^{-1} and further imply that expansion of the nebula was initiated $\sim$ 7500 years ago. With an apparent width of the torus at 8000 AU, the expansion event is surmised to have ended $\sim$ 2900 years ago and thus lasted for $\sim$ 4600 years. These timescales assume that the apparent inner edge of the torus marks the final ejection event and that the CO emission traces the complete ejected material. Using RADEX to constrain the abundance ratios of ^{12}CO and ^{13}CO, Peretto et al.

(2007) construct a number of models to subsequently infer a total torus mass of $\sim 2\ M_{\odot}$ $\pm\ 1\ M_{\odot}$. This contrasts somewhat with CO observations by Dinh-V-Trung et al. (2008) who suggest a total molecular gas mass of $0.1\ M_{\odot}$ with an overall total gas mass of $\sim$ $0.5\ M_{\odot}$. The CO observations of both authors are discussed in more detail in Chapter 5.

Based on the torus mass and the current mass of the central star, Peretto et al. (2007) infer a lower limit of $3\ M_{\odot}$ for the progenitor star. This is consistent with the calculations of Casassus et al. (2000) who estimate the progenitor mass to be $4{-}5\ M_{\odot}$. Following on from these assumptions Peretto et al. (2007) subsequently infer average mass-loss rates of 5×10^{-4} $M_{\odot}$ yr^{-1}. This complements mass loss rates from other authors which vary from $\sim 1.5 \times 10^{-4}$ $M_{\odot}$ yr^{-1} Dinh-V-Trung et al. (2008) to $\sim 7 \times 10^{-4}$ $M_{\odot}$ yr^{-1} Matsuura et al. (2005). The distance to NGC 6302 has been debated by many authors and has been estimated to range from 0.15 to 2.4 kpc. However in recent papers a distance of 1 kpc has been adopted by Kemper et al. (2002), Meaburn et al. (2005), Matsuura et al. (2005), and more recently by Dinh-V-Trung et al. (2008), with studies of its proper motion and emission-line photometry used to constrain the distance.

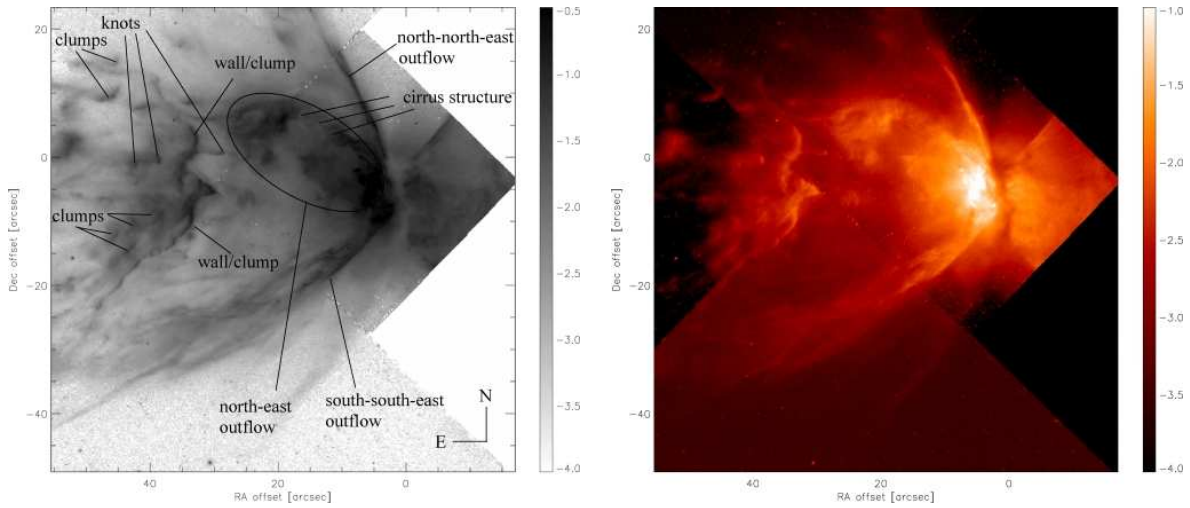

(a) Schematic representation of NGC 6302 (b) HST image of NGC 6302

Figure 1.4: (a) Schematic view of the outer region of NGC 6302 (overlaid on the HST F658N image). (b) HST WFPC2 image before distortion corrections (in the F656N band, λ_0 = 6564 Å, $\Delta\ \lambda_0$ = 21.5 Å). All images from Matsuura et al. (2005).

1.4.1 NGC 6302 Chemistry

NGC 6302 has been observed a number of times at a number of different frequencies, but a comprehensive molecular survey, along with any modelling to analyse the chemistry, has never been published. NGC 6302 has been observed by Aller et al. (1981) (λ 1200−3203 and λ 3200−4880 Å), (Payne et al. 1988) (OH maser emission), Ashley and Hyland (1988) ([SiVI][SiVII]) Huggins et al. (1996) (CO), Beintema and Pottasch (1999) (2.4 − 45 μm), Molster et al. (2001) (2.4 − 197 μm), Kemper et al. (2002) (dust and PAHs), Matsuura et al. (2005) (Hα, [NII], Brα and PAHs), Peretto et al. (2007) (CO) and most recently by Dinh-V-Trung et al. (2008) (CO) and Bujarrabal et al. (2012) (H_2O and OH).

Atomic abundances in NGC 6302 have been deduced by number of authors, with thorough reviews by Aller et al. (1981), Pottasch and Beintema (1999) and Casassus et al. (2000). Although a factor or two in abundances may be disputed between authors, it is generally agreed that NGC 6302 is an O−rich nebula with enhancements in nitrogen

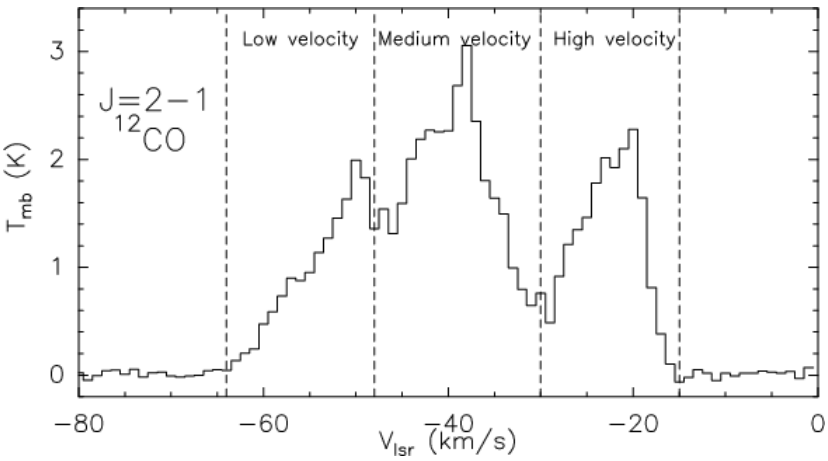

(a) CO velocity structure

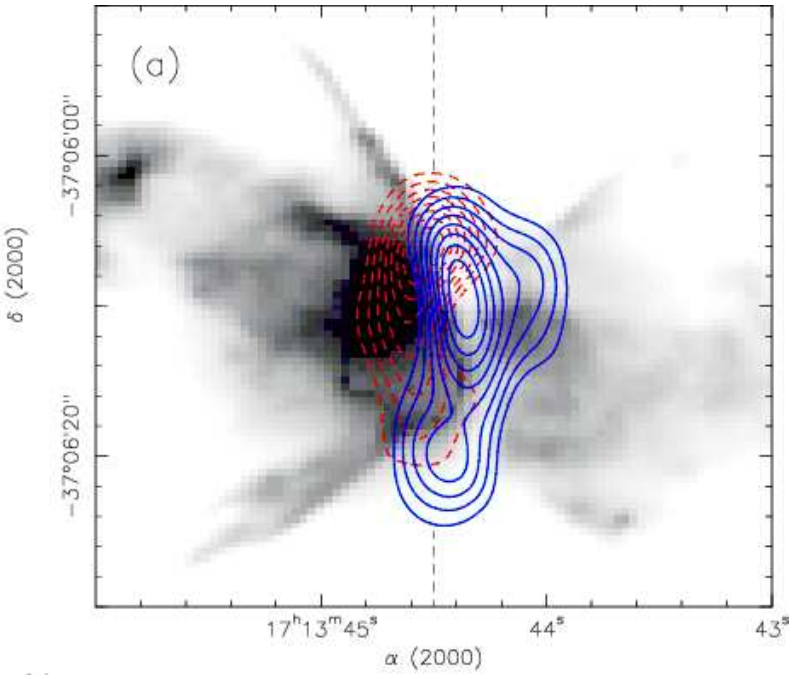

(b) Medium and high velocity components of NGC 6302

Figure 1.5: (a) CO velocity structure showing the low, medium and high velocity components respectively and (b) the Hα map (grey scale) overlaid with SMA observations of ^{13}CO J = 2 $\rightarrow$ 1 medium and high velocity components (blue contours and red-dashed contours respectively) from Peretto et al. (2007).

and helium. Indeed in the data obtained by Aller et al. (1981) via the International Ultraviolet Explorer satellite (IUE) and the Anglo-Australian telescope, the nitrogen enrichment is an order of magnitude greater than in a typical PN. Aller et al. (1981)

also suggest that sodium and potassium have average values, whilst chlorine is slightly enhanced and argon is moderately enhanced. Calcium, and possibly silicon, are suggested to be incorporated in grains and sulphur is reported to be depleted by a factor of 2. Table 4 in Aller et al. (1981) summarises the composition of NGC 6302 compared to solar and mean planetary values.

Further contributions to atomic abundances are provided by Casassus et al. (2000) who, through observations of NGC 6302 coupled with subsequent modelling using CLOUDY, detail gas-phase depletions of a number of elements. Casassus et al. (2000) state that aluminium is depleted to one hundredth of the solar value, neon is overabundant whilst magnesium is about half solar value and titanium is strongly depleted. Dust species such as perovskite ($CaTiO_3$) and corundum (Al_2O_3) are attributed to the depletion of Al and Ti. C/O ratios of 0.20 (Aller et al. 1981), C/O = 0.26 (Pottasch and Beintema 1999) and C/O = 0.43 (Wright et al. 2011) have also been suggested, thus attesting to the O−rich nature of NGC 6302.

The ISO[3] observations by Molster et al. (2001) comprehensively covers a broad wavelength range. In the region from 2.4 to 17 μm, the continuum-subtracted spectrum is characterised by C-rich dust features, whilst at longer wavelengths O-rich dust dominates the spectrum. Interestingly, in Figure 2 of Molster et al. (2001) broad crystalline H_2O ice is present. Water ice displays a number of distinct spectral features at infrared wavelengths, including 3 μm (O−H stretch) often seen in absorption (Dijkstra et al. 2006) and strong bands at 43 μm, 62 μm and a weak shoulder feature at 52μm. These latter features, namely 43, 52 and 62μm are all present in NGC 6302, thus Molster et al. (2001) suggest that although these features are likely blended with diopside and possibly a minor contribution from enstatite, the identification of all these features provides a robust detection for crystalline water ice in NGC 6302. The identification of

[3]ISO is the Infrared Space Observatory utilising the Short Wavelength (SWS) and Long Wavelength (LWS) spectrometers (2.4-197 μm)

water in gas form has recently been discussed by Bujarrabal et al. (2012) who present the latest observations of NGC 6302 using *Herschel*/HIFI. Confirmed detected species along with H_2O, include ^{12}CO and ^{13}CO, OH and NH_3.

Spectra obtained by Bujarrabal et al. (2012) of NGC 6302 are reminiscent of the detailed analysis of the CO structure observed by Peretto et al. (2007), with both authors consequently presenting spectra characterised by a central line core with wide 'wings'. However, the identification of the central line core, described as emission from the fossil, remnant AGB envelope, and those of the wings, suggested to be emission from the fast bi-polar outflows, are distinguished differently by the respective authors. Peretto et al. (2007) identify three broad velocity components at -64 to -48 km s^{-1} for the low velocity component, -48 to -30 km s^{-1} for the medium velocity component and -30 to -15 km s^{-1} for the high velocity component. Figure 1.5a, displays the averaged ^{12}CO J = 2 $\rightarrow$ 1 spectrum obtained by Peretto et al. (2007) with the SMA, integrated over the full spatial extent of the source. Bujarrabal et al. (2012) on the other hand, describe the blue wing component at -53 to -48 km s^{-1} as the high-velocity molecular gas, whilst the line core ranges from -25 to -20 km s^{-1} and represents the unaccelerated remnant of the AGB shell. Comparison of observed species in NGC 6302 is discussed thoroughly in Chapter 3.

1.5 Overview

PNe have provided fascination to all who have observed them since their initial discovery. Whilst there is not a standard accepted definition of what constitutes a PN, two features are clear; at the very basic level, PN contain an ionised circumstellar shell, surrounding a hot compact star as it evolves from the AGB to WD phase. However, answers to many aspects of this short evolutionary period remain incomplete; How does the interaction of binary stars, for example, affect PN formation? Even the processes which create the many morphologies seen in PN, are not fully understood.

Without doubt, surveys containing a large representative of sources, can help to constrain phenomena to a subset of PNe. In the recent X-ray survey by Kastner et al. (2012) for instance, the authors found that the presence of X-rays within PN, appears correlated with density structure. Kastner et al. (2012) suggest that molecule-poor, elliptical nebulae are more likely to display X-ray emission, than PN with bipolar and ring-like morphologies which are molecule-rich. Molecular emission surveys, such as those by Bujarrabal et al. (2012) utilising *Herschel*/HIFI, are advancing our understanding of PNe chemistry, with species such as H_2O now being identified in a number of objects. Nonetheless, the importance of extensive observations on singular objects should not be underestimated.

To date, only a few PN (and PPN) have been extensively studied in the millimetre regime and had their molecular content examined thoroughly. NGC 7027 and most recently NGC 6537, are two such PN which have been comprehensively observed by Zhang et al. (2008) and Edwards and Ziurys (2013) respectively. Nevertheless, there is still a lack of PN with in-depth, high spatial resolution observations. The identification of objects with enhanced equatorial regions or central torii are ideal candidates in which to analyse molecular chemistry and to test models of the interaction of UV photons (and X-rays) with molecular gas in extreme environments. One such object harbouring a dense, central torus is NGC 6302.

From the many observations to date, nebular abundances robustly indicate that NGC 6302 is typically of the Type 1 classification that has been assigned to it. Type 1 PN are thought to evolve from massive progenitors (> 2.4 $M_{\odot}$), have higher abundances of nitrogen and helium and are often characterised as displaying a bipolar morphology (Peimbert and Torres-Peimbert 1983). The massive progenitor has been discussed by a number of authors including Casassus et al. (2000) and Peretto et al. (2007). Through gas phase modelling of N/O and C/O, Casassus et al. (2000) state that the abundance

ratios are consistent with a progenitor main-sequence mass of ~4−5 $M_{\odot}$.

The nitrogen abundance was also investigated through modelling of the N/H ratio by Wright et al. (2011). The authors conclude that their derived N/H ratio is too large to account for nitrogen production by secondary conversion of initial carbon. Wright et al. (2011) state that the primary enrichment of nitrogen occurred via third dredge-up of carbon, followed by hot-bottom burning (HBB) conversion of carbon to nitrogen (via the CN cycle). Molster et al. (2001) state that subsequent thermal pulses can change the surface C/O ratios between O-rich and C-rich, thus allowing both types of grains (PAHs and silicates) to be present in the evolving nebula without the need for rigid O or C-rich boundaries. Such a mixed chemistry has been identified in NGC 6302, nonetheless, stratification of O-rich and C-rich material does seem apparent. PAH emission observed by Matsuura et al. (2005) for example, appears primarily confined to the lobes (however it is noted by the authors that PAH emission requires excitation by UV and/or optical photons, little of which penetrates the dark lane). Analysis of the mineral composition by Kemper et al. (2002) on the other hand, suggests that oxygen-rich material, which makes up the bulk of the mass, is predominantly located in the circumstellar torus.

As thorough investigations into the evolutionary, kinematic and atomic features of NGC 6302 have been conducted, this thesis aims to shed light on the molecular characteristics of the central torus of NGC 6302. The analysis will hence determine if the environmental properties drive novel chemical reactions and pathways and whether properties such as the nitrogen-rich element of the nebula, has a distinguishing effect on the molecular chemistry. The observations and detailed study will consequently add to the limited number of in-depth analyses currently available for PN. The following analysis is structured as such; Chapter two describes interferometry, with elements of the Submillimeter Array (SMA) used for observations of NGC 6302, whilst Chapter three presents the images and spectra obtained with the SMA. Chapter four details the

CN radical and its associated hyperfine structure, used to obtain opacity of the line for column density calculations. Column densities for the species observed are also described here. Chapter five explains the Meudon PDR code utilised in modelling column densities in NGC 6302 and details the various models developed to mimic certain environments within NGC 6302. Chapter six summarises all of the work undertaken in this thesis and also discusses future work.

2

Interferometry

The data in this work was taken using the Submillimeter Array (SMA)[1]. This chapter reviews the key techniques and principles of interferometry and aperture synthesis.

2.1 Interferometry Basics

Sensitivity and angular resolution are the two basic requirements of a radio telescope, with sensitivity depending on total collecting area and angular resolution of a radio telescope defined as $\theta \sim \lambda/\mathrm{D}$, where λ is the wavelength of the received radiation, D is the diameter of the telescope and θ is the angular resolution. Put simply, if two sources are closer together than this angle, then they cannot be resolved. As a single-aperture radio telescope is ill-equipped to provide the resolution needed for radio observations, interferometers are required.

The principal features of a simple two dish interferometer, separated by a baseline vector **b** is illustrated in Figure 2.1. The signals received by the antennas are considered to be planar waves i.e the source is sufficiently distant so that the incident wavefront

[1]The Submillimeter Array is a joint project between the Smithsonian Astrophysical Observatory and the Academia Sinica Institute of Astronomy and Astrophysics and is funded by the Smithsonian Institution and the Academia Sinica. http://www.cfa.harvard.edu/sma/

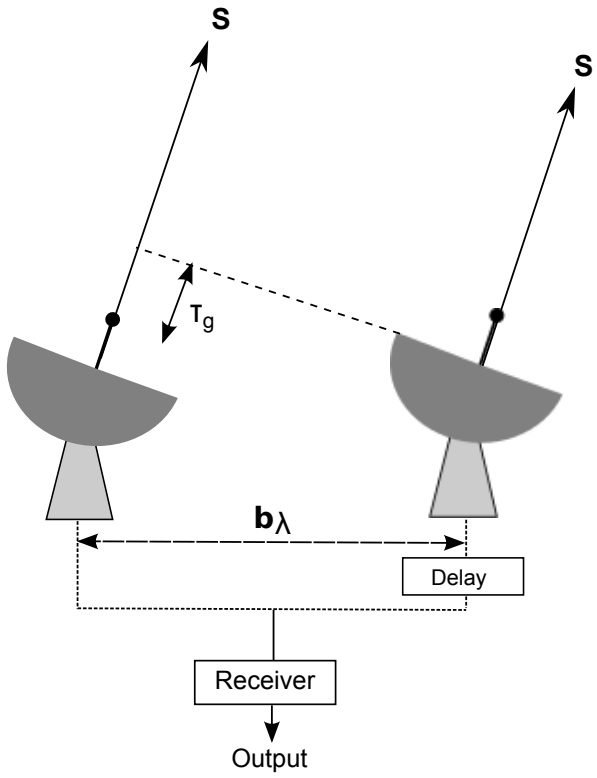

Figure 2.1: A schematic of a simple two dish interferometer. Based on Burke and Graham-Smith (2002).

arriving at the telescopes is considered to be a plane over the distance b. The wavefront arrives at the right-hand antenna at a time τ_g defined as the geometric time delay,

$$\tau_g = \mathbf{b} \cdot \mathbf{s}/c \tag{2.1}$$

where c is the velocity of light, before it reaches the left-hand antenna and **s** is the vector in the direction of the source (Burke and Graham-Smith 2002). The received signals from the antennas, $V_1(t)$ and $V_2(t)$, are combined and amplified by a voltage multiplier and time averaging is performed, resulting in an output proportional to $\langle V_1(t) \quad V_2(t) \rangle$. For signals received from a monochromatic source, the signals can be represented as $V_1(t) = v_1 \cos 2\pi\nu(t - \tau_g)$ and $V_2 = v_2 \cos 2\pi\nu t$. These signals which are then input into a correlator, yielding an output of

$$r(\tau_g) = \mathrm{v}_1\,\mathrm{v}_2 \cos 2\pi\,\nu\,\tau_g, \tag{2.2}$$

where $\mathrm{v}_1\mathrm{v}_2$ represents the fringe amplitude and is proportional to effective antenna area, A(s) and the source flux, S (Perley et al. 1986). The output can now be expressed in terms of source brightness, I(s), integrated over the sky in direction **s**. The correlator output for the signal power received in solid angle $d\Omega$ and in bandwidth $\Delta\nu$ is thus represented as,

$$dr = A(s)\,I(s)\,\Delta\nu\,d\Omega\,\cos 2\pi\,\nu\,\tau_g. \tag{2.3}$$

Rearranging in terms of source position and baseline vectors, results in,

$$r = \Delta\nu \int_S A(s)\,I(s) \cos\frac{2\pi\nu b\cdot s}{c}\,d\Omega \text{ becomes } r = \Delta\nu \int_S A(s)\,I(s) \cos 2\pi\, b_\lambda \cdot s\,d\Omega \tag{2.4}$$

where $\mathbf{b}_\lambda = \mathbf{b}/\lambda$, a simplification entailing the measurement of the baseline vector in wavelengths (Burke and Graham-Smith 2002).

In order to take an interferometric image of a source, a reference direction, $\mathbf{s}_0$, also called a *phase tracking centre* is utilised. This position vector becomes the centre of the field to be mapped and the direction to the source in respect to this position is given as $\mathbf{s} = \mathbf{s}_0 + \boldsymbol{\sigma}$, where $\boldsymbol{\sigma}$ is the vector from the phase tracking centre to the source element of solid angle dΩ (Perley et al. 1986). This is shown schematically in Figure 2.2. As $\mathbf{b}_\lambda$ is the baseline measured in wavelengths, so $\nu\tau_g = \mathbf{b}_\lambda \cdot \mathbf{s} = \mathbf{b}_\lambda \cdot (\mathbf{s}_0 + \boldsymbol{\sigma})$, then,

$$\begin{aligned} r &= \Delta\nu \int A(\boldsymbol{\sigma})I(\boldsymbol{\sigma}) \cos[2\pi\mathbf{b}_\lambda \cdot (\mathbf{s}_0 + \boldsymbol{\sigma})]d\Omega \\ &= \Delta\nu\,\cos(2\pi\,\mathbf{b}_\lambda \cdot \mathbf{s}_0) \int A(\boldsymbol{\sigma})\,I(\boldsymbol{\sigma})\,\cos(2\pi\,\mathbf{b}_\lambda \cdot \boldsymbol{\sigma})\,d\Omega \\ &- \Delta\nu\,\sin(2\pi\,\mathbf{b}_\lambda \cdot \mathbf{s}_0) \int A(\boldsymbol{\sigma})\,I(\boldsymbol{\sigma})\,\sin(2\pi\,\mathbf{b}_\lambda \cdot \boldsymbol{\sigma})\,d\Omega \end{aligned} \tag{2.5}$$

The fundamental equation for a practical interferometer however is that of the complex visibility, whereby the amplitude and phase of the visibility are the primary measurements. With the introduction of a normalised antenna reception pattern $A(\boldsymbol{\sigma}) = A(\boldsymbol{\sigma})/A_0$, the complex visibility of the source is defined as,

$$V \equiv |V| e^{i\,\phi\,V} = \int A(\boldsymbol{\sigma})\, I(\boldsymbol{\sigma})\, e^{-i2\pi \mathbf{b}_\lambda \cdot \boldsymbol{\sigma}}\, d\Omega \tag{2.6}$$

where A_0 is the beam centre antenna response (Perley et al. 1986). Then, by separating the real and imaginary parts of V, the following is obtained,

$$A_0\,|V|\,\cos\phi_V = \int A(\boldsymbol{\sigma})\, I(\boldsymbol{\sigma}) \cos(2\,\pi\,\mathbf{b}_\lambda \cdot \boldsymbol{\sigma})\, d\Omega \tag{2.7}$$

and

$$A_0\,|V|\,\sin\phi_V = -\int A(\boldsymbol{\sigma})\, I(\boldsymbol{\sigma}) \sin(2\,\pi\,\mathbf{b}_\lambda \cdot \boldsymbol{\sigma})\, d\Omega. \tag{2.8}$$

Finally, substitution of equations 2.7 and 2.8 into 2.5, gives the output of the correlator as,

$$r = A_0\,\Delta\nu\,|V|\,\cos(2\pi\,\mathbf{b}_\lambda \cdot \mathbf{s}_0 - \phi_V) \tag{2.9}$$

The output can hence be expressed in terms of a fringe pattern corresponding to $\mathbf{s}_0$, the phase reference position. The measured visibility, V, is a Fourier amplitude/phase, the inversion of which is used to obtain the sky brightness distribution (Perley et al. 1986).

2.1.1 The *uv*-plane

It is practical to apply a coordinate system for the synthesis of an interferometric map (or image) of a source to obtain its position. The baseline vector **b** is decomposed into coordinates u, v and w, corresponding to the east-west, north-south and up-down directions respectively. The offset vector $\boldsymbol{\sigma}$ can similarly be decomposed into complementary coordinates, l, m and $\sqrt{1 - l^2 - m^2}$, representing u, v and w respectively. As,

$$\mathbf{b}/\lambda \cdot \boldsymbol{\sigma} = \mathrm{ul} + \mathrm{vm} + \mathrm{w}\sqrt{1 - l^2 - m^2}, \tag{2.10}$$

the complex visibility becomes,

$$V_{u,v,w} = \int\int A(l,m)\, I(l,m)\, e^{-i2\pi(ul+vm+w\sqrt{1-l^2-m^2})}\, dl\, dm \tag{2.11}$$

Thus, for each point on the sky, the visibility is described by a phase term defined by the sky coordinates l, m and $\sqrt{1 - l^2 - m^2}$ and a function of the baseline u, v and w (Burke and Graham-Smith 2002).

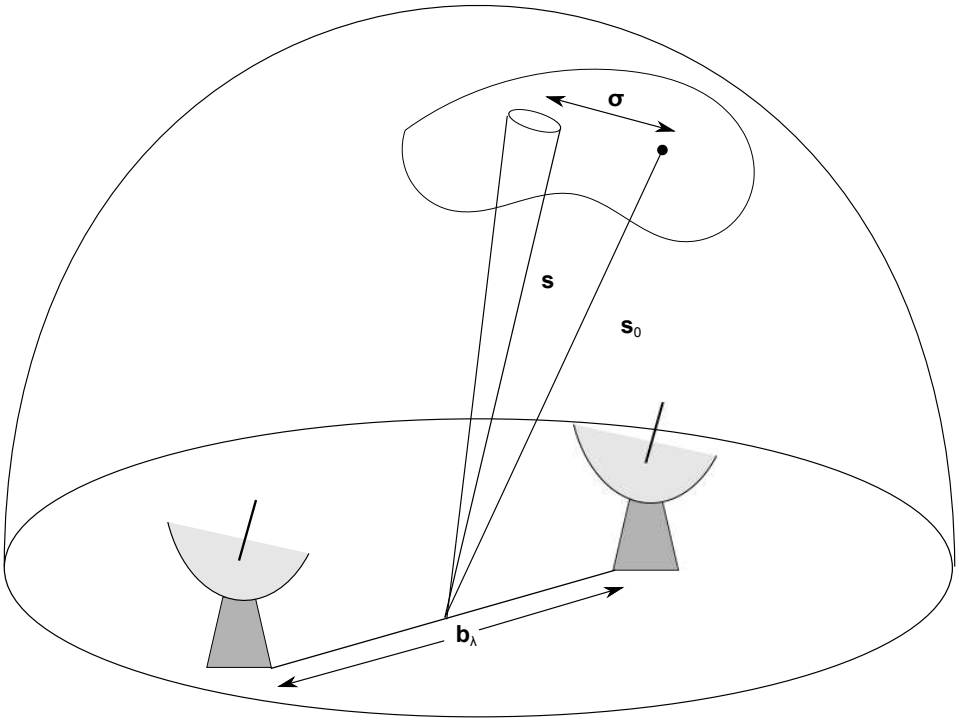

Figure 2.2: The geometry of a two element interferometer showing the radiation received from a small element, subtending a solid angle dΩ of an extended radio source, in a direction **s**. $\boldsymbol{\sigma}$ defines the vector from the phase tracking centre, $\mathbf{s}_0$, to the source element. Based on Burke and Graham-Smith (2002).

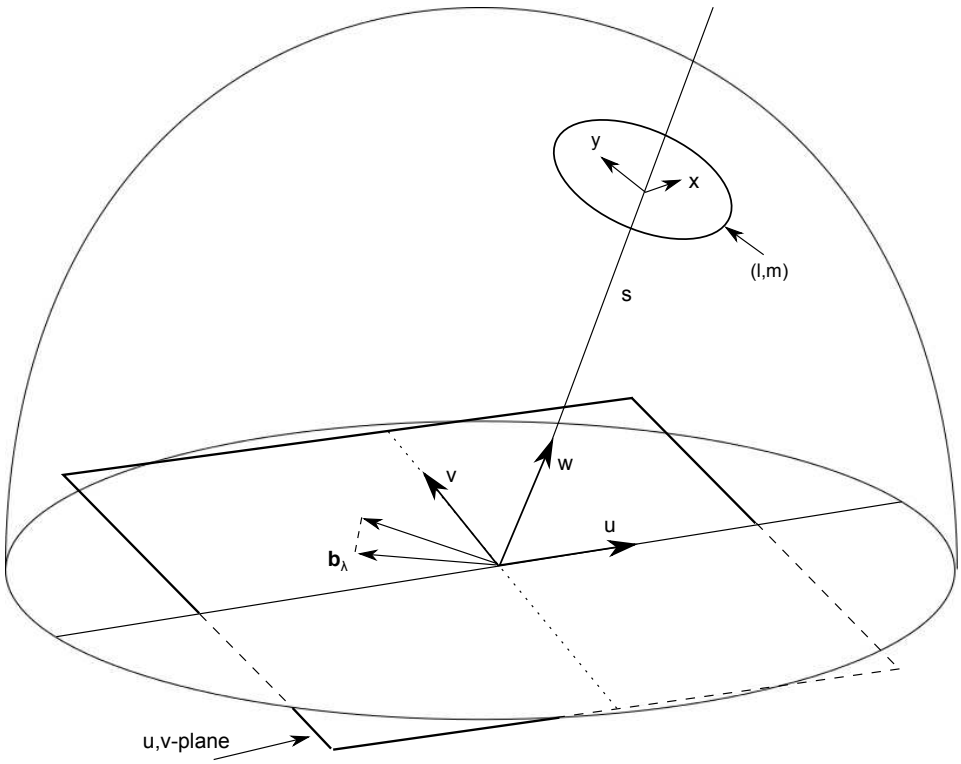

Figure 2.3: A schematic showing the geometrical relationship between the *uv* plane and the source plane (the celestial sphere), with coordinates (*l*,*m*) that become the celestial angular coordinates (*x*,*y*) in the small-angle approximation. Based on Burke and Graham-Smith (2002).

2.1.2 Aperture Synthesis

Aperture synthesis is the simultaneous use of many interferometric baselines and is augmented by Earth-rotation synthesis, which provides a continuous arc of baselines through exploitation of the rotation of the Earth. The complex visibility in equation 2.6 provides only one Fourier component of the brightness distribution, hence to obtain multiple measurements, multiple baselines from an array of telescopes are required. In a given integration time, an array of N elements can generate N(N - 1)/2 visibilities. If a source is suitably simple or there are many antennas, a short averaging time may suffice. Otherwise, Earth-rotation synthesis is utilised if insufficient coverage of the *uv*−plane provides inadequate images i.e. there are not enough Fourier components to describe the source (Burke and Graham-Smith 2002).

2.1.3 Submillimeter Array

The observations undertaken in this work, utilised both the compact and compact-north configurations of the Submillimeter Array (SMA). The compact configuration provides six antennas (15 baselines), ranging in length from 16.5 to 32m. The compact-north configuration on the other hand provides longer north-south baselines, for more circular beams for sources in the southern hemisphere. For an observation at 226GHz in the lower side band, at -37° declination with precipitable water vapour at 2.0mm, the *uv* coverage is similar to that presented in Figure 2.4.

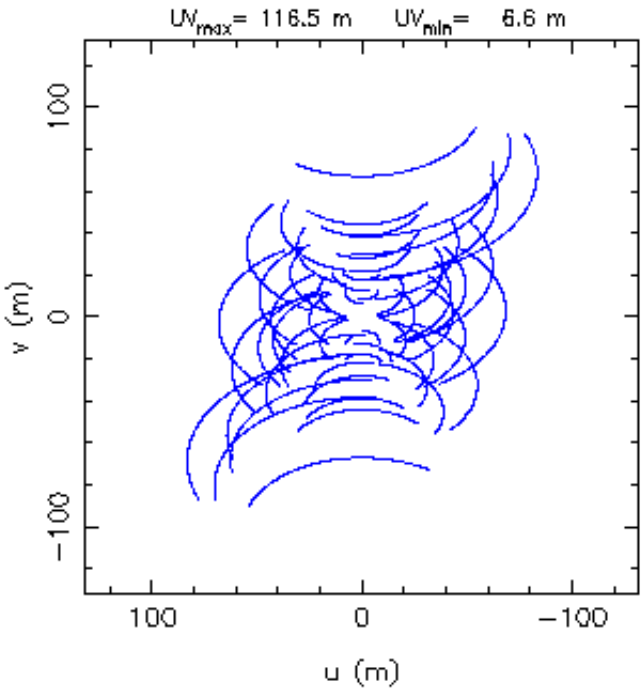

Figure 2.4: SMA *uv* coverage for an observation similar to those undertaken in this work, taken at 226GHz in the lower side band, at -37° declination with precipitable water vapour at 2.0mm, using the compact-north configuration of the SMA.

2.1.4 Dirty Beams

For each sky brightness distribution I(*l*,*m*), there is a corresponding visibility function V(*u*,*v*), that is its Fourier Transform (FT). In practice however, visibilities are not measured at all points in the *uv* plane, but are sampled at particular points. This measured set of points is referred to as the sampling function S(*u*,*v*), and is equal to zero in the absence of data. The expression for the image incorporating S(*u*,*v*) can now be written as,

$$I_\nu^D(l,m) = \int\int V_\nu(u,v)\, S(u,v)\, e^{-i2\pi(ul+vm)}\, du\, dv \tag{2.12}$$

where I_ν^D(l,m) is often referred to as the *dirty image* and is related to the intensity distribution, I(*l*,*m*) through utilisation of the convolution theorem for Fourier Transforms, by $I_\nu^D = I_\nu * B$. Here, $*$ denotes the convolution and B is the synthesised beam or point spread function, which corresponds to the sampling function, S(u,v) (Perley et al. 1986). This synthesised beam, the FT of the sampling pattern, is also known as the *dirty beam*.

Subtraction of the *dirty beam* from the *dirty image* removes unwanted artefacts, caused by the limited sampling of the *uv*-plane. This method of trying to recover the true sky through successive iterations of the subtraction process to deconvolve the dirty beam is implemented in the CLEAN algorithm (Perley et al. 1986). The CLEAN algorithm assumes that the image can be represented by a small number of point sources and uses the iterative procedure to locate the highest value in the residual image. The *dirty beam* (or point spread function) is subtracted from the highest value in the *dirty image*. The process is stopped when the maximum value in the residual map is smaller than a predefined threshold or a specified number of iterations is reached. The image is reconstructed by returning all of the components removed in the the previous step, in the form of an idealised point spread function (a *clean beam*) with appropriate positions and amplitudes.

Deconvolution of the SMA images in this work were performed with CASA[2] and the default input parameters for the CLEAN process utilised the Clark Algorithm. In simplistic terms, the Clark algorithm uses only a small patch of the dirty beam to find approximate positions and strengths of the source and selects points if the intensity (as a fraction of the image peak) is greater than the beams highest exterior sidelobe. For a more detailed description on this algorithm, see Perley et al. (1986), Lecture 7.

[2]http://casa.nrao.edu/

3

SMA Observations and Results

3.1 Data Reduction

Two tracks (with a total on-source integration time of about 9 hrs) were requested from the SMA to complete the observations required for this study and were obtained on 13th June 2010 (track 1) and 26 June 2010 (track 2), with a phase centre positioned at RA (2000) $17^h13^m44.2^s$ Dec (2000) -37°06′ 16.0″. A total bandwidth of 4 GHz per track was observed with track 1 covering a frequency range of 214.065 – 217.944 GHz in the lower side band (lsb) and between 225.962 and 229.841 GHz for the upper side band (usb). For track 2, the lsb observed frequencies between 263.967 – 267.846 GHz whilst the usb included frequencies between 275.864 – 279463 GHz. The large bandwidth of the SMA correlator allowed the simultaneous cover of ^{13}CN and ^{12}CN in the lsb and usb of track 1, respectively. For track 2, HCO^+ was observed in the lsb, with HCN, ^{13}CS and N_2H^+ simultaneously observed in the usb.

For track 1 observations, 7 antennas were used in a compact configuration with a maximum baseline of 77 m. According to the SMA online sensitivity estimator a full track on NGC6302 will give 5 hours on source, which (with 4mm of atmospheric water) gives a noise level of 0.2 K in 4 km s^{-1} channels. This is sufficient to resolve the lines

which have widths 20 km s^{-1}. Even if the lines are smoothly distributed over the torus, they will be detected with a signal to noise ratio of 5 at the full angular resolution. Weather conditions were good but deteriorated for the last hour of observations. τ was just under 0.1 with an average relative humidity of 10% and $T_{sys} \approx 200$K. Nearby quasars 1626-298 and 1733-130 were frequently monitored to correct for phase variation due to atmospheric variations and bandpass calibration was done using 3C279 and 3C454.3. The phase and amplitude were calibrated for approximately 10 mins, for about every 20 minutes of integration on the target. The flux calibration was performed using Neptune and Titan.

Observations obtained in track 2 utilised all 8 antennas in a compact north configuration with a maximum baseline of 62 m. The central frequency was set to 265.886 GHz with a total bandwidth of 4 GHz (2 GHz each for the lsb and usb). Weather conditions were good for the first half of the evening but worsened for the remaining half of the observations. τ was just under 0.2 with an average relative humidity of 20% for the first half of the night and 40% for the remaining. T_{sys} was $\approx$ 220 K. The phase and amplitude were calibrated using the same targets as for track 1, for six minutes for about every 30 minutes of integration on NGC 6302. 3C454.3 and Callisto and Mars were used as bandpass and flux calibrators respectively.

The visibility data were reduced using the SMA version of the Miriad software package, with spectra and maps later exported to CASA[1] for further inspection. After continuum emission subtraction was applied to the visibility data using the CONTSUB task, deconvolution of the dirty images was done using the CLEAN task. The resulting synthesized beam for CN (J = 2−1) channel maps is 6″ x 3″ at P.A = 0.0°. The synthesized beam for HCO^+ (J = 3−2) channel maps is slightly narrower at 6″ x 2.5″ at P.A = 0.0°. The rms noise level for each channel of 1 km s^{-1} is ∼135 mJy.

[1] http://casa.nrao.edu/

3.2 Observations Overview

NGC 6302 has been observed a number of times at a number of different frequencies, but the majority of observations to date have been concerned with the high-ionisation region of the nebula (the bipolar optical lobes). Observations that have included the central torus are limited to one or two molecular species. Consequently, a comprehensive molecular survey, along with any modelling to analyse the chemistry, has never been published. In addition, there is also a lack of comprehensive molecular surveys in PNe in the literature in general. As NGC 6302 has been identified with a potentially large, dense central torus capable of producing a rich and varied chemistry (Peretto et al. 2007), it was felt that this object would be an ideal candidate in which to map a broad range of molecular species and hence establish the molecular characteristics of the central torus. Further analysis was conducted through chemical models (§ 5) to determine if the environmental properties drove novel chemical reactions and pathways or not.

A list of all the species observed with the SMA is detailed in Table 3.1, followed by a description of the characteristics of the main species detected. NGC 6302 has a heliocentric radial velocity of -38.0 ± 0.8 km s^{-1} measured by Minkowski and Johnson (1967) from [NII] measurements of the nebular core. This correlates with the peak velocities of the majority of species observed in this work. It is also shown by Peretto et al. (2007) from their detailed ^{12}CO observations, that distinct velocity components exist within the torus of NGC 6302. These are identified at -64 to -48 km s^{-1}, -48 to -30 km s^{-1} and -30 to -15 km s^{-1} for the low, medium and high velocity components respectively. Similar velocity components are also identified by Dinh-V-Trung et al. (2008) and are reviewed below. Through analysis of the spectra obtained with the SMA in this work, it is apparent that other species (HCO^+ for example) show the same velocity structures; accordingly the emission maps for most of the species identified have been separated into the corresponding velocity components where applicable and

compared with the ^{12}CO J=2-1 SMA maps of Peretto et al. (2007). The central star, represented by a black star on the emission maps, is located at coordinates (J2000) α 17:13:44.45 and δ -37:06:11.1 which is the peak of the 1.3mm continuum, also taken from Peretto et al. (2007).

Whilst initially mentioned in section 1.4.1, it is worth noting again at this point that a number of velocity components have also been identified in recent observations of NGC 6302 by Bujarrabal et al. (2012), however the authors distinguish a different line core range at -25 to -20 km s^{-1} to represent the unaccelerated remnant of the AGB shell, compared with that of the medium velocity component established by Peretto et al. (2007). As seen in the spectra below, the peak intensity of species observed in this work are centred around -38 km s^{-1} and thus clearly fall within the medium velocity component identified by Peretto et al. (2007).

3.2.1 CO

The J = 2 – 1 CO transition lies outside the frequencies specified for the data collected with the SMA. Additionally, as CO has recently been discussed in detail by Dinh-V-Trung et al. (2008) and Peretto et al. (2007), it was felt that further analysis was not necessary here. However, as the CO emission is (generally) the dominating molecular emission within a PN, the CO emission from Peretto et al. (2007) is used as a comparison for the molecular distribution obtained from the SMA data. Integrated intensity peaks obtained by Peretto et al. (2007) for the three components as are follows; 12.5, 27.3 and 15.4 K km s^{-1} for the low, medium and high velocity components respectively. An overview of both authors work is discussed below.

The ^{12}CO and ^{13}CO J = 2 -1 emission from Dinh-V-Trung et al. (2008) display high

Table 3.1: List of species observed in NGC 6302 with the SMA. † indicates the central rest frequency of the multiple hyperfine lines for CN and ^{13}CN. The hyperfine frequencies are listed in Table 4.1 and 4.2 for CN and ^{13}CN respectively. The peak figure for both species similarly refers to the central rest frequency for both species, which is the brightest line. The spectrum and integrated intensity map for $^{29}SiC_2$ is detailed in the appendix. The tentative detection of Si^{13}CC is shown on the N_2H^+ spectrum.

Frequency (GHz)	Species	Transition	Maximum (peak) (Jy beam^{-1})	RMS (Jy beam^{-1})	Notes
226.892†	CN	2-1	2.01	0.05	
217.467†	^{13}CN	2-1	0.31	0.07	
267.557	HCO^+	3-2	6.43	0.07	
265.886	HCN	3-2	4.93	0.08	
277.455	^{13}CS	6-5	1.56	0.09	
217.104	SiO	5-4 v=0	0.61	0.07	
215.596	SiO	5-4 v=1	0.46	0.05	
279.511	N_2H^+	3-2	0.39	0.04	
229.304	$^{29}SiC_2$	10-9	0.28	0.06	Tentative detection
279.471	Si^{13}CC	12-11	0.35	0.04	Tentative detection

velocity wings (extending up to $\sim$ 40 km s^{-1}) with very peculiar and complex shapes and is suggested by Dinh-V-Trung et al. (2008) to represent a nonspherical envelope which could contain a fast molecular outflow. Their channel maps show the emission breaking into separate clumps at velocities from -36 to -32 km s^{-1} with intensity dominating in the northern clump. This is reflected in the total integrated intensity map which shows a double peaked structure with the main peak around -40 km s^{-1} and a smaller peak around -20 km s^{-1}. Dinh-V-Trung et al. (2008) state that the peaks of the medium and high velocity components are located on either side of the continuum peak, albeit shifted northwards by a few arcseconds. Coupled with the low velocity of these components, Dinh-V-Trung et al. (2008) suggest these features are indicative of an expanding toroidal structure, which may be weaker (or incomplete) towards the south, due to the shift in the north. The deconvolved size of the ^{12}CO emission is 10.8″

x 2.1″ at velocity V_{LSR} = -38 km s^{-1}, and the emission is strongly elongated in the north-south direction.

Dinh-V-Trung et al. (2008) also detect knots in their maps and attribute some to molecular bullets, a type of compact, high velocity outflow seen in other young PNe. Such a flow is postulated to form from fast collimated outflows interacting with the ambient gas of the slowly expanding envelope. The authors report that both the ^{12}CO J = 1-0 and ^{12}CO J = 2-1 transition are most likely optically thick, whilst the ^{13}CO emission is optically thin and conclude that the peak brightness temperature for the J = 2-1 emission is ∼ 2 K. From the combined mass components, Dinh-V-Trung et al. (2008) find a total molecular mass (derived from their ^{13}CO data) of ∼ 0.1 $M_{\odot}$; a figure higher than that obtained by Huggins et al. (1996) ∼ 0.022 $M_{\odot}$, but somewhat smaller than that presented by Peretto et al. (2007) ∼ 1.4 $M_{\odot}$. Dinh-V-Trung et al. (2008) find a total gas estimate (including atomic mass) as ∼ 0.4-0.5 $M_{\odot}$.

^{12}CO and ^{13}CO data were obtained by Peretto et al. (2007) using both the JCMT (for J=3-2) and SMA (J=2-1). Their emission displays several broad components between a velocity range of -15 to -65 km s^{-1}, with narrow components seen only in the ^{12}CO emission at -38, -30 and -10 km s^{-1}. Peretto et al. (2007) suggest that the relative strengths of these features trace gas which has a high ^{12}CO/^{13}CO ratio. Two of these narrow components (-30 and -10 km s^{-1}) are missing however, in their SMA observations. Peretto et al. (2007) point out that due to the nature of the SMA interferometric data (higher resolution and insensitivity to very extended emission), it is likely that these components are associated with the extended emission of NGC 6302 or are unrelated interstellar gas. The component at -38 km s^{-1} which is evident in their SMA data is however attributed with the molecular torus. Peretto et al. (2007) define three velocity components (Fig 1.5) evident in all their spectra but most clearly defined at ^{12}CO $J = 2 - 1$, at -64 to -48 km s^{-1}, -48 to -30 km s^{-1} and -30 to -15 km s^{-1} for the low, medium and high velocity components respectively. Peretto et al. (2007) suggest that

the velocity components outlined in their observations are indicative of an expanding torus, rather than a disk-like structure around NGC 6302. The high velocity component is described as tracing the optically thin warm gas located behind the star, whilst the medium velocity component is associated with the optically thick cold gas located in front of the star. The low velocity component is described as peaking 7″ south-east of the central source and thus is not part of the torus; this velocity range is found in only one species of the SMA data and so discussion is limited on this component. The velocity range between -75 and -64 km s^{-1} is discussed by Dinh-V-Trung et al. (2008) however, who identify discrete molecular knots in this blueshifted component.

3.3 SMA Spectra and Maps

3.3.1 HCN

The HCN spectra (Fig 3.1) clearly shows emission in the equivalent medium and high velocity components as noted above. The brightest emission appears in channels around -38 km s^{-1} with blending of a smaller component apparent around -44 km s^{-1}. A smaller wing/feature in the spectra is incident with the high velocity component and peaks at -25 km s^{-1}. The feature at +25 km s^{-1} which extends to +45 km s^{-1}, is a set of defective channels and when viewed in the image map clearly shows an artefact.

The integrated HCN (3-2) emission for the high velocity component V_{LSR} = -28 to -16 km s^{-1} is shown in Figure 3.3, whilst that for the medium velocity component V_{LSR} = -44 to -34 km s^{-1} is displayed in Figure 3.2. The HCN emission (from both components) in the same velocity range, show a clear correlation with the peak of ^{12}CO. Figure 3.2 shows that the lower contours of the HCN medium component have a distinct broadening to the southwest not coincident with the ^{12}CO emission, which has an extended broadened emission to the northeast with further narrow extended emission to the south. Conversely, the inner contours of the component in Figure 3.3,

closely trace the ^{12}CO structure, with emission for both species peaking off centre to the east from the continuum peak (central star location). The outer contour however has extended emission (to somewhat of a lesser degree than the medium component) to the east and to the south, which is not mirrored in the ^{12}CO emission. Compared with the HCN emission the ^{12}CO emission is extended to the north. The broadening of the HCN emission to the southeast could be tracing an outflow. Observations by Elliott and Meaburn (1977) identified neutral (as well as ionised) material flowing in four separate but major streams from the core; two were angled towards the observer from one side of the core and two tilted away from the observer on the opposite side. Similarly, fast CO outflows in the form of molecular knots, have also been identified by Dinh-V-Trung et al. (2008) in NGC 6302. These knots, whilst located in the bipolar lobes, are offset from the major nebula axis in the east-west direction and to the south of the central region (marked by the continuum emission).

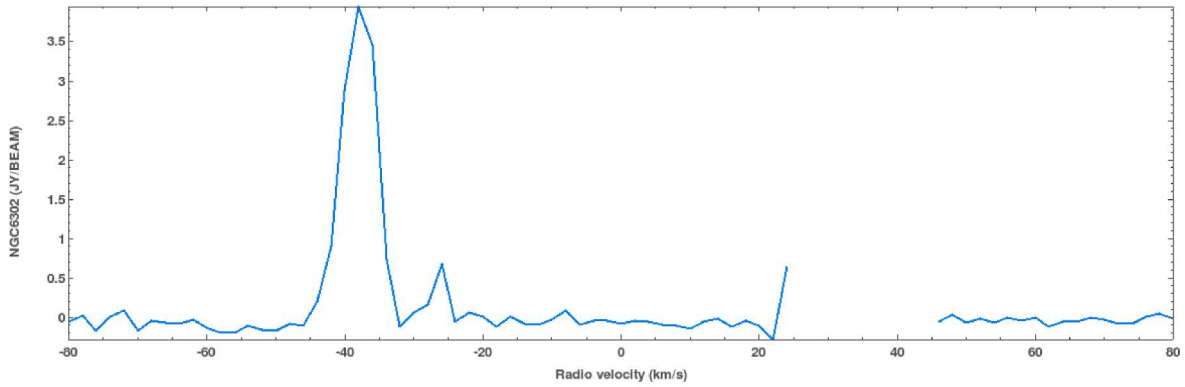

Figure 3.1: HCN spectrum showing main peak centred around -38 km s^{-1} with a small wing to the right peaking at -20 km s^{-1}. The gap at +25 km s^{-1} which extends to +45 km s^{-1} are bad channels and should be disregarded. The spectrum is obtained from the central pixel located within the brightest region, i.e the peak of emission.

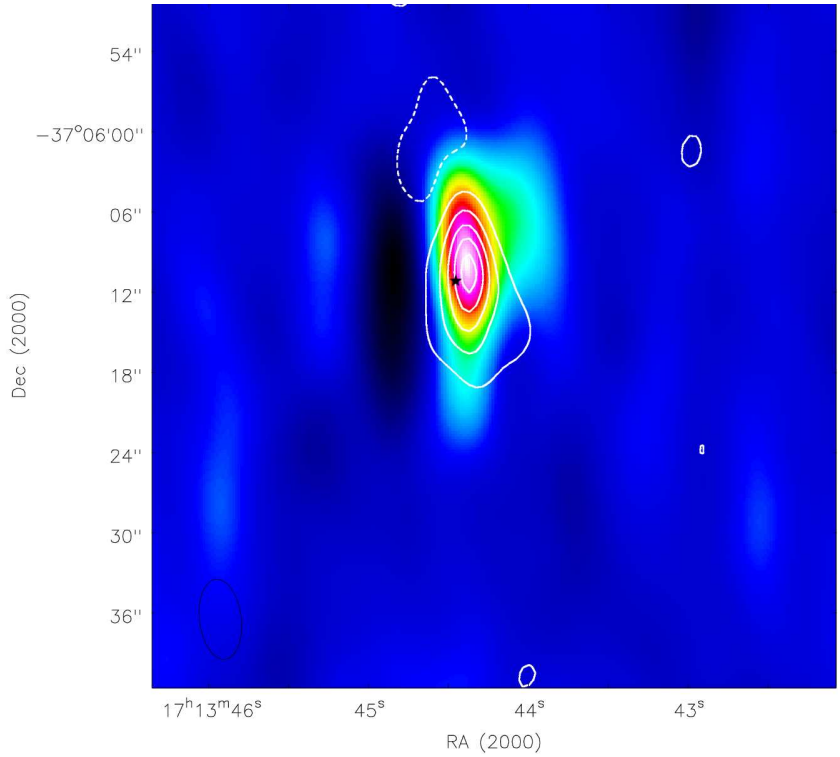

Figure 3.2: HCN (J=3-2) medium velocity component integrated intensity map (contours) with ^{12}CO medium velocity component (colours). The integrated intensity map for HCN is from -44 to -34 km s^{-1} with a peak value of 27.4 (K km s^{-1}). Contours are spaced from 10 to 90% in steps of 20% of the peak value. Negative contours are in dashed lines and are at 10% of the main peak value.

3.3.2 HCO$^+$

HCO$^+$ and CN are the only species observed in this work, which shows all three components detected by Peretto et al. (2007) distinctly. The high and medium components can be identified in the HCO$^+$ spectrum (Figure 3.4) which displays a clear line central core, peaking at 6.43 Jy beam^{-1} coupled with the characteristic redshifted wing to the right of the main line. The low velocity component however is blended with the main peak.

The integrated HCO$^+$ (3-2) emission for the low velocity component is V_{LSR} = -50 to -48 km s^{-1}, for the medium velocity component V_{LSR} = -48 to -34 km s^{-1}, whilst

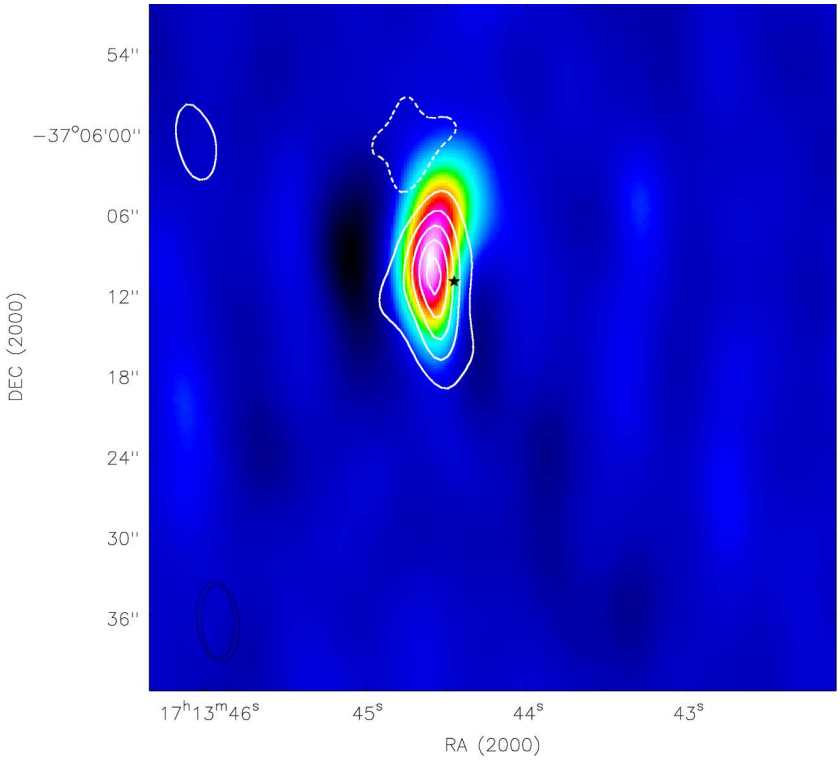

Figure 3.3: HCN (J=3-2) high velocity component integrated intensity map (contours) ^{12}CO high velocity component (colours). The integrated intensity map for HCN is from -28 to -18 km s^{-1} with a peak value of 19.2 (K km s^{-1}). Contours are spaced from 10 to 90% in steps of 20% of the peak value. Negative contours are in dashed lines and are at 10% of the main peak value.

for the high velocity component V_{LSR} = -28 to -16 km s^{-1}. In Fig3.5 (and also in Figure 5c of Peretto et al. (2007)) the superposition of the Hα image with the ^{12}CO integrated intensity map for the low velocity component is shown. On this image it is clear to see that the ^{12}CO low velocity component is a double peaked structure, with the brighter peak offset from the continuum peak by $\sim$7″ to the south. The peaks of the CO straddle the southern end of the torus with the brightest peak coincident with the bright emission of the eastern lobe, and is located on the edge of the south-south-east outflow, whilst the second peak borders the south-south-west edge of the western lobe. The low velocity HCO^+ emission (Fig 3.6) however, is centred on the brightest peak only and is only evident in two channels. It is thus integrated from -50 to -48 km s^{-1} whilst the ^{12}CO emission is integrated over a larger velocity range from -64 to

-48 km s^{-1} and is approximately twice as bright (12.5 K km s^{-1} compared with a peak of 5.93 K km s^{-1} for HCO^+). Nonetheless, the positioning of both bright peaks would suggest some affiliation with the outflows of the eastern lobe. The HCO^+ medium velocity component emission (Fig 3.7) is similar to that of HCN, with the inner contours closely aligned to the brightest peak of the ^{12}CO emission, nevertheless, the HCO^+ emission is heavily extended and broadened to the south with a slight direction shift to the southwest. Similarly the extended ^{12}CO emission to the northwest is not traced by the HCO^+ emission. The inner contours of the high velocity component (Fig 3.8) again, are closely associated with the ^{12}CO high velocity component, the outer contour however is extended in all directions except northwards. The distribution is asymmetrical and is particularly prominent south and westwards.

It can be seen in the three velocity components (Figures 3.6, 3.7 and 3.8) that the peak position (in declination) is $\sim 14''$ (at -49 km s^{-1}), $\sim 12''$ (at -39 km s^{-1}) and $\sim 10''$ (at -23 km s^{-1}). This is indicative of a velocity gradient in the HCO^+ distribution and is likely due to the expansion of the torus. An expanding torus is also observed in CO emission by both Dinh-V-Trung et al. (2008) and Peretto et al. (2007), but is not seen in any other observed molecular species in this work. Figures **??** and **??** show the HCO^+ velocity channel maps, which details the velocity distribution of the emission and clearly shows the peak of the low, medium and high velocity components discussed above.

3.3.3 ^{13}CS

Emission from ^{13}CS J = 6-5 is limited to a velocity of V_{LSR} = -38 km s^{-1} only, and therefore is confined to the medium velocity component. A high velocity component is absent and the characteristic wing feature seen in HCN and HCO^+ is not apparent in the spectrum (Fig 3.11). The main line peaks at 1.56 Jy $beam^{-1}$ and the FWHM is

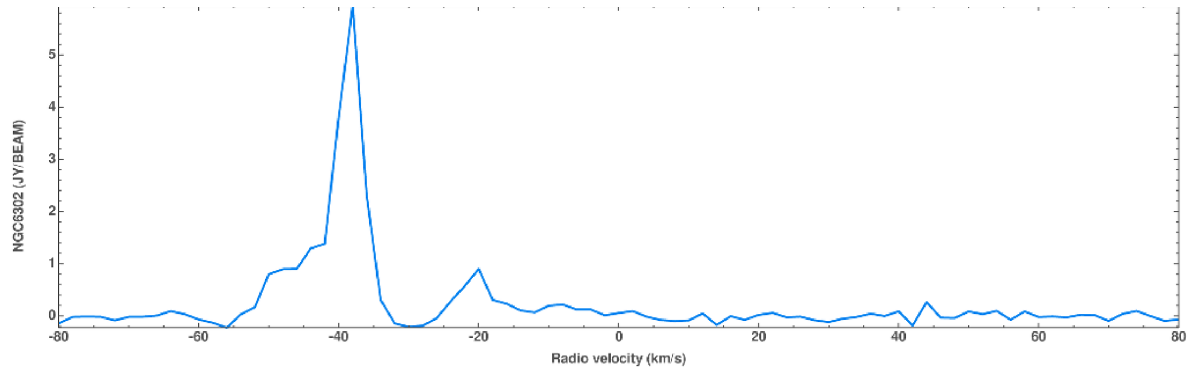

Figure 3.4: HCO^+ spectrum showing main peak centred around -38 km s^{-1} blended with the high velocity component. The small wing to the right peaking at -25 km s^{-1} is the low velocity component. The HCO^+ spectrum is obtained from the central pixel located within the brightest region, i.e the peak of emission.

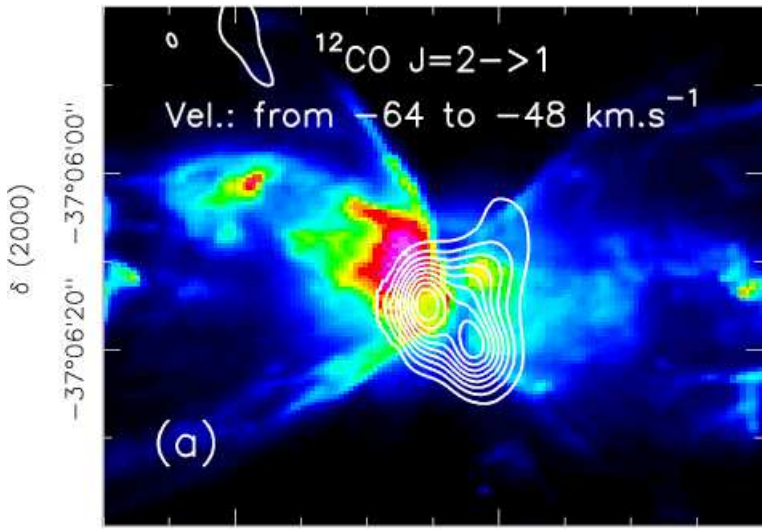

Figure 3.5: ^{12}CO low velocity component integrated intensity map (contours) overlaid on Hα image (colours) showing the position of the peaks in relation to the torus structure from Peretto et al. (2007).

~4 km s^{-1} confirming the narrow line width of this species compared with other observed species. The brightest ^{13}CS emission corresponds with the central peak of the ^{12}CO emission, albeit it is slightly shifted eastwards with contours tightly packed on the west side of the structure. The outer contours however, elongate outwards towards the south-east, in the direction of the eastern outflow lobe. The geometry of NGC

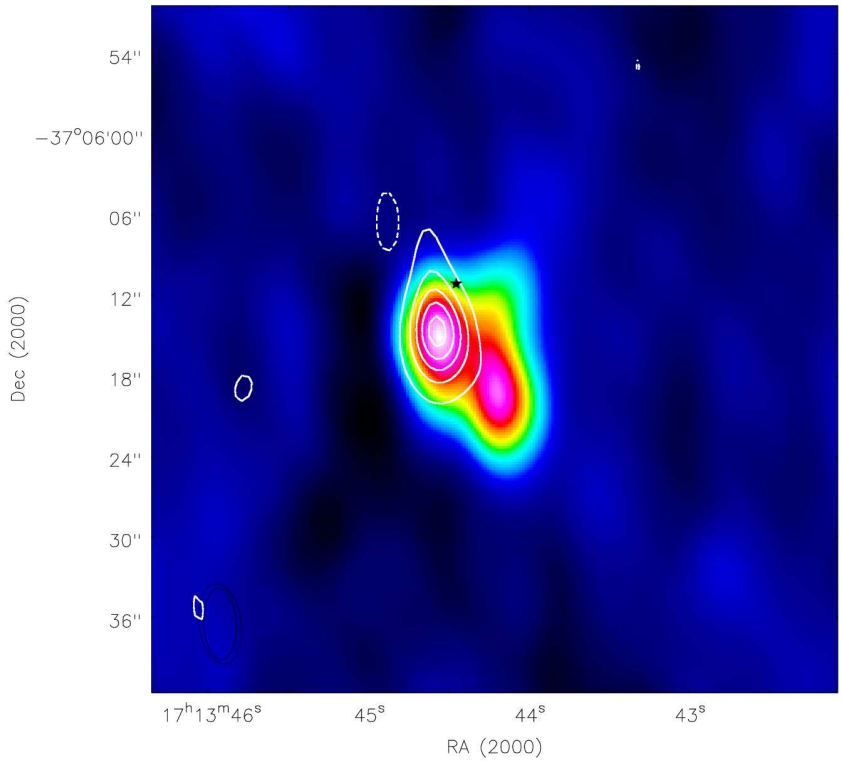

Figure 3.6: HCO^+ (J=3-2) low velocity component integrated intensity map (contours) with ^{12}CO low velocity component (colours). The integrated intensity map for HCO^+ is from -50 to -48 km s^{-1}, with a peak value of 5.93 K km s^{-1}. Contours are from 10 to 90% in steps of 20% of the peak value. Negative contours are in dashed lines and are at 10% of the main peak value.

6302 (see for example Meaburn et al. (2005), Peretto et al. (2007), Dinh-V-Trung et al. (2008) and Wright et al. (2011)) indicates that the bipolar lobes are orientated perpendicular to the expanding torus with the western lobe pointing away from the observer, whilst the eastern lobe is closer to the observer. In the optical images of the VLT and HST (Kemper et al. (2002) and Matsuura et al. (2005) respectively), the eastern lobe is brighter, hence reinforcing the suggestion that the western lobe is obscured by the intervening dust in the torus. In high-excitation regions, sulphur is easily ionised (with an ionisation potential of 10.36 eV), and S^+ is the main precursor to CS (Goicoechea and Le Bourlot 2007). As CS formation is also known to be favoured in UV radiated regions, it is possible that the enhanced emission is tracing higher ionised gas in the eastern lobe.

It is unfortunate that the two tracks requested from the SMA did not cover the appropriate frequency to observe ^{12}CS in the same observing run, as comparison between the two isotopologues would have given further insights into the distribution of the emission.

3.3.4 SiO

The identification of SiO in NGC 6302 is as surprising as the nature of the SiO emission, which is shown in Figures 3.14 and 3.15. Two transitions of SiO (v=0 and v=1, J = 5-4) have been observed and as can be seen in the spectra, SiO displays a sharp, nar-

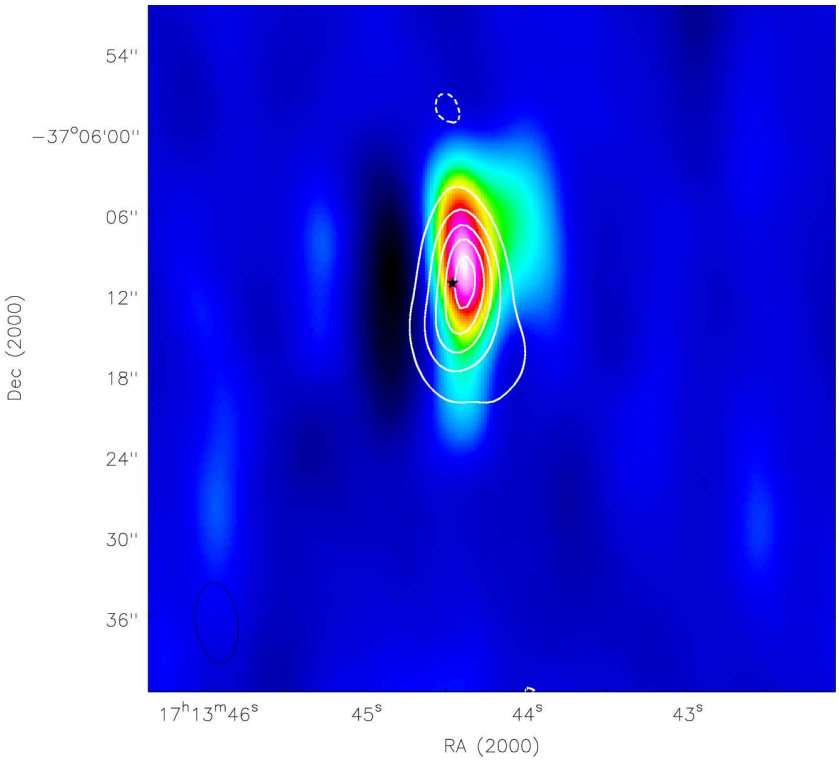

Figure 3.7: HCO^+ (J=3-2) medium velocity component (contours) with ^{12}CO medium velocity component (colours). The integrated intensity map for HCO^+ is from -44 to -34 km s^{-1}, with a peak value of 39.1 (K km s^{-1}). Contours are spaced from 10 to 90% in steps of 20% of the peak value. Negative contours are in dashed lines and are at 10% of the main peak value.

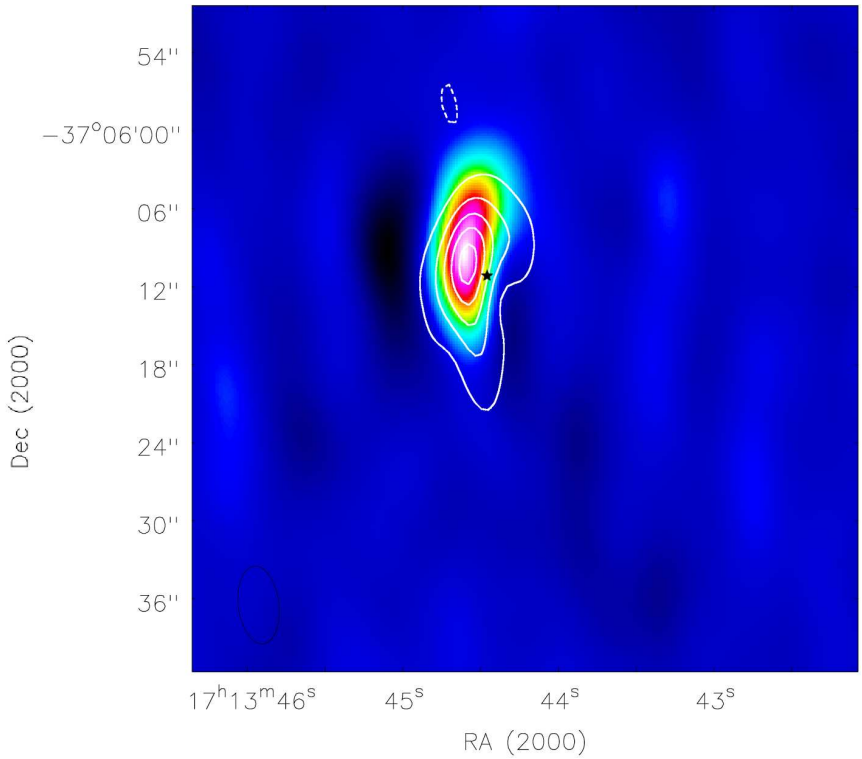

Figure 3.8: HCO^+ (J=3-2) high velocity component (integrated intensity map) contours with ^{12}CO high velocity component (colours). The HCO^+ integrated intensity map is from -28 to -18 km s^{-1}, with a peak value of 19.1 (K km s^{-1}) with contours from 10 to 90% in steps of 20% of the peak value. Negative contours are in dashed lines and are at 10% of the main peak value.

row peaked emission, commonly associated with maser emission (Figure 3.13). The integrated intensity maps are thus restricted to one channel at a velocity of V_{LSR} = -36 km s^{-1} for SiO *v*=0 and V_{LSR} = -26 km s^{-1} for SiO *v*=1, and accordingly can be assigned to the medium and high velocity components, respectively. The integrated intensity maps for both transitions show a compact structure with the emission concentrated on the eastern edge of the respective ^{12}CO velocity components. The peak of the SiO *v*=0 emission is ∼5″ northwards of SiO *v*=1 and neither peak is coincident with the brightest ^{12}CO peak emission. The contours of SiO *v*=0 are tilted in a northwest direction and broaden to the east and south, the contours of SiO *v*=1 on the other hand, mimic the ^{12}CO high velocity structure, albeit in a compacted form and are displaced to the southern end of the emission. If indeed this is maser emission it is

unlikely to be associated with the cooler, dense torus, but instead emission would be offset and located closer to the lobes, where pumping of SiO material can produce the masers. However, maser emission at the spatial resolution of the SMA observations would probably be point-like and the SiO emission is not resolved, hence indicating a different excitation mechanism. In addition, neither the J= 1−0 (43 Ghz) or J= 2=1 (86 GHz) masers have been identified in NGC 6302, both of which are considerably more common in AGB star sources, than J= 5−4 masers. The contour maps show emission on the periphery of the ^{12}CO, towards the eastern lobe, hence this region could be representative of a clumpy medium flowing outwards in the direction of the eastern lobe. Evidence of the destruction of silicaceous dust has been observed by Groves et al. (2002) and is discussed in Chapter 6.

3.3.5 N_2H^+

The spectrum of N_2H^+ (Fig 3.16) shows a broad line width ∼9 km s^{-1} compared with species such as ^{13}CS. The small wing feature to the right of the main peak cannot be conclusively identified, as it is not typical of the wing features in other species such as HCO^+, however, it is unlikely to be N_2H^+ and is hence possibly a blend with another species. Also shown on the spectrum is a tentative detection of Si^{13}CC. The low signal to noise however, limits a clear integration of emission to produce an integrated intensity map. N_2H^+ is similar to ^{13}CS in that only one velocity component is evident, with emission for N_2H^+ (3-2) limited to a velocity range of V_{LSR} = -42 to -36 km s^{-1} and hence is restricted to the medium velocity component. The N_2H^+ morphology (Fig 3.17) represents a compact structure with the contours centred on the brightest ^{12}CO emission. The contours are moderately elongated north and south, and show no further extended emission. Interestingly, the compact structure is very similar to that of the HCO^+ low velocity component emission, however the central emission of N_2H^+ is displaced ∼5″ to the north. The velocity separation between the two species is not too

dissimilar with HCO^+ emission ranging from -50 to -48 km s^{-1} (the lower end of the low velocity component) and N_2H^+ distributed from -42 to -36 km s^{-1} (the higher end of the medium velocity component). Nevertheless, as the production and destruction of HCO^+ and N_2H^+ are interwoven, with the destruction of N_2H^+ a formation route for HCO^+, the similarity of emission features and alignment, albeit somewhat shifted in location, may be indicative of co-dependency.

3.3.6 CN

The complete CN (2-1) spectrum, centred at 226.8735 GHz is displayed in Figure 3.18, showing the many hyperfine components within this bandwidth. The hyperfine components of the lower frequency group are clearly distinguished, however blending in the higher frequency group hinders identification of the individual components. The hyperfine components are discussed in detail in Chapter 4 with details of the hyperfine intensities listed in Table 4.1. The individual hyperfine components were integrated over the velocity range appropriate to the specific velocity component in order to provide the integrated intensity maps. For example, the low velocity component corresponds with hyperfine components F=$5/2-5/2$ and F=$3/2-3/2$, these were integrated over the velocity range V_{LSR} = -60 to -48 km s^{-1}. The hyperfine components F=$3/2-1/2$ and F=$7/2-5/2$ are within the confines of the medium velocity component and the individual components were then integrated over the velocity range V_{LSR} = -48 to -36 km s^{-1}. The high velocity component encompasses the F=$5/2-3/2$ component and was integrated over the velocity range V_{LSR} = -28 to -18 km s^{-1}. As noted above, CN and HCO^+ are the only species which distinctly show emission in all three velocity components identified by Peretto et al. (2007). The CN low velocity component however is unlike that of the HCO^+ low emission, as the peak CN emission does not correspond with either of the two peaks of the ^{12}CO low velocity component. Instead it lies 6″ to the north of the brightest ^{12}CO peak and is tilted in a north-north-west direction (Figure 3.20). The direction of the emission, does however lie in a similar di-

rection to the extended emission of ^{12}CO, with the outer contours elongated in a south easterly orientation. The outer contours also overlay the brightest ^{12}CO peak but the CN emission in general does not correspond with the structure of the ^{12}CO low velocity component. The contours of the CN medium velocity component are consistent with the brightest emission of ^{12}CO, the outer contour on the other hand, like most species observed, is elongated to the south, whereas the ^{12}CO extends to the northwest with tenuous emission to the south. Similarly, the high velocity component contours are cospatial with the ^{12}CO counterpart and closely match the ^{12}CO structure in shape. A slight extension to the south and west of the outer contour is discernible.

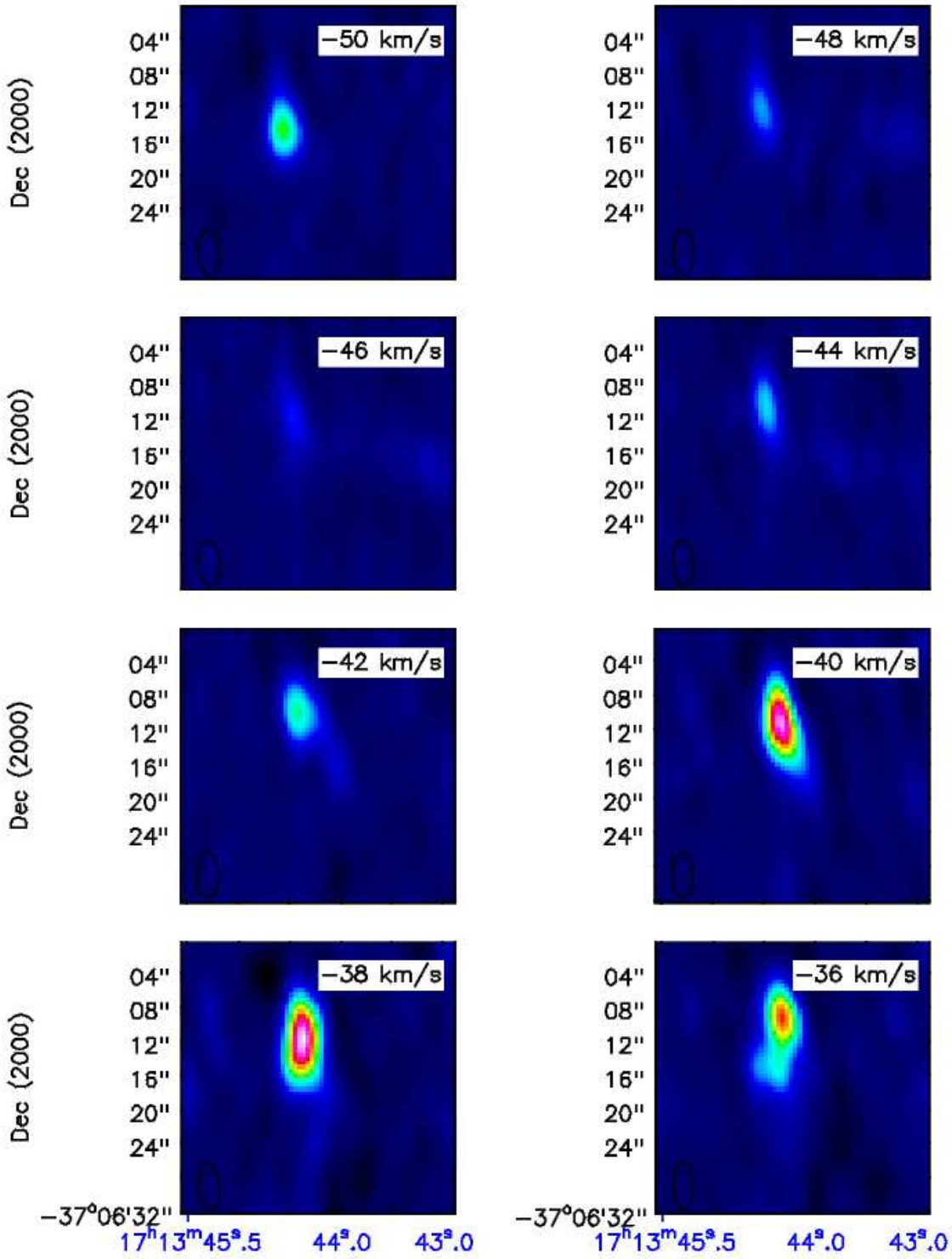

Figure 3.9: Velocity channel maps of HCO^+ (J=3-2) emission including the low velocity component (-64 to -48 km s^{-1}) and the majority of the medium velocity component (-48 to -30 km s^{-1}) which peaks at -38 km s^{-1}.

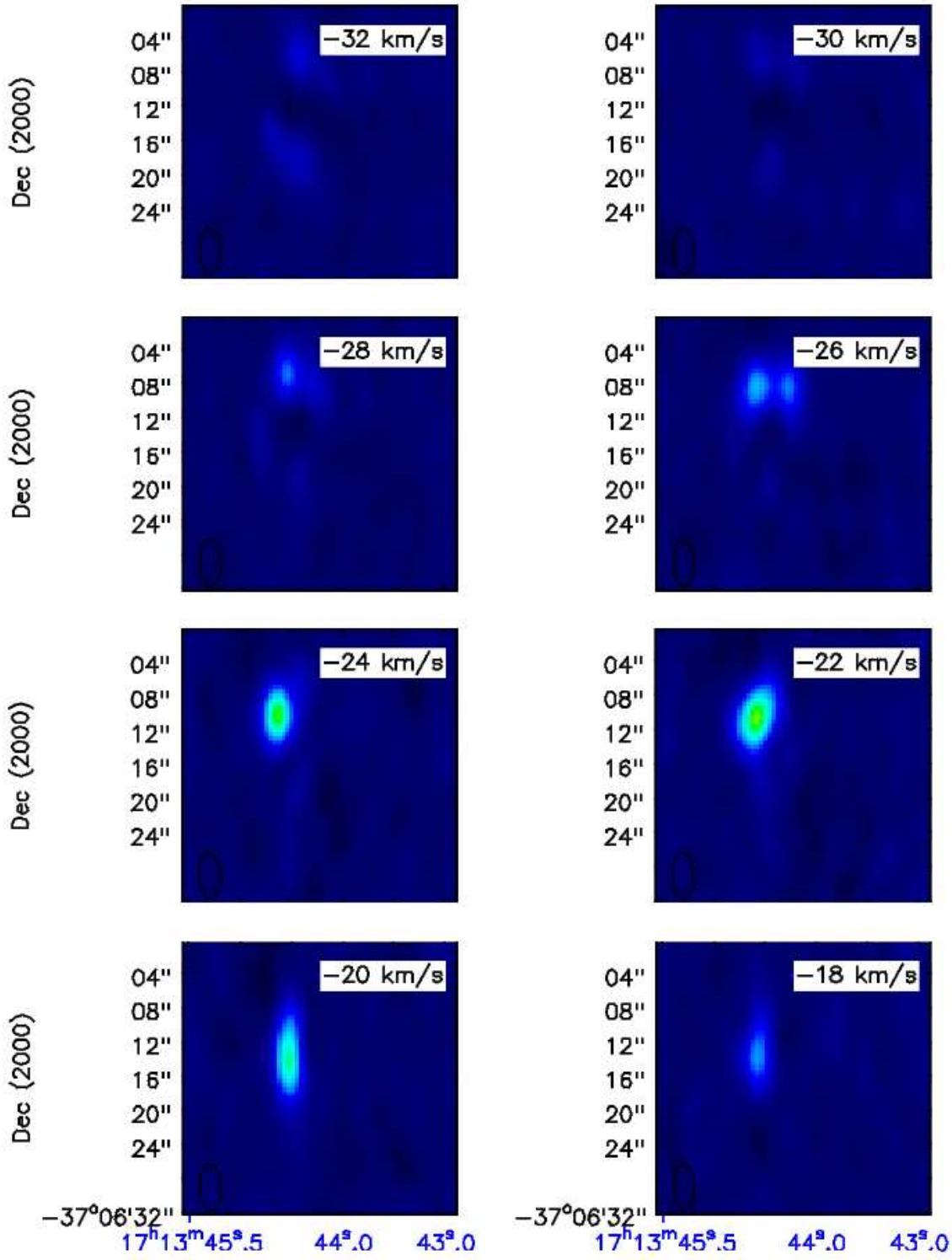

Figure 3.10: Velocity channel maps of HCO^+ (J=3-2) emission including the high velocity component (-30 to -15 km s^{-1}) which ends at -18 km s^{-1}.

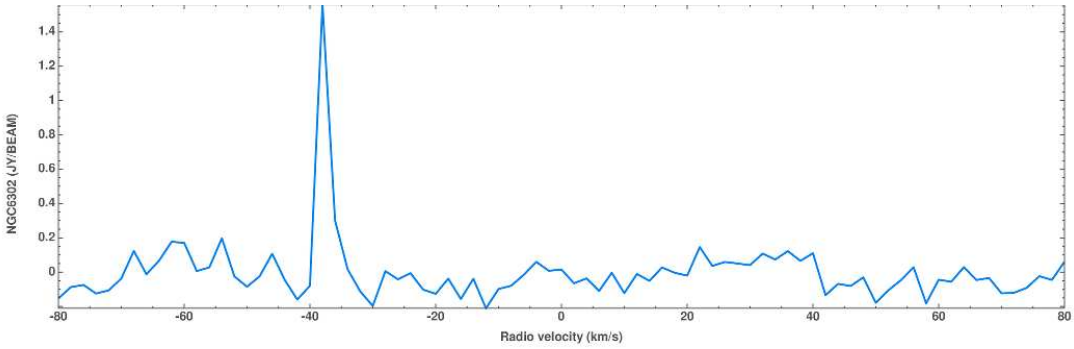

Figure 3.11: ^{13}CS spectrum showing a main peak only and is devoid of any wing features. The spectrum is obtained from the central pixel located within the brightest region, i.e the peak of emission.

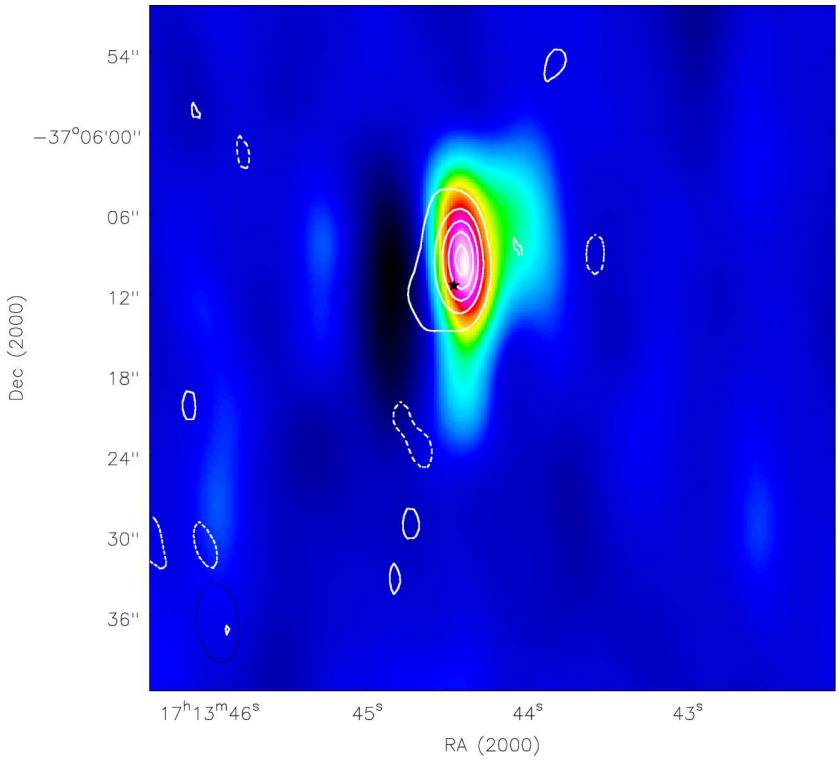

Figure 3.12: ^{13}CS medium velocity component integrated intensity map (contours) with ^{12}CO medium velocity component (colours). The ^{13}CS integrated intensity map is of one channel only and corresponds to a velocity of -38 km s^{-1} with a peak value of 3.76 (K km s^{-1}). Contours are from 10 to 90% in steps of 20% of the peak value. Negative contours are in dashed lines and are at 10% of the main peak value.

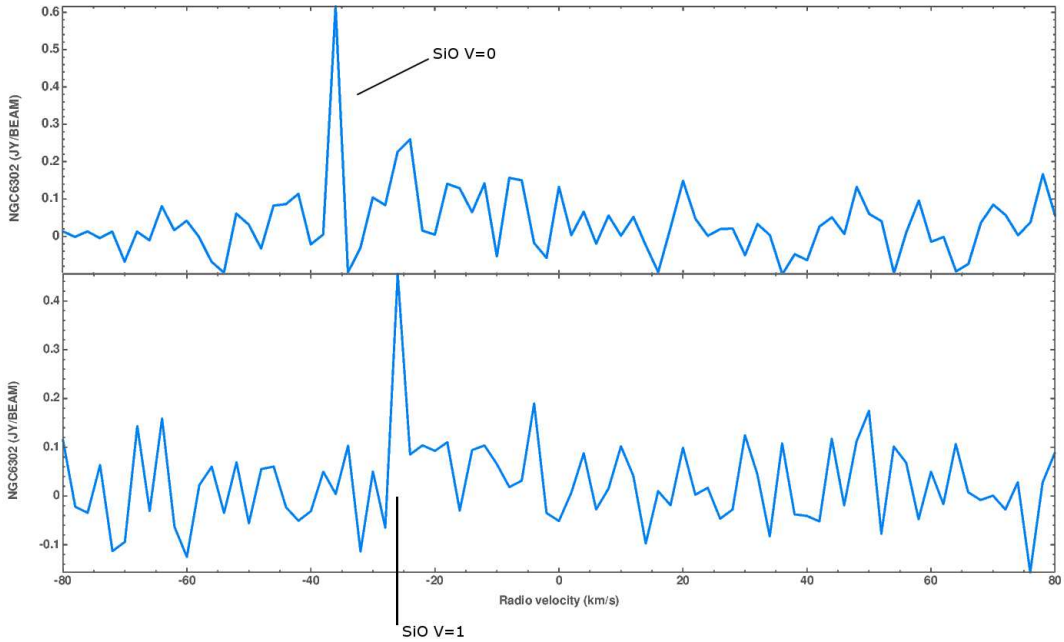

Figure 3.13: Spectra with both SiO 5-4 v=0 and v=1 transitions, showing the maser-like emission for this species. Transition v=0 is centred at velocity -36 km s^{-1}, whilst that of v=1 is centred at -26 km s^{-1} and corresponds to emission in the medium and high velocity components respectively. The spectrum is obtained from the central pixel located within the brightest region, i.e the peak of emission for both transitions.

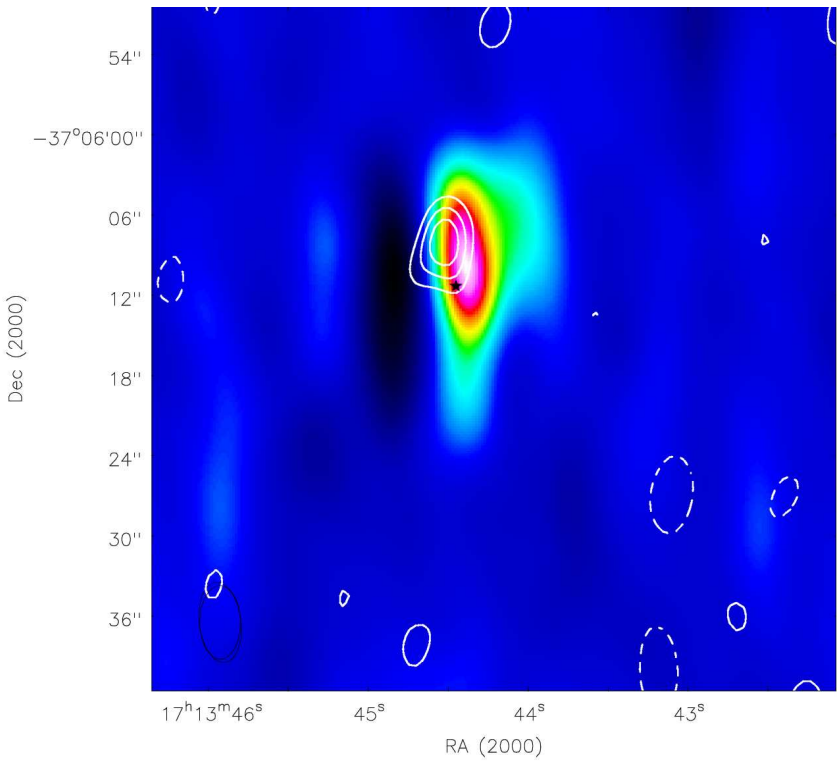

Figure 3.14: SiO V= 0 (J=5-4) medium velocity component integrated intensity map (contours) with ^{12}CO medium velocity component (colours). The SiO integrated intensity map is of one channel only and corresponds to a velocity of -36 km s^{-1} with a peak value of 1.23 (K km s^{-1}). Contours are from 40 to 80% in steps of 20% of the peak value. Negative contours are in dashed lines and are at -40% of the main peak value.

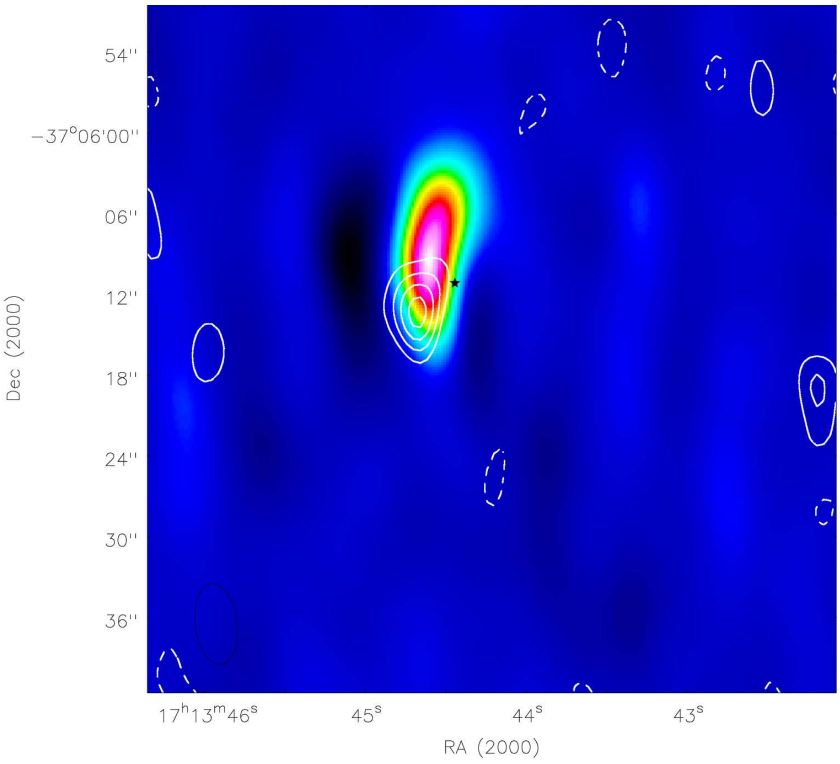

Figure 3.15: SiO V=1 (J=5-4) high velocity component integrated intensity map (contours) with ^{12}CO high velocity component (colours). The SiO integrated intensity map is of one channel only and corresponds to a velocity of -26 km s^{-1} with a peak value of 0.93 (K km s^{-1}). Contours are from 30 to 90% in steps of 20% of the peak value. Negative contours are in dashed lines and are at -30% of the main peak value.

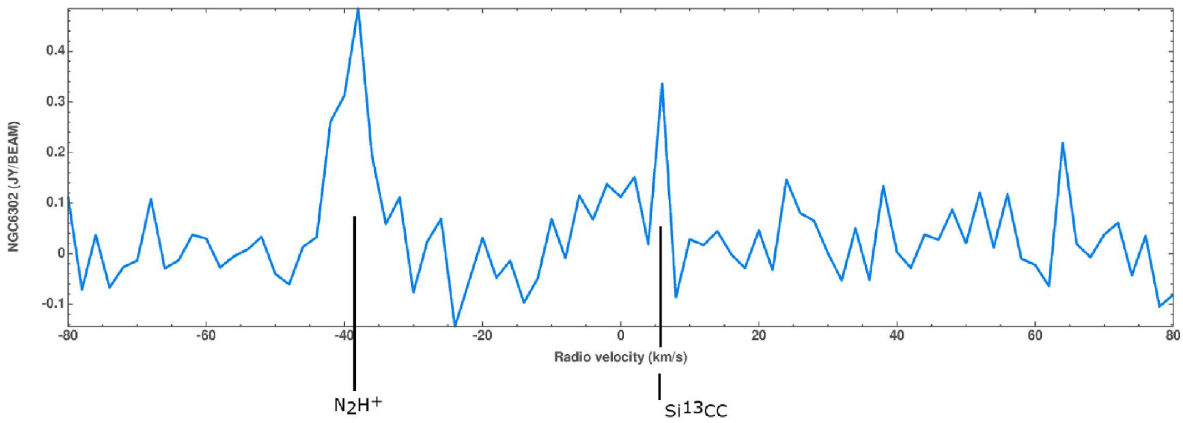

Figure 3.16: N_2H^+ spectrum showing main peak centred around -38 km s^{-1}. The small wing feature to the right of the main peak is a possible blend with another species, as it is not typical of the wing features presented in other spectrum (HCN for example). The spectrum for N_2H^+ is obtained from the central pixel located within the brightest region, i.e the peak of emission. At 6km s^{-1} a tentative detection of $Si^{13}CC$ is also marked.

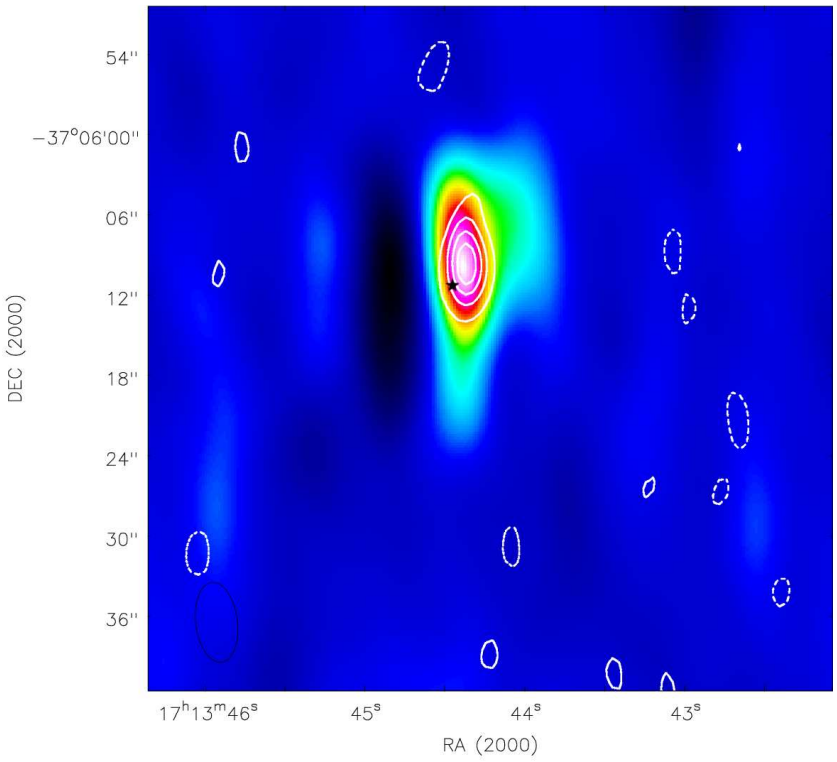

Figure 3.17: N_2H^+ medium velocity component integrated intensity map (contours) with ^{12}CO medium velocity component (colours). The integrated intensity map for N_2H^+ is from -42 to -36 km s^{-1} with a peak value of 2.92 (K km s^{-1}). Contours are spaced from 20 to 80% in steps of 20% of the peak value. Negative contours are in dashed lines and are at -20% of the main peak value.

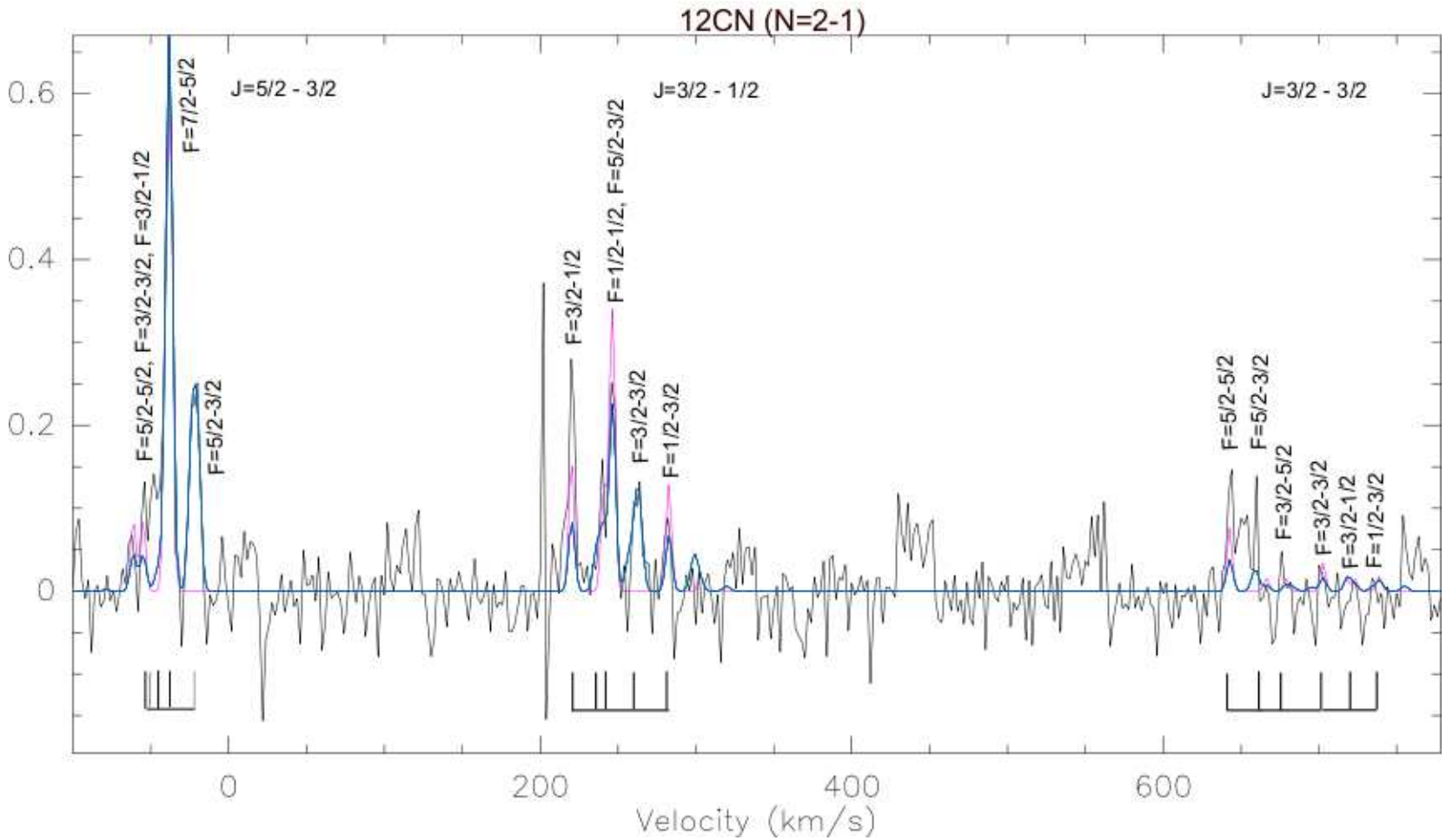

Figure 3.18: ^{12}CN spectra showing hyperfine structure and τ fitting using the CLASS software. Two fits of different velocities were applied to ensure that the majority of the hyperfine components were included. Fits were obtained using a method implemented in the GILDAS data reduction software package, CLASS and is described in §4.3.

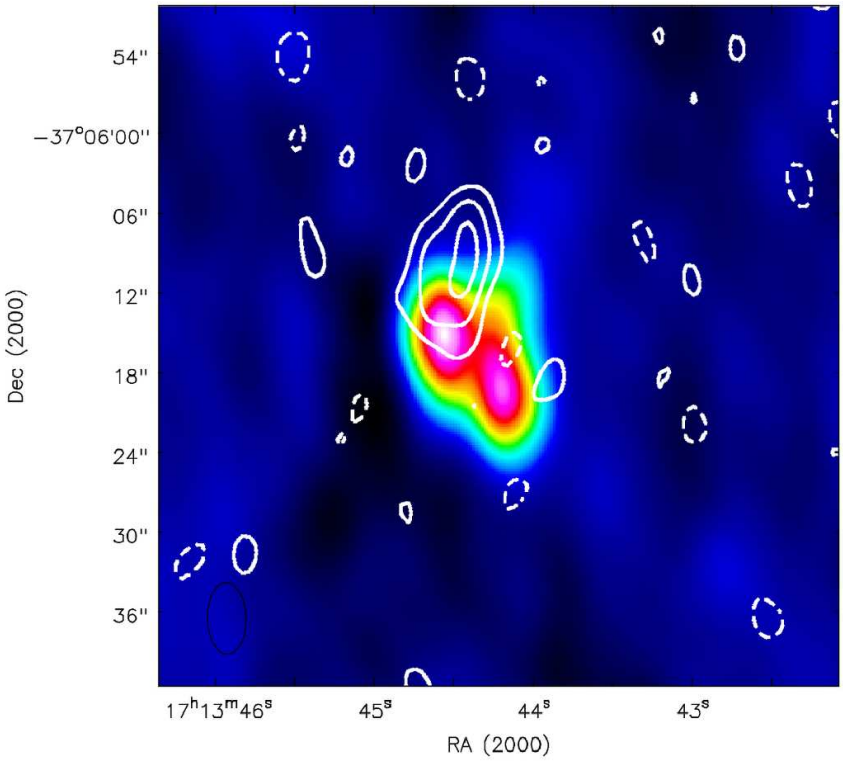

Figure 3.19: CN (J=2-1) low velocity component integrated intensity map (contours) with ^{12}CO low velocity component (colours). The CN integrated intensity map is from -60 to -48 km s^{-1} with a peak value of 1.79 (K km s^{-1}). Contours are from 30 to 90% in steps of 20% of the peak value. Negative contours are in dashed lines and are at 30% of the main peak value.

3.3.7 ^{13}CN

As with ^{12}CN, the complete ^{13}CN (2-1) spectrum, centred at 217.467 GHz is displayed in Figure 3.22, showing the many hyperfine components within this bandwidth. The hyperfine components of the main frequency group are clearly distinguished, however, in a similar manner to ^{12}CN, blending of the components is evident, especially in the lower frequency groups, thus limiting identification of the hyperfine components. Identification is also impeded by a low signal to noise for this species, so hence only the main hyperfine lines were included in the integrated intensity map and were integrated over V_{LSR} = -40 to -38 km s^{-1}. As per ^{12}CN, the hyperfine components are

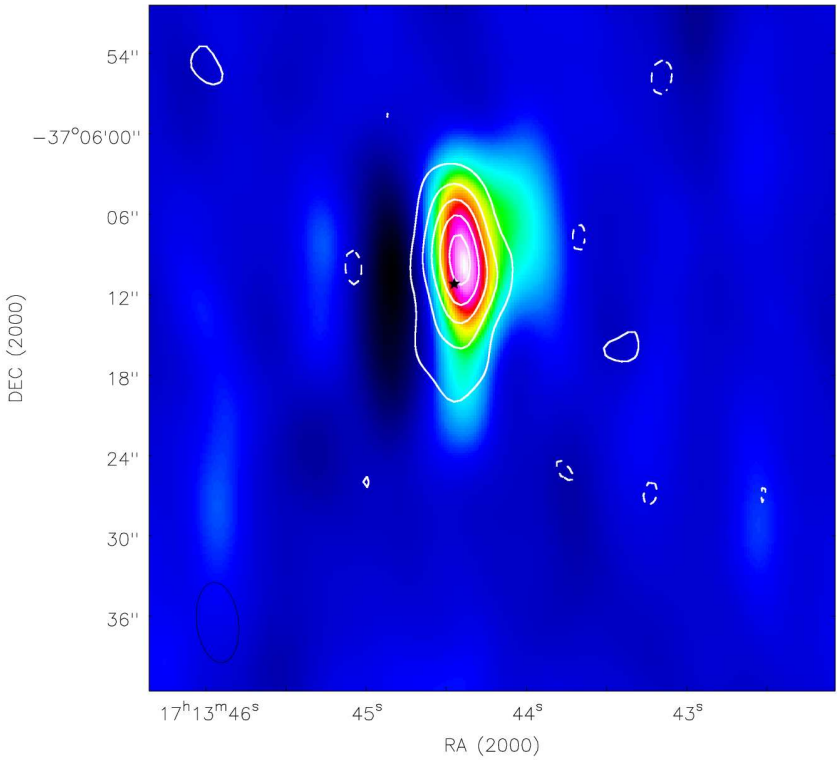

Figure 3.20: CN (J=2-1) medium velocity component integrated intensity map (contours) with ^{12}CO medium velocity component (colours). The CN integrated intensity map is from -48 to -34 km s^{-1} with a peak value of 11.97 (K km s^{-1}). Contours are from 10 to 90% in steps of 20% of the peak value. Negative contours are in dashed lines and are at 10% of the main peak value.

discussed in detail in Chapter 4 with details of the hyperfine intensities listed in Table 4.2. The ^{13}CN emission is similar in size and shape to the central (i.e. neglecting the outer, elongated emission) ^{12}CO structure, however the contours and the peak intensity of the ^{13}CN emission are shifted to the west. The elliptic nature of the ^{13}CN structure is elongated north and south but shows no further enhancement.

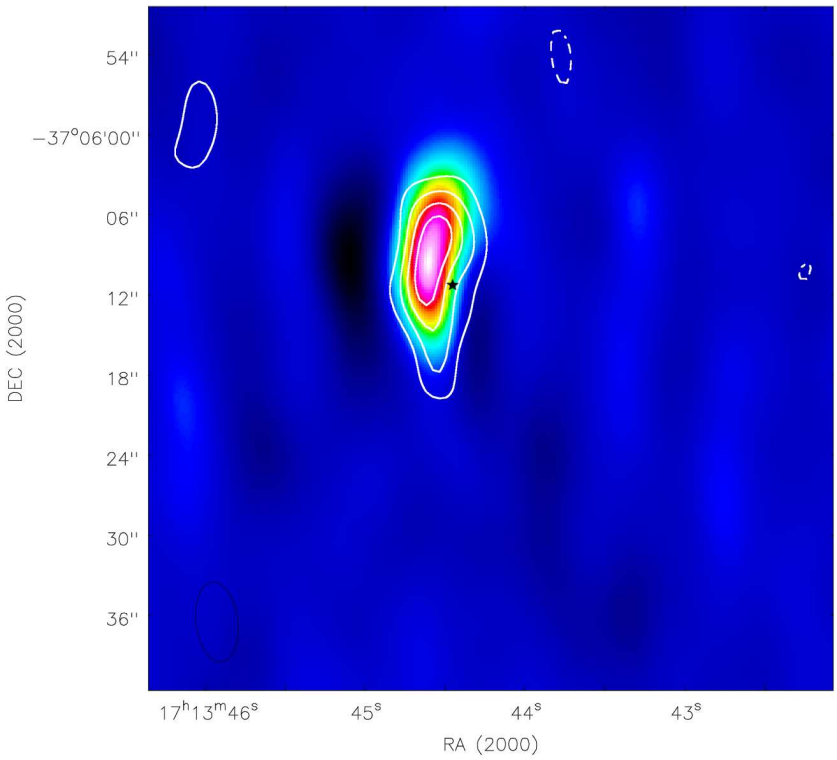

Figure 3.21: CN high velocity component integrated intensity map (contours) with ^{12}CO high velocity component (colours). The CN integrated intensity map is from -28 to -18 km s^{-1} with a peak value of 5.19 (K km s^{-1}). Contours are from 20 to 80% in steps of 20% of the peak value. Negative contours are in dashed lines and are at -20% of the main peak value.

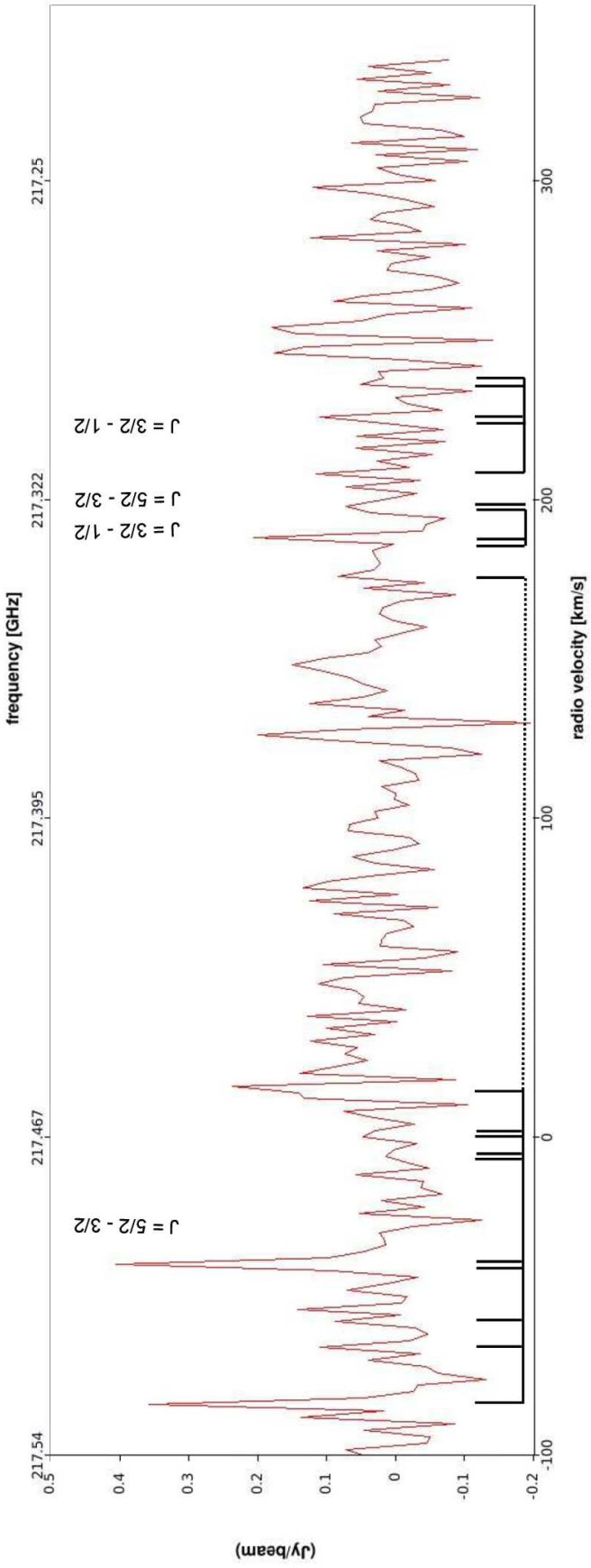

Figure 3.22: ^{13}CN spectrum showing hyperfine structure centred at 217.467 GHz. A list of hyperfine frequencies and intensities are available in Table 4.2. A low signal to noise and blending of the components is problematic for identification of the individual hyperfine components.

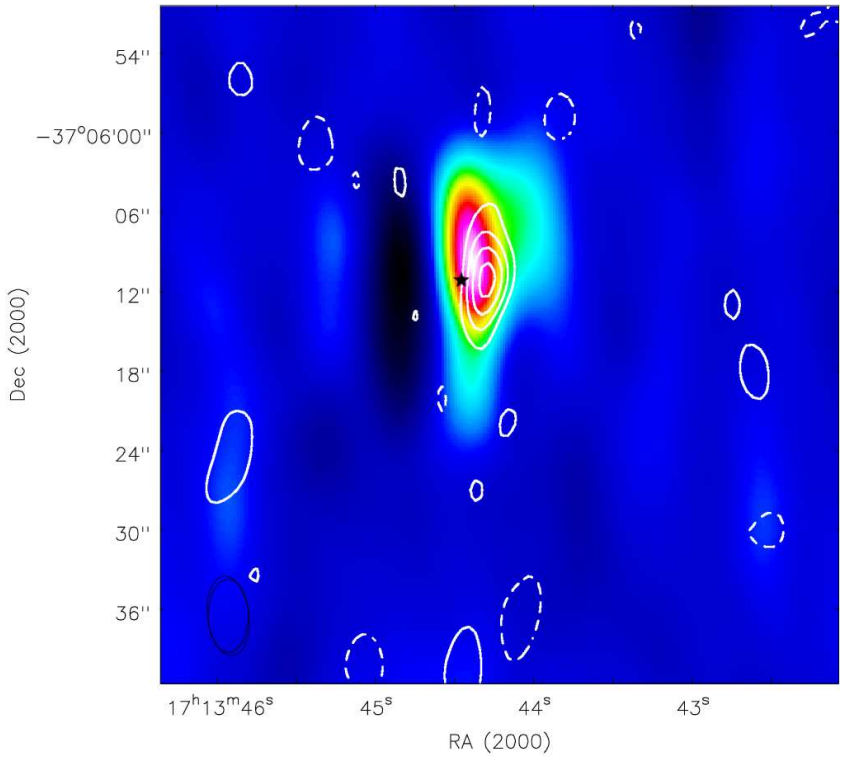

Figure 3.23: ^{13}CN (J=2-1) medium velocity component integrated intensity map (contours) with ^{12}CO medium velocity component (colours). The ^{13}CN integrated intensity map is from -40 to -38 km s^{-1} with a peak value of 1.265 (K km s^{-1}). Contours are from 30 to 90% in steps of 20% of the peak value. Negative contours are in dashed lines and are at -30% of the main peak value.

4

The Cyanide Radical and Molecular Column Densities

Millimeter-wave observations of CN have become increasingly favoured as a method of probing dense molecular gas and PDR conditions. The simultaneously observable fine and hyperfine components of the rotational transitions of CN allow for measurement of the opacity via the ratio of the line intensity of these components. Furthermore, the isotopologue ^{13}C is generally detectable within the same environment and can be utilised to calculate ^{12}C/^{13}C ratios, which is an important tracer of Galactic chemical evolution.

^{12}CN and ^{13}CN have both been observed in NGC 6302 and integrated intensity maps and spectra for the two species are detailed in the previous chapter in Section 3.3. The spectra for both species (Figures 3.18 and 3.22) show the identified hyperfine structures which are listed below in Table 4.1 for ^{12}CN and Table 4.2 for ^{13}CN. The spectrum for ^{12}CN show two fits of different velocities, used to obtain the optical depth (τ) for ^{12}CN, which is subsequently used to calculate the column density for this species (see below in §4.3). Two fits of different velocities were applied to ensure that the majority of the hyperfine components were included. τ was obtained using a method implemented

in the GILDAS data reduction software package, CLASS[1]. This method assumes the same excitation temperature for all the components of the multiplet, and that all lines have the same width. The fit is completed by supplying an input parameter file containing the number of appropriate hyperfine structures, the relative associated intensities and the positions in velocity space relative to the main component. The relative intensities of the hyperfine lines used to calculate the optical depth for ^{12}CN are taken from Saleck et al. (1994) and are also listed in Table 4.1. The relative intensities of the hyperfine lines for ^{13}CN are taken from Simon et al. (1997). Energy level diagrams for the N = 2 − 1 rotational levels for both species showing the observed hyperfine structures, are presented in Figures 4.1 and 4.2 for ^{12}CN and ^{13}CN respectively.
The ^{12}C/^{13}C ratio from observations in this work has been calculated following the methods of Savage et al. (2002) and is presented at the end of this Chapter in § 4.3.3

Table 4.1: ^{12}CN hyperfine frequencies for N = 2 - 1 transition.

Frequency (GHz)	Transition	F Component	Relative Intensity[a]
226.2988	J = 3/2 - 3/2	1/2 - 3/2	0.0049
226.3030		3/2 - 1/2	0.0049
226.3145		3/2 - 3/2	0.0120
226.3325		3/2 - 5/2	0.0053
226.3419		5/2 - 3/2	0.0053
226.3598		5/2 - 5/2	0.0280
226.6165	J = 3/2 - 1/2	1/2 - 3/2	0.0620
226.6321		3/2 - 3/2	0.0494
226.6595		5/2 - 3/2	0.1667
226.6636		1/2 - 1/2	0.0494
226.6793		3/2 - 1/2	0.0617
226.8741	J = 5/2 - 3-2	5/2 - 3/2	0.1680
226.8747		7/2 - 5/2	0.2667
226.8758		3/2 - 1/2	0.1000
226.8874		3/2 - 3/2	0.0320
226.8921		5/2 - 5/2	0.0320

[a] Saleck et al. (1994)

[1]https://www.iram.fr/IRAMFR/GILDAS/doc/html/class-html/node1.html

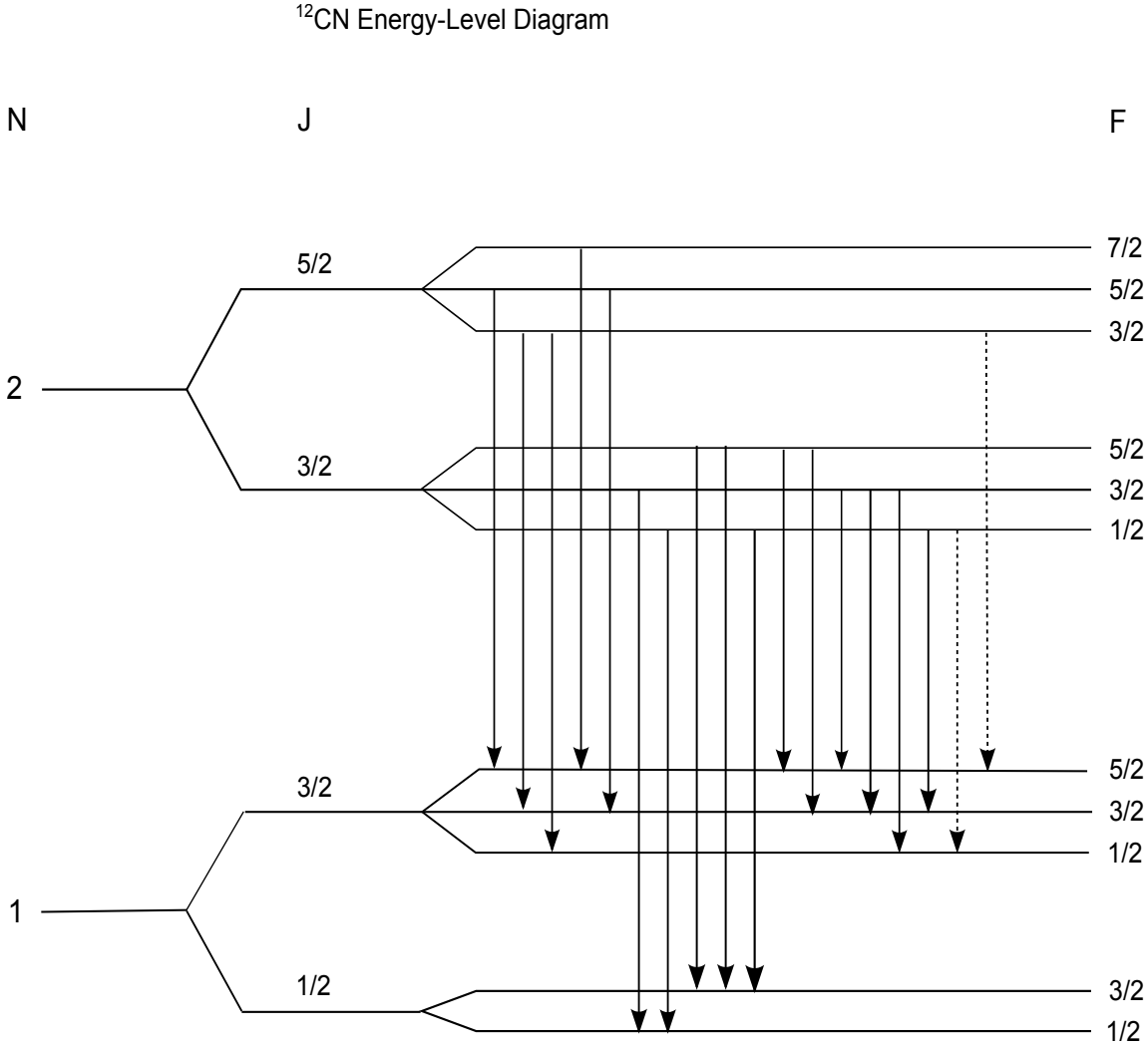

Figure 4.1: Energy level diagram of ^{12}CN for the N = 2 and 1 rotational levels. Quantum numbers J and F show the nitrogen hyperfine splittings. The observed hyperfine components in this work are indicated by solid lines. Components not observed within the N = 2-1 transition are marked with a dashed line. Transitions are ordered by frequency for easier identification.

Table 4.2: Observed ^{13}CN hyperfine frequencies for N = 2 - 1 transition

Frequency (GHz)	J′	F'_1	F′	J″	F''_1	F″	Relative Intensity[a]
217.2646	3/2	1	0	1/2	0	1	0.0100
217.2776	3/2	1	1	1/2	0	1	0.0289
217.2868	3/2	2	2	1/2	1	2	0.0201
217.2908	3/2	2	1	1/2	1	1	0.0199
217.2965	3/2	2	1	1/2	1	0	0.0264
217.2989	5/2	2	2	3/2	2	2	0.0125
217.3011	3/2	2	2	1/2	1	1	0.0594
217.3031	3/2	2	3	1/2	1	2	0.1115
217.3049	3/2	1	2	1/2	0	1	0.0441
217.3060	5/2	2	3	3/2	2	3	0.0219
217.4285	5/2	2	3	3/2	1	2	0.0889
217.4363	5/2	2	2	3/2	1	1	0.0488
217.4377	5/2	2	2	3/2	1	2	0.0146
217.4433	5/2	2	1	3/2	1	1	0.0153
217.4439	5/2	2	1	3/2	1	0	0.0216
217.4670	5/2	3	4	3/2	2	3	0.1550
217.4673	5/2	3	3	3/2	2	2	0.1068
217.4691	5/2	3	2	3/2	2	1	0.0724
217.4805	5/2	3	2	3/2	2	2	0.0138
217.4836	5/2	3	3	3/2	2	3	0.0138

[a] Simon (1997)

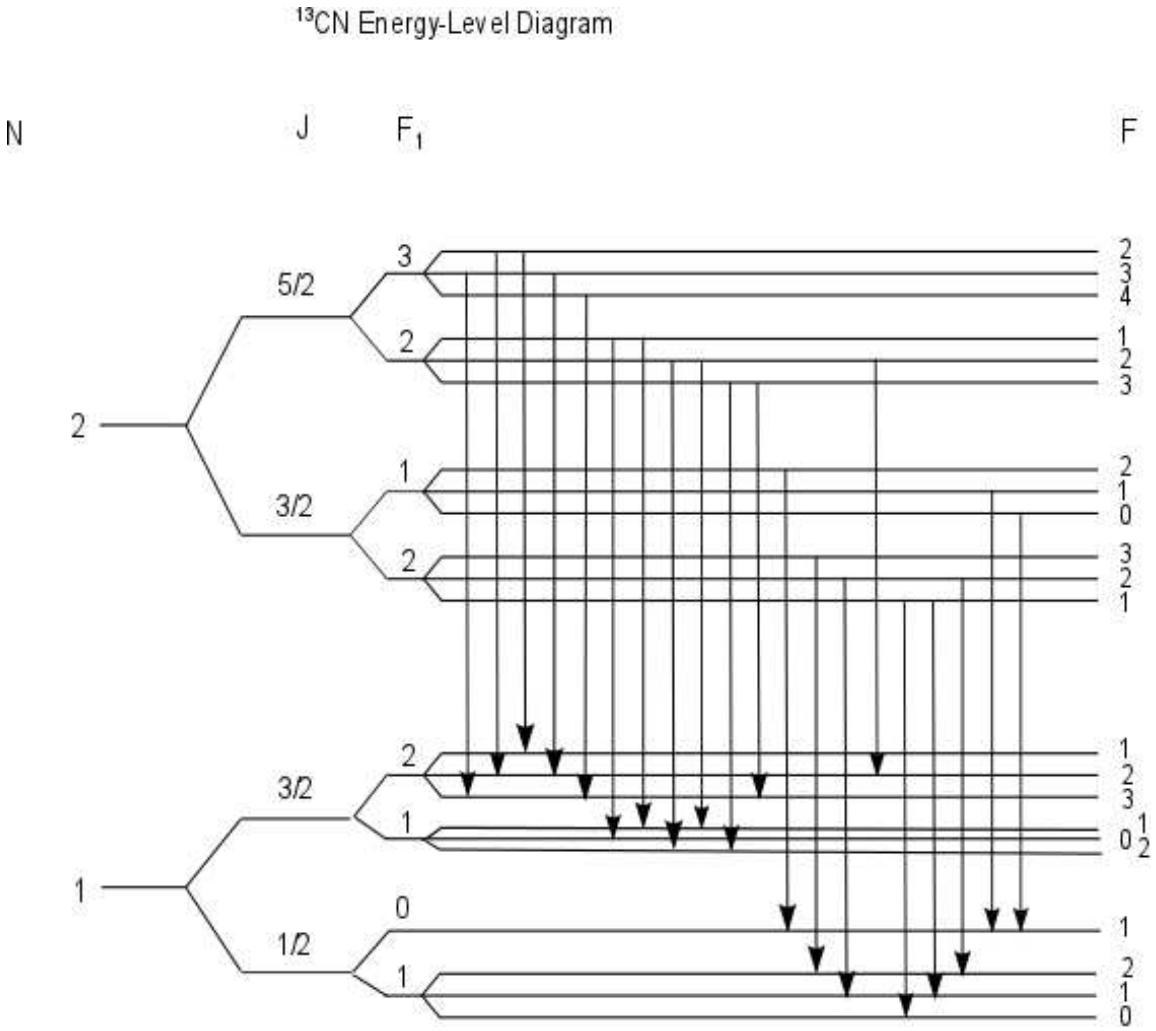

Figure 4.2: Energy level diagram of ^{13}CN for the N = 2 and 1 rotational levels, showing both the fine and hyperfine structure. The observed hyperfine components are indicated by arrows. Transitions are ordered by frequency for easier identification.

4.1 Quantum Mechanics of the CN radical

4.1.1 ^{12}CN

^{12}CN and ^{13}CN are free radicals with one unpaired electron in a σ orbit and with an electronic ground state of $X^2\Sigma^+$. The spin of the unpaired electron (S = 1/2) coupled with the nuclear spin of ^{14}N produces fine and hyperfine splitting of the rotational levels of CN, respectively. Splitting results from coupling of the different angular momenta and the relative magnitudes of the various coupling terms. Hund's coupling cases are idealised cases which approximate the actual states of many linear molecules. Of the five different coupling cases distinguished by Hund, (a) through (e), CN conforms most closely to Hund's coupling case (b), specifically ($b_{\beta J}$). A comprehensive discussion on this and associated topics can be found in Gordy and Cook (1984).

A molecule with orbital electronic angular momentum $L \neq 0$ is strongly coupled to the molecular axis by electrostatic forces. The electron spin angular momentum, **S** does not couple directly with the electrical forces unless $\Lambda \neq 0$ ($\Lambda = \mid \Sigma\lambda_i \mid$ where λ is the axial component of orbital angular momentum). In this situation the spin magnetic moment interacts with the magnetic field generated by the orbital motion directed along the bond axis. In Hund's case (b) (shown in Figure 4.3a), $\Lambda = 0$ but S $\neq$ 0, the spin moment hence becomes coupled to **N**, the axis of rotation, as the absence of an orbital field prevents coupling of the spin moment to the internuclear axis. **S** instead couples to **N** via a weak magnetic field produced by the end-over-end rotation of the molecule. **N** becomes equivalent to **R** (the rotational angular momentum of the nuclei) when $\Lambda = 0$. For each rotational level N > 1 two fine structure levels are produced as a result the spin rotation interaction, 2S + 1, when S = ½. The idealised coupling of **S** and **N** forms **J**, a total angular momentum. Each fine structure doublet is split further into hyperfine levels as, **I**, the nuclear spin of nitrogen adds to **J** to form **F** (**I** + **J** = **F**, illustrated in Figure 4.3).

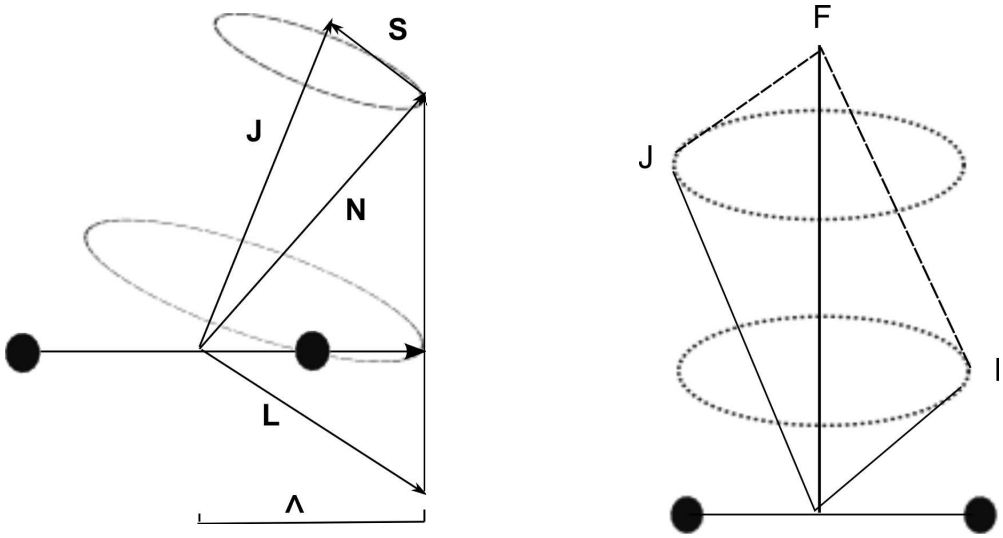

(a) Hunds Case B

(b) Hunds Case for CN

Figure 4.3: Vector diagram depicting Hund's case (b) (left) and for the case of CN, showing coupling of nuclear spin I with molecular rotational momentum J (right). Adapted from Gordy and Cook (1984).

4.1.2 ^{13}CN

In a similar manner to ^{12}CN, the spin rotation interaction also generates a fine structure doublet in ^{13}CN, however, both nuclei in this isotopologue have a nuclear spin; I_1 = ½ for the ^{13}C nucleus producing hyperfine structure of a similar magnitude, and I_2 = 1, which creates a smaller hyperfine structure for ^{14}N. ^{13}CN is now preferentially described by a combination of Hund's cases $b_{\beta J}$ described above, and $b_{\beta S}$ a coupling scheme appropriate when the hyperfine interaction between **S** and **I** is stronger than the spin-rotation coupling. In the $b_{\beta S}$ case, the ^{13}C nuclear spin couples first with the electron spin ($\mathbf{S} + \mathbf{I}_1 = \mathbf{F}_1$). **N** adds to $\mathbf{F}_1$ to form angular momentum $\mathbf{F}_2$. The total angular momentum, **F**, is completed by $\mathbf{F}_2$ coupling with $\mathbf{I}_2$, the second nuclear spin from the nitrogen atom. **F** is thus formed via, $\mathbf{N} + \mathbf{F}_1 = \mathbf{F}_2$, $\mathbf{F}_2 + \mathbf{I}_2 = \mathbf{F}$. The energy levels of ^{13}CN are represented by quantum numbers N, F_1, F_2 and F, with section rules $\Delta F_1 = 0, \pm 1$ and $\Delta F_2 = 0, \pm 1$ (Savage et al. 2002).

4.2 Radiative Transfer

The specific intensity I_ν of radiation, passing through a medium, is modified by absorption, scattering and emission. If I_ν does not depend explicitly on time, and scattering is ignored for simplicity, the radiative transfer equation for a frequency ν involving a line and continuum is,

$$\frac{dI_\nu}{ds} = j_\nu - \kappa_\nu I_\nu \tag{4.1}$$

where j_ν, the emission coefficient, or emissivity, is defined as the energy emitted per unit volume per frequency interval per unit time into a unit solid angle. For an isotropic emitter, the total energy, dE_ν radiated by volume element dV, is equal to the Power, P_ν, per unit volume (dV) per unit frequency ($d\nu$) per unit time (dt). To consider the emission coefficient in terms of P_ν and hence calculate emission per solid angle, then $j_\nu = P_\nu/4\pi$. As a formula, the emission coefficient is,

$$j_\nu = \frac{h\nu_0}{4\pi} \; N_j \, A_{ji} \, \phi_{ji}(\nu) + j_c \tag{4.2}$$

where ν_0 is the central frequency of the transition between an upper energy level j and lower energy level i. This transition has line shape function $\phi_{ji}(\nu)$ and Einstein A−value A_{ji}. The population, or number density, of the upper level is N_j. The contribution j_c is continuum emission that is taken to be a constant over the frequency range where $\phi_{ji}(\nu)$ is significantly different from zero.

The absorption coefficient κ_ν, is the reciprocal of the distance required to attenuate I_ν to $1/e$ of its original value. Its functional form is,

$$\kappa_\nu = \frac{h\nu_0}{4\pi} \left[B_{ij} \, N_i - B_{ji} \, N_j \right] \phi_{ji}(\nu) + \kappa_c \tag{4.3}$$

where we assume the same line shape for emission and absorption, and where B_{ij}, B_{ji} are respectively the Einstein B−coefficients for absorption and stimulated emission (see section 4.2.1). The term κ_c is continuum absorption and is treated as constant

across the width of the line in the same sense as j_c. For a continuum dominated by thermal processes, at temperature, T, the continuum coefficients are related by $j_\nu = \kappa_\nu B_\nu(T)$, where $B_\nu(T)$ is the planck function.

To calculate specific intensity within a medium, the solutions to the radiative transfer equation (Eq 4.1) when considering emission only, is given by

$$I_\nu(s) = I_\nu(0) + \int_0^s j_\nu(\acute{s})\, d\acute{s} \tag{4.4}$$

with the addition of the integral accounting for the emissivity varying inside the medium. In the case of absorption only, the solution for the radiative transfer equation is given by,

$$I_\nu(s) = I_\nu(0) \exp\left[-\int_0^s \kappa_\nu(\acute{s})\, d\acute{s}\right] \tag{4.5}$$

showing that the specific intensity decreases exponentially as the ray of light travels a distance, s, through the medium. If κ_ν is a constant, then Equation 4.5 can be written as $I_\nu(s) = I_\nu(0) \exp[-\kappa_\nu s]$.

The optical depth, τ is a useful quantity in which to describe the transparency of a medium and it is the integral of the absorption coefficient along the ray of light, which increases as it traverses the medium. It is hence defined as,

$$\tau_\nu(s) = \int_0^s \kappa_\nu(\acute{s})\, d\acute{s} \tag{4.6}$$

If a medium is described as optically thin, it has $\tau \ll 1$. If τ is $\gg 1$, then the medium is said to be optically thick (opaque) and attenuation of the radiation will be large. Equation 4.5 can also be written as, $I_\nu(s) = I_\nu(0)\, e^{-\tau_\nu}$ where $I_\nu(s)$ is diminished by its initial value exponentially as a function of its optical depth.

It is convenient to express the radiative transfer equation (Eq 4.1) in terms of the optical depth. In this case,

$$\frac{dI_\nu(\tau)}{d\tau} = S_\nu - I_\nu \tag{4.7}$$

where S_ν is the source function and is defined as the ratio of the emission to the absorption coefficient, $S = j_\nu/\kappa_\nu$. Multiplying both sides by e^τ gives,

$$\frac{e^\tau\, dI_\nu}{d\tau} + e^\tau\, I_\nu = e^\tau\, S_\nu \quad \rightarrow \quad \frac{d(e^\tau\, I_\nu)}{d\tau} = e^\tau\, S_\nu. \tag{4.8}$$

After substitution of values, the formal solution to Equation 4.7 is given as,

$$I_\nu(\tau) = e^{-\tau}\, I_\nu(0) + \int_0^\tau S_\nu\,(\acute{\tau})\, e^{-(\tau-\acute{\tau})}\, d\acute{\tau}. \tag{4.9}$$

which in its simplest form can be interpreted as the sum of two terms; the initial intensity reduced by absorption, plus the radiation emitted by the medium also reduced by absorption. The optical depth, τ, is zero at the surface of the medium and increases inwards.

Kirchhoff's Law states that in thermodynamic equilibrium, emission and absorption are equal $j_\nu = \kappa_\nu B_\nu(T)$, where $B_\nu(T)$ is the Planck function,

$$B_\nu(T) = \frac{2h\nu^3}{c^2}\frac{1}{e^{h\nu/kT} - 1}, \tag{4.10}$$

thus if the emission depends solely on the temperature of the emitting material, the transfer equation for thermal radiation becomes,

$$I_\nu = I_{\tau 0} e^{-\tau_\nu} + B_\nu(T)(1 - e^{-\tau_\nu}). \tag{4.11}$$

It is convenient in radio astronomy to specify the specific intensity, I_ν in terms of the equivalent blackbody brightness temperature, T_b; $I_\nu = B_\nu(T_b)$. At radio wavelengths Planck's law is well approximated by the Rayleigh-Jeans approximation, $h\nu/kT \ll 1$, given by

$$B_\nu(T) = \frac{2\nu^2}{c^2} kT_b \tag{4.12}$$

In local thermodynamical equilibrium, the excitation temperature, T_{ex} can be used in the source function to yield $S_\nu = B_\nu(T_{ex})$. Again, if the Rayleigh-Jeans approximation holds for the relevant frequency, then

$$T_B = T_{ex}\,(1 - e^{-\tau_\nu}) \tag{4.13}$$

If $\tau_\nu \gg 1$ i.e. the material is optically thick, then $T_B = T_{ex}$ and the excitation temperature is given by the observed brightness temperature directly. Conversely, if $\tau_\nu \ll 1$ then $T_B = \tau_\nu T_{ex}$.

4.2.1 Einstein Coefficients

Kirchhoff's Law (section 4.2) relates the emission and absorption of a thermal emitter on a macroscopic scale. This equivalent relationship on a microscopic level is defined by the Einstein coefficients and describes the emission and absorption of photons and the resulting interaction with matter. The Einstein coefficient for *spontaneous emission* from an upper level j to a lower level i is defined as A_{ji}, the transition probability per unit time (s^{-1}). $N_j\ A_{ji}$ is the number of spontaneous radiative decays from level j to level i per unit volume where N_j is the number of particles in level j per unit volume. The probability of a radiative transition from level i to level j per unit time, in a radiation field of mean intensity J_ν, is defined by B_{ij}, the Einstein coefficient for *absorption*, and equates to $J_\nu B_{ij}$, where $\nu = E_{ij}/h$ and E_{ij} is the energy separation between the levels. Similarly, the Einstein coefficient for *stimulated emission*, B_{ji}, from level j to level i is defined as $J_\nu B_{ji}$, where J_ν follows the notation above. Using a detailed balance of the energy level populations, it can be shown that,

$$A_{ji} = (2h\nu^3/c^2)B_{ji} \quad \text{and} \quad B_{ij} = (g_j/g_i)B_{ji} \tag{4.14}$$

where g_j and g_i are the statistical weights of the respective upper and lower levels respectively (Emerson 1996). The Einstein A and B coefficients can also be expressed in terms of the absorption and emission coefficients, as discussed above in § 4.2.

The source function (S_ν) is the ratio of the emission to the absorption coefficient, $S_\nu = j_\nu/\kappa_\nu$, by replacing j_ν and κ_ν with the definitions above (Eq. 4.2 and 4.3) and combining with equation 4.14, the line-only source function reduces to Planck's function if the energy levels are populated according to the Boltzmann distribution,

$$\frac{N_j}{N_i} = \frac{g_j}{g_i}\, e^{-E_{ij}\,/\,kT_{ex}} \quad \text{with } E_{ij} = h\nu \tag{4.15}$$

4.3 Column Densities

4.3.1 ^{12}CN and ^{13}CN

The column densities for ^{12}CN and ^{13}CN can be directly evaluated from the relative intensities of the hyperfine components of the rotational transitions. If the level populations of the hyperfine states are in LTE, the states populated are proportional to the statistical weights within a given rotational level. Calculations of column densities utilising this approach have been presented by Akyilmaz et al. (2007) (Eq. 4.16) and Savage et al. (2002) (Eq. 4.17) and has been followed for the work in this thesis. The column density N is given by,

$$N = \frac{4\pi\Delta v}{\lambda^3}\left(\frac{\pi}{\ln 2}\right)^{\frac{1}{2}} \frac{Q}{g_u A(u \rightarrow 1)} \frac{\tau}{1-\exp(-E_l/k_B T_{ex})} \frac{1}{\exp(-E_l/k_B T_{ex})} \tag{4.16}$$

In the expression above, Δv is the full width velocity of the line at half maximum intensity (of the main hyperfine component), g_u is the degeneracy (statistical weight) of the upper level of the 2 - 1 transition, A(u $\rightarrow$ l) is the spontaneous radiative transition

probability to the lower level, whose energy is E_l and Q is the partition function. The optical depth, τ, was obtained through fits to the CN spectrum and is detailed in section 4. In the case of ^{13}CN, the emission is assumed to be optically thin and a column density was derived from the following,

$$N_{tot} = \frac{\zeta_{rot} 3k10^5 T_R \Delta V_{1/2}}{8\pi^3 \nu u_0^2 R_h f} \tag{4.17}$$

where ζ_{rot} is the rotational partition function, T_R is the beam-corrected antenna temperature, ν is the frequency, u_0^2 is the dipole moment and $\Delta V_{1/2}$ is is the velocity at full width of the line at half maximum in km s^{-1}. R_{hf} is the LTE intensity ratio of a given hf component to the main line. In this instance the F = 5/2 $\rightarrow$ 3/2 was used. Column density results for both species are listed in Table 4.4.

4.3.2 HCN, HCO$^+$, CS and N_2H^+

Whilst both HCN and N_2H^+ have hyperfine structure, the components are subject to blending and not resolved in the spectra obtained for these species. Column densities for these species, plus HCO^+ and ^{13}CS, are thus calculated assuming no hyperfine structure, and with optically thin emission and with levels populated in LTE conditions. The equation (Eq. 4.18) used to derive N_{tot} follows the work of Caselli et al. (2002). An excitation temperature T_{ex} = 30 K was used and was taken from Bujarrabal et al. (2012) who present the latest temperature calculations on NGC 6302. It was found however, that increasing the excitation temperature to 100 K had little effect on column density figures. The equation by Caselli et al. (2002) assumes that all lines are optically thin and that all rotational levels are characterised by the same excitation temperature

$$N_{tot} = \frac{8\pi W}{\lambda^3 A} \frac{g_l}{g_u} \frac{1}{J_\nu(T_{ex}) - J_\nu(T_{bg})} \frac{1}{1 - \exp(-h\nu/kT_{ex})} \frac{Q_{rot}}{g_l \exp(-E_l/kT_{ex})} \tag{4.18}$$

where $J_T = T_0/[\exp(T_0/T) - 1]$ and $T_0 = (E_u - E_l)/k$, A is the Einstein coefficient

and g_u and g_l are the statistical weight of the upper and lower levels respectively. Q_{rot} is the partition function, E_l is the energy of the lower level and *k* is the Boltzmann constant. The integrated intensities, *W*, were derived from Gaussian fitting of the main line profile and for species with 'wing' emission, *W*, refers to the sum of the integrated intensities of each velocity component. The parameters and values used to determine N_{tot} for each species, are listed in Table 4.3. Table 4.4 lists the calculated column densities for the detected species in this work, with comparisons of N_{tot} for NGC 7027 (Zhang et al. 2008) and the Red Spider Nebula (NGC 6537) (Edwards and Ziurys 2013). The column densities of CN, ^{13}CN and ^{13}CS are similar for all three PN. The column density of HCO^+ is an order of magnitude greater in NGC 7027 and exactly one order of magnitude lower in NGC 6537 than in NGC 6302. A similar pattern can be observed for HCN, albeit figures for NGC 6537 are a factor of 4 lower. N_2H^+ again is more abundant in NGC 7027 and a factor of 2 lower than NGC 6302.

Table 4.3: Column density parameters used to determine N_{tot}, for each molecular species observed (except ^{12}CN and ^{13}CN) using equation from Caselli et al. (2002). Integrated intensity includes central line profile emission and any 'wing' emission. An excitation temperature of 30 K was used for all species.

Molecule	Transition	Q_{rot}	B	Integrated Intensity (K km s^{-1})
HCO^+	3 - 2	12.02	44.594	37.73 (± 0.3)
HCN	3 - 2	12.09	44.315	30.66 (± 0.3)
^{13}CS	6 - 5	22.86	23.754	4.16 (± 0.1)
N_2H^+	3 - 2	11.52	46.587	3.07 (± 0.1)

4.3.3 ^{12}C/^{13}C Ratios

While ^{12}C is formed predominantly via the triple alpha process, ^{13}C formation is a secondary process, arising via the CNO cycle and occurs primarily in the red giant/supergiant phases. These differing mechanisms thus provide constraints on interior stellar processes and are used to trace Galactic chemical evolution. Typical values for the abun-

Table 4.4: Column densities for observed molecular species in NGC 6302 calculated in this work, with comparative data on N_{tot} in other PNe, specifically The Red Spider Nebula (NGC 6537) and NGC 7027.

Molecule	Frequency (GHz)	Transition	N_{tot} (cm^{-2})[a]	NGC 6537[b]	NGC 7027[c]	Notes
CN	226.874	2 - 1	4.40 (13)	1.6 (13)	1.02 (13)	
^{13}CN	217.4671	2 - 1	4.3 (12)	8.3 (12)	...	
HCN	265.886	3 - 2	2.3 (13)	5.5 (12)	7.05 (14)	
HCO^+	267.557	3 - 2	2.3 (13)	2.3 (12)	3.38 (14)[d]	[d] refers to HCO^+ transition J = 1 − 0 in [c]
^{13}CS	277.455	6 - 5	6.9 (12)	9.9 (12)[e]	...	[e] refers to CS transition J = 5 − 4 in [b]
N_2H^+	279.511	2 - 1	1.6 (12)	6.9 (11)[f]	2.43 (13)	[f] refers to N_2H^+ transition J= 3 - 2 in [b]

[a] All column densities in the form; a(b) = a x 10^b
[b] Edwards and Ziurys (2013)
[c] Zhang et al. (2008)

dance ratios for the local ISM are 69 ± 6 and in PDRs such as the Orion Bar, a somewhat lower abundance ratio of 59 ± 18 is derived (Savage et al. 2002). In a study aimed at determining the $^{12}C/^{13}C$ ratio in PNe through millimeter wave observations of $^{12}CO/^{13}CO$, Palla et al. (2000) determined a range of values between 9 and 23. Palla et al. (2000) suggest that non-standard mixing processes in the progenitors of the PNe must have occurred during the red giant and/or asymptotic giant phase, to significantly mix ^{13}C and transport it to the surface layers. In recent observations of the Red Spider Nebula, Edwards and Ziurys (2013) obtained a $^{12}C/^{13}C$ ratio of ~ 4 and similarly invoke hot-bottom burning to account for the low ratio.

The method used in this work to obtain $^{12}C/^{13}C$ ratios, follows that of Savage et al. (2002) and is detailed in Equation 4.19,

$$\frac{^{12}C}{^{13}C} = \frac{(3/5)\,\tau_{main}\,T_{ex}\,(^{12}CN)}{T_R^*/\eta_c\,(^{13}CN)}, \tag{4.19}$$

where T^*_R is the line temperature measured from the observed spectra and η_c is the beam efficiency. In this work T^*_R is the brightest hyperfine line for ^{13}CN, and corresponds to transition F_1 3−2. τ_{main} is the optical depth in the main hyperfine line for ^{12}CN and was obtained through fits to the ^{12}CN spectrum described above in Section 4. T_{ex} for ^{12}CN is also calculated following the equation of Savage et al. (2002), by

$$\frac{T_R^*}{\eta_c} = (T_{ex} - T_{bg})(1 - \exp^{R_{hf}\tau_{main}}) \tag{4.20}$$

where T_{bg} is the cosmic background temperature (T_{bg} = 2.73 K) and R_{hf} is the LTE intensity ratio of the given hyperfine component to the main line (F = 5/2 − 3/2). The value obtained using equation 4.19 is 18.8 (± 10). The ^{12}C/^{13}C ratio calculation assumes that both CN isotopomers undergo the same degree of excitation, occupy the same volume and are not subject to chemical anomalies. Anomalies refer to processes such as isotope-selective photodissociation, whereby ^{12}C is preferentially favoured over its isotopomer counterpart due to self shielding in regions of high UV flux (Savage et al. 2002).

This ratio is within the values obtained by Palla et al. (2000) for other PNe and is higher than the ^{12}CO J = 2 → 1 and ^{13}CO J = 2 → 1 observations by Peretto et al. (2007) (see §1.4 and §3.2.1). Peretto et al. (2007) derive a lower limit of 15 for the ^{12}CO/^{13}CO abundance ratio, and hence by association the ^{12}C/^{13}C ratio.

5

The Meudon PDR Code

5.1 The Meudon PDR Code

The Meudon PDR code has been an important tool used for modelling and has been utilised as an aid in the analysis of chemical abundances for comparison against observations. The code is primarily aimed at solving chemistry for photon-dominated regions (PDR) and is a steady state, one dimensional code[1]. A thorough review is given by Le Petit et al. (2006).

The model considers a stationary plane-parallel slab of gas and dust, irradiated on one or both sides of the cloud by the interstellar standard radiation field (ISRF), the intensities of which can be different on each side (see Fig 5.1 for a schematic representation). The radiation field from a star can also be added, either via known stellar spectra recognised by the code or via an external file supplied by the user. The addition of the stellar radiation has consequential implications for the chemistry, as due to the geometry of the code the radiation is viewed unidirectional to the surface of the slab of gas whereas the ISRF is isotropic. The code runs iteratively using the discrete transitions of H and H_2 and absorption in the continuum by dust to solve the radiative

[1] Available from http://aristote.obspm.fr/MIS.

transfer in the UV at each point in the cloud. Specific treatment is also given to H_2 and HD photodissociation, C and S photoionisation and CO predissociating lines in the calculations. Thermal balance is also computed via heating mechanisms such as photoelectric effect on dust grains and cosmic rays, which are counteracted with cooling processes of infrared and millimetre emission of the available dust, atoms, ions and molecules. In a similar iterative manner the chemistry is computed, with abundances of species calculated at each point. On completion of the main code, a post processor tool can be used to extract the specific information, including emissivities/intensities, cloud temperatures and molecular abundances. The steady-state approximation of the Meudon PDR code is its major limitation, nonetheless, the steady-state nature is compensated for, as photoprocesses in high radiation fields (and/or lower extinctions) are typically shorter than timescales for two-body chemical reactions in a diffuse environment.

5.1.1 Parameters

Density and temperature are the two most important physical quantities considered in the Meudon code, both of which can be user defined and both can be computed in different ways. Specific temperature and density models include; isothermal, constant density and isobaric. User defined density and temperature profiles can also be added via an input file. Density is defined as the total number of hydrogen nuclei $n_H = n(H) + 2n(H_2) + n(H^+)$ cm^{-3}. The user is similarly able to define a number of other parameters within the code. The details of which are listed in Table 5.1.

The specific photon intensity of the average interstellar FUV field given by Draine (1978) is adopted with revisions by Sternberg and Dalgarno (1995) to calculate the UV radiation field

$$I(\lambda) = \frac{1}{4\pi}\left(\frac{6.300x10^7}{\lambda^4} - \frac{1.0237x10^{11}}{\lambda^5} + \frac{4.0812x10^{13}}{\lambda^6}\right) \quad (5.1)$$

Table 5.1: Meudon Model Parameters

Parameter	Units	Description
n_H	cm^{-3}	Total hydrogen density
χ	Draine	FUV radiation strength
A_V	mag	Extinction (total cloud depth)
ζ	10^{-17} s^{-1}	Cosmic-ray ionisation rate
T	K	Initial Temperature
Star	None	Additional plane parallel radiation field (optional)
d_*	pc	Distance from star to cloud surface (if applicable)
P	K cm^{-3}	Thermal Pressure
v_{turb}	cm s^{-1}	Turbulent velocity

where λ is in Å and I in ergs cm^{-2} s^{-1} sr^{-1} $Å^{-1}$ and is used from the Lyman cutoff up to λ 2000 Å given by Draine (1978). For longer wavelengths, the following is used;

$$I(\lambda) = 1.38243x10^{-5}\lambda^{-0.3} \text{ ergs cm}^{-2}\text{s}^{-1}\text{sr}^{-1}\text{Å}^{-1} \tag{5.2}$$

If the radiation field is isotropic I = J, whereby J(λ) is the derived mean intensity in ergs cm^{-2} s^{-1} $Å^{-1}$ and is defined by,

$$J(\lambda) = \frac{1}{4\pi}\int I(\lambda)d\Omega \tag{5.3}$$

However, the energy density of the radiation field $u(\lambda)$ (in ergs cm^{-3} $Å^{-1}$) is used to compute most of the physical quantities which are radiation field dependant,

$$u(\lambda) = \frac{1}{c}\int I(\lambda)d\Omega = \frac{4\pi}{c}\, J(\lambda) \tag{5.4}$$

The radiation field can be scaled by the user, by a scaling factor χ, in the parameter input field. An additional radiation field can also be applied via the Star parameter, which is calculated as a diluted blackbody and is characterised by its radius R_*, its distance to the PDR surface d_* and its effective temperature T_{eff}.

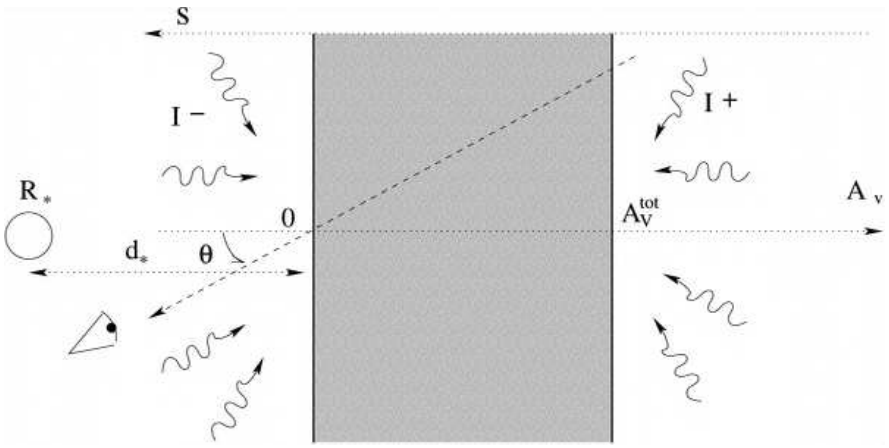

Figure 5.1: Schematic interpretation of the structure and geometry conventions of the Meudon code

5.1.2 Code Structure

All quantities of the PDR code (chemical and physical) are dependant upon one spatial coordinate, the dust optical depth at visible wavelengths, τ_v, calculated perpendicular to the PDR surface. Limitations surrounding the structure of the code impose restrictions on the calculation of the physical equations. As the optical depth τ_V increases, attenuation of the radiation field reduces the energy density in the cloud, consequently conditions at locations closer to the impinging radiation source require different treatment than deeper parts of the cloud. Accordingly, thermal and chemical balance and radiation transfer are solved through an iterative process, whereby the whole cloud structure calculated at step i is used to refine the model at step $i + 1$. At each iteration, the following processes are treated in order; (i) radiative transfer in the UV, (ii) chemistry and (iii) level populations and thermal balance; these processes are described in more detail below under the appropriate heading. A thorough treatment of radiative transfer requires an embedded second level of iteration to be performed, as radiative transfer is dependant on species population which in turn is dependant on temperature. Steep variations in the optical depth τ_V, at locations such as the H/H_2 transition where abundances of both species can vary substantially, are accounted for by the use of an adaptable logarithmic spatial grid. This ensures that the relative variations of the main

physical quantities do not exceed a predefined threshold as the size of each τ_V step is calculated.

5.1.3 Grain Properties

Dust grains in astrophysical environments are not only a platform for a host of chemical reactions, including the main formation route of H_2, but they participate in thermal balancing of a PDR through photoelectric heating and collisions with the gas. In addition, dust grains determine the cloud extinction curve required for the calculation of UV radiative transfer. In the code, grains are characterised by a mass density of g cm^{-3} and a gas to dust ratio of $C_D = N(H) + 2\ x\ N(H_2)/E(B-V)$ (in cm^{-2} and mag^{-1}). A number of additional grain properties are used to determine their influence on the cloud structure and chemistry as follows; the optical depth due to dust at a wavelength λ is given by

$$\tau_\lambda = \left[1 + \frac{1}{R_V}\ \frac{E(\lambda - V)}{E(B-V)}\right]\ \frac{A_V}{2.5\log(e)} \tag{5.5}$$

whereby the parameterization of Fitzpatrick and Massa (1990) is used for the standard extinction curve. Specific parameters depending on the adopted environment can be added to an input file to provide new lines of sight if required. The grain size distribution follows Mathis et al. (1977), which is a power-law function, $dn(a) \propto a^{\propto}\ da$, where the number of grains per unit of volume $dn(a)$ have a radius between a and $a + da$ and the index of the distribution law $\propto$ = -3.5. The grain absorption cross sections are taken from Draine and Lee (1984) and Laor and Draine (1993). The spectroscopic properties of the graphite and silicate particles are determined experimentally and are mixed proportionally within the code. Spherical grains with radii between 1 nm and 10 μm are considered, whilst those with radii smaller than 50 nm are treated as polycyclic aromatic hydrocarbons (PAH) properties. Finally, dust absorption and attenuation are calculated via the dust albedo, ω, and diffusion factor, g, parameters respectively. The Meudon PDR code treats these parameters as constants, as within the wavelength range

912−2000*AA* these parameters do change significantly. The typical value for albedo is 0.42 (from Mathis (1996)), whilst the diffusion factor, g, is the mean cosine of the angle of diffusion, θ and its typical value is 0.6 (from Weingartner and Draine (2001)). Table 5.2 displays the main dust parameters and values for the parameters listed above.

Table 5.2: Meudon Dust Grain Parameters

Parameter	Units	Description	Typical Value
a_{min}	cm	Lower size cutoff	3 x 10^{-7}
a_{max}	cm	Upper size cutoff	3 x 10^{-5}
d	cm	Mean distance between adsorption sites	2.6 x 10^{-8}
$\propto$	None	Distribution law index	-3.5
ω	None	Dust Albedo	0.42
G_r	None	M_{grain}/M_{gas}	0.01
ρ_{gr}	g cm^{-3}	Grain volumetric mass	3
R_V		A_V/E_{B-V}	3.1
C_D	cm^{-2} mag^{-1}	$N(H_2)/E_{B-V}$	5.8 x 10^{21}

5.1.4 UV Radiative Transfer

Due to the intensive computational requirements needed to calculate the radiative transfer equation over a wide wavelength range associated with a PDR, the code assumes a number of conditions; firstly the impinging UV radiation is separated from the outgoing (IR and millimetre) radiation emitted by the dust grains. No internal UV sources are allowed, instead scattering or pure absorption followed by emission at UV wavelengths is solved. Cooling in the cloud is assumed to be an 'on-the-spot' approximation whereby redistribution of radiation effects are neglected and photons are considered to either escape from the cloud or be reabsorbed from their emitted location, see Gonzalez Garcia et al. (2008) for further information in regards to this process. Accordingly level populations can only be calculated from local quantities at a given point in the cloud. The full transfer equation along a line of sight can finally

be solved at the post-processing phase to obtain line profiles and integrated intensities, when temperature, abundances and their level populations have been calculated at each point inside the cloud.

Radiation Field Properties

The external UV radiation field is determined by Draine (1978) and is detailed above in section 5.1.1. The spherical harmonics method by Roberge (1983) is used to solve the radiative transfer equation via application of a variable grid of wavelengths to maintain accuracy whilst limiting CPU requirements. The grid is constructed with a number of either physical values (line positions, ionisation thresholds) or imposed wavelengths from external input files and is applied to a plane-parallel cloud with elastic scattering in order that dependance on wavelength can be ignored. The transfer equation is given by

$$\mu \frac{\partial I(r,\mu)}{\partial s} = -(\kappa_\lambda + \sigma_\lambda) I(r,\mu) + \frac{\sigma_\lambda}{2} \int_{-1}^{+1} p(\mu,\acute{\mu}) I(r,\acute{\mu}) d\acute{\mu} \tag{5.6}$$

where $\mu = \cos\theta$, and θ is the angle between the direction of propagation of a beam of radiation and then perpendicular to the slab of gas (see Figure 5.1) and s is the curvilinear abscissa in the perpendicular direction to the gas. $I(r,\mu)$ is the specific intensity in ergs s^{-1} cm^{-2} sr^{-1} $Å^{-1}$ at position r in the direction μ, whilst σ_λ is the dust scattering coefficient (cm^{-1}) and κ_λ is the total absorption coefficient (dust plus gas) also in cm^{-1}. $p(\mu,\acute{\mu})$ is the dust angular redistribution function of the radiation field.

In order to model a PDR region effectively, the precise treatment of the H/H_2 transition zone is required, which is primarily governed by the calculation of H_2 self shielding. In the code, this is performed in one of two ways; an approximated method based on Federman et al. (1979) to calculate the self-shielding effects for H_2 and CO. If explicit information on H and H_2 is not required then an exact method by Goicoechea and Le Bourlot (2007) can be selected. This latter method allows for rigorous calculation of

overlapping effects and radiative transfer is solved explicitly at each specified wavelength. The former method utilises contribution by dust extinction but approximates the calculation of absorption in H_2 lines and does not take into account overlapping of lines of any chemical species. Assuming a one-sided model for simplification, the energy density at wavelength λ, at any point in the cloud is calculated as (Federman et al. 1979);

$$u_\lambda(\tau) = u_\lambda^0 D_\lambda \sum_X L_\lambda(N(X)) \tag{5.7}$$

where u_λ^0 is the energy density at the edge of the cloud, D_λ is dust absorption at position at τ_ν, X is the chemical species in question and $L_\lambda(N(X))$ is the absorption of species X with a column density N(X) from the cloud edge to position τ_ν. Upon evaluation of the absorption variables, the radiative transfer equation becomes,

$$\mu \frac{\partial I(\tau,\mu)}{\partial \tau} = I(\tau,\mu) - S(\tau,\mu) \tag{5.8}$$

with S, the source function;

$$S(\tau,\mu) = \frac{\omega(\tau)}{2} \int_{-1}^{+1} p(\mu,\acute{\mu}) I(\tau,\acute{\mu}) d\mu \tag{5.9}$$

The escape probability of secondary UV photons within the cloud, is computed using the method of Flannery et al. (1980), an ”on-the-spot approximation” whereby photons are assumed to be absorbed from their emitted location, if they did not escape the cloud. The shortcoming of this approximation is an underestimation of the energy loss, thus slightly changing the level population of species at that point.

5.1.5 Thermal Balance

Heating Processes

The temperature and hence the chemical structure of a PDR is controlled by the incident FUV photons which drive the chemistry through two main heating processes, H_2

formation on grains and photoelectric heating via ejection of electrons of small dust grains and PAHs. The models by Bakes and Tielens (1994) of the size distribution of interstellar grains and their contribution to the heating of the gas by the photoelectric effect are followed by the Meudon code, with some adaptations, including the grain absorption coefficients which are taken from Laor and Draine (1993), and the charge distribution which is calculated for each grain size. H_2 forms by the association of hydrogen atoms on the surface of dust grains via: H + H + gr. $\rightarrow$ H_2 + gr., and whilst some fraction of the formation energy (~4.5 eV) is retained in vibrational excitation of the H_2 molecule, the energy distribution between internal energy, grain excitation and the kinetic energy of the molecule is unknown. As such, the repartition energy of H_2 formation in the code is split evenly between these processes. Although a number of options are available to determine how the internal energy is spread within the levels via the *iforh2* parameter, only one is recommended and is calculated as,

$$E_{int} = \frac{\sum_{n=1}^{n_{max}} E_n \, g_n \, \exp(-\frac{E_a}{kT_{ex}})}{\sum_{n=1}^{n_{max}} g_n \, \exp(-\frac{E_a}{kT_{ex}})} \tag{5.10}$$

where E_n is the energy of level n, g_n is its statistical weight and n_{max} is the highest H_2 ro-vibrational level. The photodissociation of H_2 at a PDR surface is an important factor in gas heating and is assumed by the code to yield a mean kinetic energy of $\sim$ 1 eV (Abgrall et al. 2000) along with HD, CO and its isotopes. As dissociation is not always expected, the photodissociation probability and abundance of species involved (at that point) are multiplied with the mean kinetic energy to calculate the actual energy input. A mean photon energy of 13 eV is assumed for other chemical species. Further heating is provided by: kinetic energy via molecular formation and atomic ionisation. 4 eV by cosmic rays are also assumed. The ions produced in highly exothermic dissociative recombination reactions and ion-neutral reactions via cosmic rays provide the primary source of heating in the code at large A_V. The rest is provided for by the difference in enthalpies of the products and reactants in chemical reactions, which becomes important in cold, dark regions where the photon flux is diminished.

Cooling Processes

Discrete radiative transitions in lines of C, O, S, Si, C^+, N^+, Si^+, HCO^+, CO, CS, H_2 and HD provide the cooling in the code. Calculations are performed on a detailed balance of the energy level populations produced by: chemical formation and destruction, radiative decay, collisional transitions and cosmic microwave background interactions. The cooling properties of C^+ accounts for the majority of the cooling at lower magnitudes ($\lesssim 3$ A_V), whilst photons crossing through the C^+/C transition zone are essentially able to escape to the edge of the cloud to participate in cooling at larger A_V. H_2 is important in both heating and cooling processes within a PDR. Collisional de-excitation of the vibrational levels after FUV pumping of H_2 heats the gas, whilst radiative quadrupole decay following collisional vibrational excitation cools the gas. Additional consideration when calculating the balance in H_2 levels is also given to collisional transitions with H, H_2, He, H^+ and H_3^+ and level specific formation on grains.

5.1.6 Chemistry

The penetrating FUV photons near the edge of a PDR keep hydrogen and oxygen atomic and carbon ionised. Molecular hydrogen, once formed, reacts quickly with species such as C^+, O and OH which have small activation energies and thus chemical reactions can proliferate at an appreciable rate in the warm, dense gas of a PDR. Chemical aspects including abundances and column densities, can all be analysed after convergence has been reached for radiative transfer, thermal balance and chemical equilibrium. These can all be determined at each point in the cloud with the post-processor tool. Chemical species and reactions are read from an input file supplied with the code. The file lists 134 species including neutral and cationic species. As standard, no anion species are included. Two variations of the chemistry file can be downloaded, one including deuterated species and the other without. The species are involved in 2652 reactions and specific reaction are described below. Chemical balance is obtained for each species X via

$$\frac{dn(X)}{dt} = F_X - D_X \equiv 0 \tag{5.11}$$

where F_X is the formation rate and D_X is the destruction rate. The majority of reactions follow an Arrhenius law and for each reaction chemical rates are calculated from three parameters, α, β and γ,

$$k = \gamma \left(\frac{T_K}{300}^{\alpha} \right) \exp(-\beta/T_K) \text{ cm}^3 \text{ s}^{-1} \tag{5.12}$$

with k the chemical rate at a specific point in the cloud at temperature T_K. Gas phase reactions are only considered in the Meudon PDR code, as temperatures are considered to high in a PDR for species to freeze out onto grains. H_2 is the notable exception as gas phase reactions are notoriously too slow, so formation on grains is generally assumed to be the dominant pathway. The different categories of reactions are listed in Table 5.3.

Table 5.3: Generic gas phase reactions important in PDRs and typical rates. Table adapted from Tielens (2005)

Name	Reaction	Rate Coefficients	Unit	Note
Photodissociation	AB + hν $\rightarrow$ A + B	10^{-9}	s^{-1}	(a)
Neutral-neutral	A + B $\rightarrow$ C + D	4 x 10^{-11}	cm^3 s^{-1}	(b)
Ion-molecule	A^+ + B $\rightarrow$ C^+ + D	2 x 10^{-9}	cm^3 s^{-1}	(c)
Charge-transfer	A^+ + B $\rightarrow$ A + B^+	10^{-9}	cm^3 s^{-1}	(c)
Radiative association	A + B $\rightarrow$ AB + hν			(d)
Dissociative recombination	A^+ + e $\rightarrow$ C + D	10^{-7}	cm^3 s^{-1}	

(a) Rate in the unshielded radiation field
(b) Rate in the exothermic direction and assuming no activation barrier
(c) Rate in the exothermic direction
(d) Rate highly reaction specific

5.2 Discussion of Chemical Models of PNe

The first chemical models of PN environments were presented by Black (1978) who predicted the existence of a number of diatomic molecules such as H_2, H_2^+, HeH^+, CH^+ and OH through modelling ionised gas in the H^+/H^0 transition zone. A number of other authors including Howe et al. (1994), Yan et al. (1999), Natta and Hollenbach (1998), Hasegawa et al. (2000), Ali et al. (2001) and most recently Kimura et al. (2012) have all used models in order to investigate the varying phenomena within PNe. Howe et al. (1994) model molecule formation in dense globules (indicative of evolved PN) and predict appreciable quantities of C_2H and CN if the gas is carbon-rich.

The neutral envelope of NGC 7027 is investigated by both Yan et al. (1999) and Hasegawa et al. (2000) who utilised chemical steady-state models of a semi-infinite slab approximation and spherical symmetric model, respectively, of a thin, dense shell and an outer stellar wind region. Yan et al. (1999), who presented a thermal-chemical model, concluded that CH^+, OH, CH and high-J CO lines originate from a high-temperature ($\sim$ 1000 K), dense PDR. Similarly Hasegawa et al. (2000), also conclude that high temperatures (for the same species) and a combination with photo-chemistry (for HCO^+ and CO^+) can explain the observed abundances in NGC 7027. Hasegawa et al. (2000) also state that molecular formation is occurring within timescales of less than 100 yrs due to photodissociation in the neutral envelope.

Natta and Hollenbach (1998) examine the effects of FUV (6 eV $<$ hν $<$ 13.6 eV), soft X rays (50 eV $\lesssim$ hν $<$ 1 keV) and shocks on predominantly neutral gas. They determine that whilst FUV photons influence early PN evolution, soft X-rays are dominant in latter stage PN formation. Ali et al. (2001) construct pseudo-time-dependant models of cool, dense, C-rich clumps in neutral envelopes, for comparison against observations of three evolved PN: NGC 6781, M4-9 and NGC 7293. Their results suggest that an enhanced ionisation rate from X-ray emission is required to match ob-

servations of species such as HCN, HNC, HC_3N and SiC_2. Additionally a number of molecular species including CH, CH_2, CH^+2, OH and H_2O should be prevalent in the PNe. Kimura et al. (2012) probe chemical formation in cold regions beyond the ionised zone, using a self-consistent photoionisation numerical code. In conjunction with previous authors, their models also required X-ray emission to account for the molecular composition of their modelled gas.

5.3 Meudon Models

For modelling a PNe, the Meudon code has the advantage of being able to add an external stellar spectrum to the parameter input file, thus emulating the conditions within a planetary nebula. The stellar spectrum is limited however to the range of values accepted for the radius and temperature of the added source. NGC 6302 is described as being one of the highest ionized known PN, with a central star temperature of $\sim$ 150, 000 (Groves et al. 2002) to 430, 000 K (Ashley and Hyland 1988). Additionally, as a PN evolving to a white dwarf, its previous estimated progenitor mass (4-5 $M_\odot$) would therefore be no longer applicable and a reduced-mass star was initially selected. A central star mass of 0.73−0.82 was found by Wright et al. (2011) who compared the properties of NGC 6302 from their models, with those from late-thermal pulse (LTP) models to ascertain its evolution. A series of models were then run to establish which parameters accepted by the code would best fit the PN at its current evolution status.

Starting with the lowest calculated temperature (150, 000K), the star temperature parameter was increased incrementally in steps of 10, 000K (up to 200, 000 K) and mass increased in steps of 0.1 (from 0.8 $M_\odot$). It was found, that a star of 1 solar mass and temperature of 150, 000 K provided the best fit to the observed column densities for the majority of species within the standard models (ModA). With the temperature and radius set for the star input file, models were then constructed changing a parameter at a time, to establish its effect on the chemistry. Parameters that remain unchanged in-

clude the hydrogen density (n_H), set at 5.5 x 10^4 cm^{-3} and the starting gas temperature, which is set at 20 K for all models. Varying the initial temperature up to 100 K had no overall effect on the final column density figure.

The chemistry file utilised in the following models was downloaded with the Meudon PDR code. The chemistry file consists of 134 chemical species and 2652 reactions compiled from UDfA[2], the OSU[3] database and from the literature. The vast majority of the reactions, however, are from the UDfA. A few select abundances and some reaction rates have been altered to probe varying conditions, details of which are listed below and in Table 5.4. The chemistry was allowed to evolve to a maximum A_V = 20 to highlight any peculiarities or anomalies with increasing extinction. A few authors have already calculated the extinction via differing methods, notably Matsuura et al. (2005) and Szyszka et al. (2009) and both have reported high extinction towards the torus of NGC 6302. Matsuura et al. (2005) derive A_V = 6-8 from the ratio map of Hα to radio flux. This is echoed by Szyszka et al. (2009) who find a similar value of A_V = 6.6 by comparing the (4690−6766 Å) colour of the two photometric points with that of a star of a given blackbody temperature subjected to line-of-sight extinction. As such, the comparison of modelled column densities figures with those calculated from observations in this work are presented at A_V = 7−8. Column density figures are presented for both magnitudes, as abundances for some molecular species is seen to increase around an A_V of 7−8 (see below).

A grid of models with varying parameters were constructed in order to model column densities comparable to the calculated column densities of NGC 6302 and thus ascertain the likely conditions of the nebula. Conditions are broadly divided into four areas; standard, X-ray, dense-cloud and dense-cloud with X-ray models. Standard model conditions have standard ζ (cosmic-ray ionisation rate) values (5×10^{-17} s^{-1}) and standard

[2]http://www.udfa.net/

[3]http://www.physics.ohio-state.edu/ eric/research.html

R_V (the total to selective extinction ratio) value (3.1). X-ray models have increased ζ (5×10^{-16} s^{-1}), to simulate X-ray emission (see §5.3.2), otherwise values are the same as standard models. These models are labelled as ModA and ModA2, respectively. Models ModB and ModB2 represent dense-cloud environments and dense-cloud with a simulated X-ray emission, respectively. Dense-cloud models have standard ζ values and an increased R_V value. The diffuse ISM has a typical R_V of 3.1 and is the default value in the Meudon code (and hence for ModA and ModA2 models). The value of R_V, in general rises from 3.1 to 4 and 5 for star formation regions and dark clouds (Moore et al. 2005). A larger value of R_V is suggested to indicate larger grains in a dense environment (Cardelli and Clayton 1991). As the massive expanding torus of NGC 6302 is suggested to have a total torus mass of $\sim 2\ M_\odot \pm 1\ M_\odot$ (Peretto et al. 2007), and as the presence of a population of large and cold grains has been suggested by Molster et al. (2001), ModB models have an increased $R_V = 5.5$ to reflect a dense-cloud environment populated with large grains. Dense-cloud with X-ray models have a R_V of 5.5 and increased ζ the same as X-ray models.

Within these model sets, a number of different chemistry files have been constructed with varying N/O abundances as NGC 6302 is an O-rich PN with a high nitrogen abundance (Wright et al. 2011). In addition, enhanced H_2O reactions have also been included to establish if increased reaction rates can affect the production of HCO^+ (§5.3.5). The C/N/O abundances (relative to H) specific to NGC 6302 have been discussed by Casassus et al. (2000) (referenced from Barlow (1983)) and Wright et al. (2011). General Type 1 PNe abundances are also discussed by Kingsburgh and Barlow (1994). Values discussed in Casassus et al. (2000) are C/H = 4.4 x 10^{-4}, O/H = 5.0 x 10^{-4} and N/H = 9.2 x 10^{-4}, whilst those of Wright et al. (2011) are C/H = 2.2 x 10^{-4}, O/H = 5.1 ± 1.3 x 10^{-4} and N/H = 3.9 x 10^{-4}. Those of Kingsburgh and Barlow (1994) are C/H = 4.28 ± 5.35 x 10^{-4}, O/H = 4.93 ± 2.22 x 10^{-4} and N/H = 5.2 ± 0.88 x 10^{-4}. Values used in the models are given in Table 5.4 and the chemistry files are identified by a K number. The chemistry is therefore presented from the perspective of an O-rich

nebula.

The modelled column density figures at $A_V = 7-8$ are presented in Table 5.5, whilst the observed column densities from this work used for direct comparison, are available in Table 4.4. This table also includes comparisons with other modelled PN environments obtained from the literature. While ^{13}CS is presented in the observations for this work (Chapter 3), isotopic species are not present in the Meudon chemistry files and thus are not included in the models. Its isotopologue, CS, is instead used in the following analysis and comparison for this thesis and hence represents an upper limit for this species. Also, species such as SiO and $^{29}SiC_2$ are also not present in the chemistry network and hence are not included in the models.

Table 5.4: Details of the chemistry file parameters for all models.

Chem File	C/H	N/H	O/H	HCO^+/N_2H^+ reaction rates	Notes
K0	3.6 (-04)	3.9 (-04)	5.01 (-04)	standard UMIST	(C, O) average of values in refs 1, 2 and 3. (N) from ref 2
K1	3.6 (-04)	9.2 (-04)	5.01 (-04)	standard UMIST	(C, O) average of values in refs 1, 2 and 3. (N) from ref 1
K2	3.6 (-04)	3.9 (-04)	7.15 (-04)	standard UMIST	(C) average values of refs 1, 2 and 3. (N) from ref 2. (O) upper limits from ref 3
K3	3.6 (-04)	9.2 (-04)	7.15 (-04)	standard UMIST	(C) average values of refs 1, 2 and 3. (N) from ref 1. (O) upper limits from ref 3
K4All	3.6 (-04)	3.9 (-04)	7.15 (-04)	enhanced H_2O reactions	(C, N, O) values as above but with increased reaction rates for H_2O
K5All	3.6 (-04)	9.2 (-04)	5.01 (-04)	enhanced H_2O reactions	(C, N, O) values as per K1 but with increased reaction rates for H_2O

All rates/abundances in the form; a(b) = a x 10^b

References: (1) Casassus et al. (2000), (2) Wright et al. (2011), (3) Kingsburgh and Barlow (1994) (Type 1 PN)
(4) Huntress and Anicich (1976), (5) Huntress et al. (1980)

5.3.1 Standard Models (ModA)

In the standard models, the column density figure of CN is over an order of magnitude greater than HCN, and over two orders of magnitude greater in nitrogen enriched models compared with O-rich chemistry. This could be attributed to HCN having a larger effective photo-dissociation rate than CN by a factor of ~ 2-3. Nonetheless, in the observed column densities, CN and HCN are of the same order of magnitude. The higher dissociation energy of CN requires photons of shorter wavelengths, and such photons are absorbed by dust more efficiently. CN is primarily formed via CH + N → H + CN across all the chemistry files and then via C + NH followed by C + NO for the K0 and K1 chemistry files and vice-versa for K2 and K3 chemistry files. Photodissociation by HCN accounts for just ~5% of the production total over all chemistry files. Similarly the formation route for HCN differs little between O-rich and N-rich chemistry, and is formed via CH_2 + N → H + HCN (~55%), followed by $HCNH^+ + e^-$ → H + HCN. Production via H_2 + CN → H + HCN accounts for ~4-8%. The destruction of CN is via collisions with N and O across K0 to K3 chemistry files, whilst HCN on the other hand, is destroyed predominately by photons in all models.

Interestingly, the main formation path of HNC across all models, is the same as that of HCN, namely CH_2 + N → H + HCN. The [HNC/HCN] abundance ratio across the range of astronomical environments ranges from ~1/100 and the formation route (within molecular clouds) is thought to be $HCNH^+ + e^-$ → H + HNC (Sarrasin et al. 2010). This dissociative recombination however, is a secondary route in these models, accounting for just ~10-15% of HNC formation. HNC is destroyed in the same manner as HCN, through interactions with photons or through ion-molecule reactions with C^+.

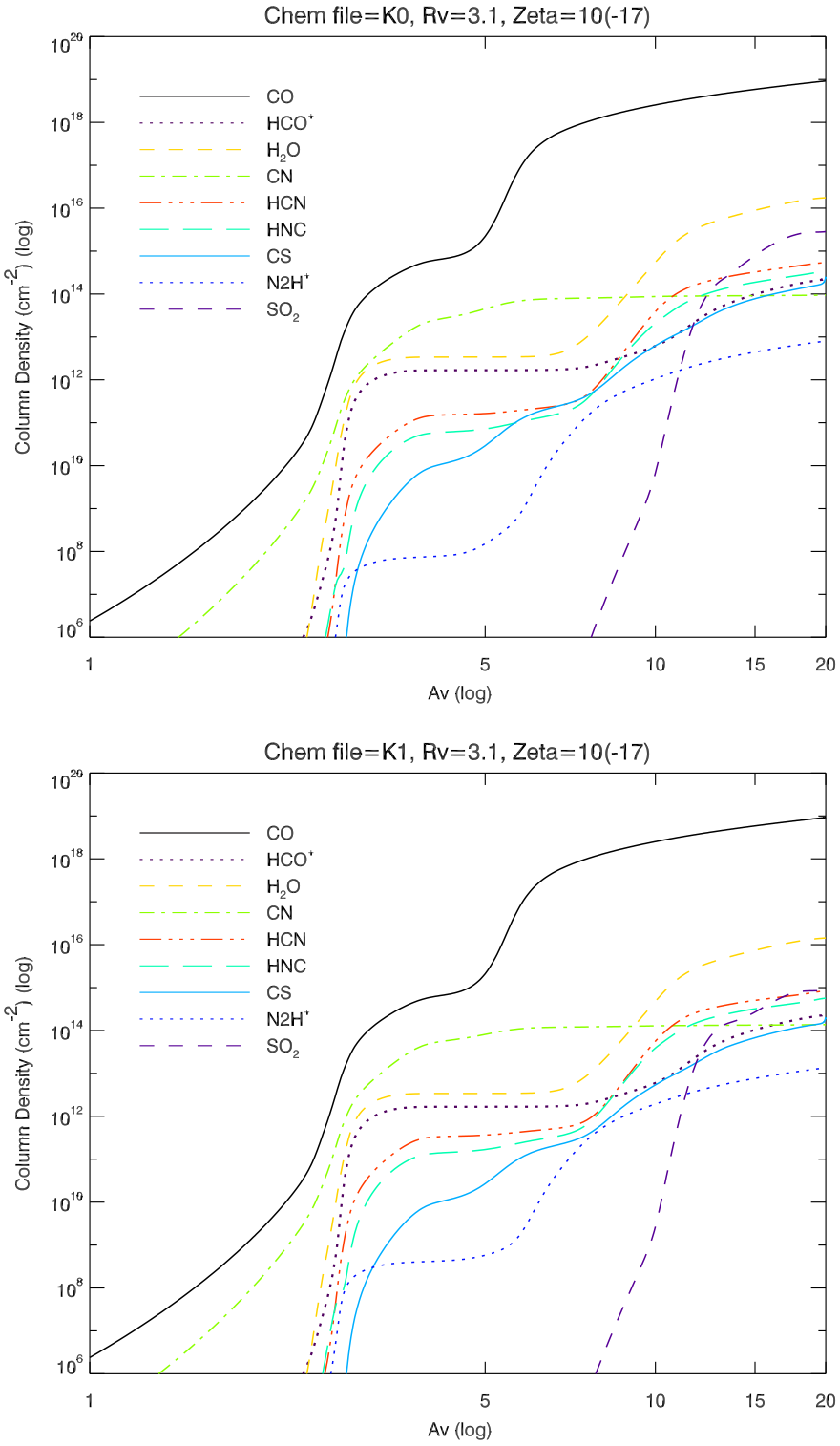

Figure 5.2: Standard models (ModA). Chemistry file K0 (upper) and K1 (lower).

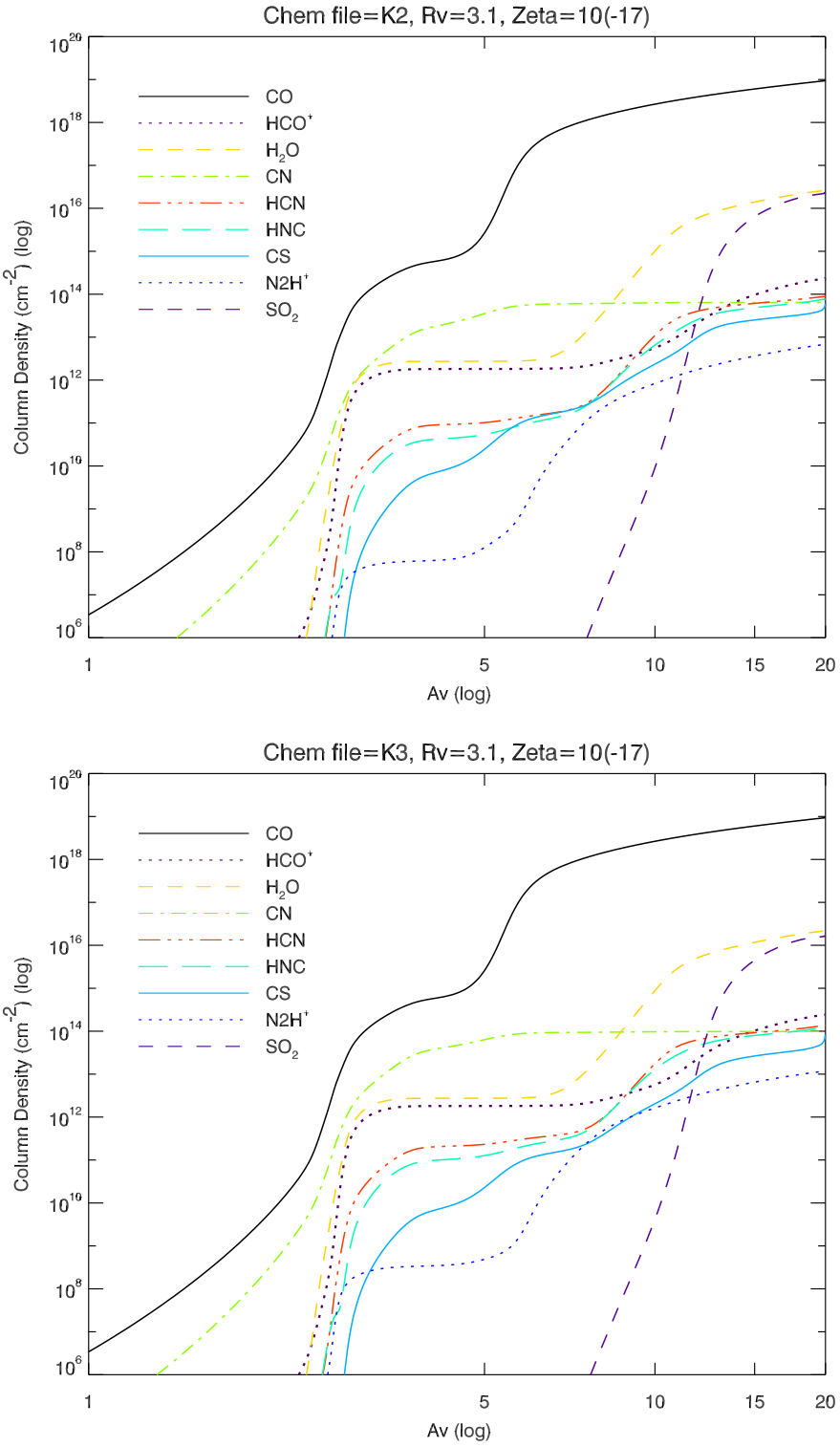

Figure 5.3: Standard models (ModA). Chemistry file K2 (upper) and K3 (lower).

Table 5.5: Column Densities for all Models at A_V = 7 / 8

Model Name/ Species	ModA K0 2031	ModA K1 2031	ModA K2 2031	ModA K3 2031	ModA K4All 2031	ModA K5All 2031
CO	7.08(17)/1.29(18)	6.91(17)/1.27(18)	7.90(17)/1.39(18)	7.79(17)/1.38(18)	7.10(17)/1.30(18)	7.82(17)/1.38(18)
HCO^+	1.77(12)/2.41(12)	1.76(12)/2.34(12)	1.92(12)/2.47(12)	1.91(12)/2.44(12)	1.80(12)/2.44(12)	1.93(12)/2.48(12)
H_2O	5.02(12)/2.08(13)	4.80(12)/1.78(13)	5.41(12)/3.16(13)	5.06(12)/2.67(13)	4.66(12)/1.91(13)	4.66(12)/2.48(13)
CN	7.90(13)/8.17(13)	1.20(14)/1.22(14)	5.97(13)/6.09(13)	9.35(13)/9.47(13)	7.90(13)/8.16(13)	9.34(13)/9.46(13)
HCN	2.76(11)/9.43(11)	5.72(11)/1.52(12)	1.97(11)/4.95(11)	4.10(11)/8.65(11)	2.76(11)/9.42(11)	4.08(11)/8.59(11)
HNC	1.90(11)/8.21(11)	3.92(11)/1.36(12)	1.58(11)/4.71(11)	3.24(11)/8.19(11)	1.90(11)/8.21(11)	3.22(11)/8.13(11)
CS	2.81(11)/7.12(11)	2.48(11)/6.29(11)	1.93(11)/4.00(11)	1.72(11)/3.57(11)	2.80(11)/7.05(11)	1.71(11)/3.52(11)
N_2H^+	4.59(10)/2.64(11)	9.48(10)/5.15(11)	3.81(10)/2.07(11)	8.63(10)/4.40(11)	4.61(10)/2.65(11)	8.69(10)/4.42(11)
SO_2	2.39(04)/4.19(06)	1.52(04)/2.08(06)	5.25(04)/6.41(06)	3.66(04)/3.76(06)	2.31(04)/4.11(06)	3.57(04)/3.17(06)
	ModA2 K0 2031	ModA2 K1 2031	ModA2 K2 2031	ModA2 K3 2031	ModA2 K4All 2031	ModA2 K5All 2031
CO	6.11(17)/1.17(18)	6.04(17)/1.15(18)	7.02(17)/1.29(18)	7.0(17)/1.28(18)	6.18(17)/1.18(18)	7.09(17)/1.29(18)
HCO^+	2.22(12)/5.82(12)	2.15(12)/5.36(12)	2.42(12)/5.99(12)	2.37(12)/5.72(12)	2.28(12)/6.10(12)	2.44(12)/6.07(12)

Continued on next page...

Table 5.5: Column Densities for all Models at A_V = 7 / 8

H_2O	1.75(13)/1.24(14)	1.60(13)/1.08(14)	2.54(13)/2.10(14)	2.31(13)/1.84(14)	1.41(13)/9.57(13)	1.89(13)/1.50(14)
CN	9.34(13)/1.15(14)	1.33(14)/1.53(14)	6.85(13)/7.86(13)	1.02(14)/1.12(14)	9.31(13)/1.14(14)	1.02(14)/1.11(14)
HCN	5.94(11)/4.91(12)	1.13(12)/8.07(12)	4.37(11)/2.69(12)	8.48(11)/4.79(12)	5.93(11)/5.00(12)	8.39(11)/4.81(12)
HNC	5.39(11)/4.72(12)	1.02(12)/8.24(12)	4.26(11)/2.77(12)	8.16(11)/5.09(12)	5.37(11)/4.81(12)	8.07(11)/5.13(12)
CS	5.50(11)/3.61(12)	4.50(11)/3.07(12)	3.54(11)/1.82(12)	2.97(11)/1.51(12)	5.41(11)/3.55(12)	2.89(11)/1.54(12)
N_2H^+	2.58(11)/1.65(12)	5.79(11)/3.35(12)	2.08(11)/1.31(12)	5.24(11)/2.94(12)	2.63(11)/1.68(12)	5.37(11)/3.03(12)
SO_2	7.08(05)/1.58(08)	3.47(05)/6.27(07)	1.28(06)/2.50(08)	6.70(05)/1.40(08)	6.79(05)/1.54(08)	6.49(05)/1.13(08)

	ModB K0 2055	ModB K1 2055	ModB K2 2055	ModB K3 2055	ModB K4All 2055	ModB K5All 2055
CO	8.91(13)/3.86(14)	8.90(13)/3.86(14)	1.21(14)/4.52(14)	1.20(14)/4.55(14)	8.98(13)/3.90(14)	1.21(14)/4.58(14)
HCO^+	1.87(12)/4.60(12)	1.87(12)/4.60(12)	2.51(12)/5.57(12)	2.51(12)/5.56(12)	1.91(12)/4.70(12)	2.56(12)/5.67(12)
H_2O	4.50(12)/1.15(13)	4.50(12)/1.15(13)	5.69(12)/1.23(13)	5.69(12)/1.23(13)	4.43(12)/1.12(13)	5.59(12)/1.20(13)
CN	6.86(11)/2.64(12)	9.95(11)/3.43(12)	6.32(11)/2.38(12)	9.32(11)/3.12(12)	6.87(11)/2.64(12)	9.32(11)/3.12(12)
HCN	1.95(12)/5.36(12)	2.71(12)/7.04(12)	1.79(12)/4.62(12)	2.54(12)/6.17(12)	1.95(12)/5.37(12)	2.54(12)/6.17(12)
HNC	1.20(12)/3.42(12)	1.69(12)/4.50(12)	1.09(12)/3.03(12)	1.56(12)/4.04(12)	1.20(12)/3.42(12)	1.56(12)/4.04(12)
CS	1.57(12)/2.41(13)	1.56(12)/2.40(13)	1.21(12)/1.51(13)	1.12(12)/1.51(13)	1.57(12)/2.41(13)	1.12(12)/1.52(13)
N_2H^+	2.52(10)/2.97(10)	8.51(10)/9.61(10)	3.15(10)/3.61(10)	1.04(11)/1.16(11)	2.52(10)/2.97(10)	1.04(11)/1.16(11)

Continued on next page...

Table 5.5: Column Densities for all Models at A_V = 7 / 8

SO_2	9.41(03)/3.51(04)	9.43(03)/3.58(04)	1.68(04)/5.12(04)	1.68(04)/5.13(04)	9.40(03)/3.57(04)	1.68(04)/5.13(04)
	ModB2 K0 2055	ModB2 K1 2055	ModB2 K2 2055	ModB2 K3 2055	ModB2 K4All 2055	ModB2 K5All 2055
CO	8.85(13)/3.83(14)	8.85(13)/3.84(14)	1.20(14)/4.50(14)	1.20(14)/4.50(14)	8.92(13)/3.87(14)	1.21(14)/4.54(14)
HCO^+	1.85(12)/4.57(12)	1.85(12)/4.56(12)	2.49(12)/5.51(12)	2.49(12)/5.51(12)	1.89(12)/4.66(12)	2.54(12)/5.61(12)
H_2O	4.48(12)/1.14(13)	4.48(12)/1.14(13)	5.64(12)/1.21(13)	5.64(12)/1.22(13)	4.04(12)/1.11(13)	5.54(12)/1.18(13)
CN	1.41(12)/6.61(12)	1.66(12)/7.79(12)	1.24(12)/5.83(12)	1.48(12)/6.97(12)	1.41(12)/6.61(12)	1.48(12)/6.97(12)
HCN	4.25(12)/6.61(12)	4.82(12)/1.51(13)	3.72(12)/1.10(13)	4.28(12)/1.28(13)	4.25(12)/1.32(13)	4.28(12)/1.28(13)
HNC	2.58(12)/8.40(12)	2.94(12)/9.72(12)	2.24(12)/7.25(12)	2.59(12)/8.50(12)	2.58(12)/8.40(12)	2.59(12)/8.50(12)
CS	1.54(12)/2.35(13)	1.53(12)/2.34(13)	1.11(12)/1.49(13)	1.11(12)/1.49(13)	1.54(12)/2.35(13)	1.11(12)/1.49(13)
N_2H^+	9.73(09)/1.76(10)	6.47(10)/8.08(10)	1.32(10)/2.09(10)	8.18(10)/9.77(10)	9.73(09)/1.75(10)	8.17(10)/9.77(10)
SO_2	9.36(03)/3.54(04)	9.37(03)/3.54(04)	1.66(04)/5.03(04)	1.66(04)/5.04(04)	9.35(03)/3.53(04)	1.66(04)/5.04(04)

All rates/abundances in the form; a(b) = $a \times 10^b$

In the confines of the CO molecular zone, CO is predominantly formed via $HCO^+ + e^- \rightarrow H + CO$ regardless of any O or N enhancement. At $A_V = 7$, the same reaction dominates. In all models, the primary destruction route for CO is combination with H_3^+ to form $H_2 + HCO^+$. Preferential modes for destruction also include combination with N_2H^+ and secondary photon interaction, with destruction by N_2H^+ favoured more in N-rich chemistry. The reaction paths of CO and HCO^+ are closely linked, with the main destruction routes of CO being the favoured formation route for HCO^+ in ModA and ModA2 models. The reaction $CO^+ + H_2$ is favoured by Kimura et al. (2012) for the production of HCO^+ in the H^0 and H_2 zones, where strong UV radiation prevails (see *S* 5.3.6). The chemical abundances of carbon and oxygen used in the models by Kimura et al. (2012) however are equal. In an oxygen or nitrogen rich environment, HCO^+ formation proceeds via $O + CH_2^+$ and $O + CH_2^+$ in the same zone. At $A_V = 7$, the reaction,

$$CO + H_3^+ \rightarrow H_2 + HCO^+ \tag{5.13}$$

dominates. H_3^+ is expected to be very short-lived due to its rapid recombination with electrons, thus reaction 5.13 requires a high survival rate of H_3^+. The production of H_3^+ can be increased by ionisation of H_2 by an impinging soft X-ray flux or cosmic rays and is discussed in the next section (5.3.2). In a similar manner, the production and destruction of HCO^+ and the dense gas dust tracer N_2H^+ are also interwoven. Whilst reaction 5.13 is the primary formation route for HCO^+, it is also produced by the minor reaction $CO + N_2H^+ \rightarrow N_2 + HCO^+$, which is a secondary destruction path of N_2H^+. The primary formation route for N_2H^+ is

$$N_2 + H_3^+ \rightarrow H_2 + N_2H^+ \tag{5.14}$$

which accounts for ~85% of the N_2H^+ formation across all ModA (standard models) at $A_V = 7–8$. Unlike HCO^+ however, N_2H^+ has but one alternative formation route, the ion-neutral reaction

$$H_2 + N_2^+ \rightarrow H + N_2H^+. \quad (5.15)$$

This alternative reaction is the controlling formation path for N_2H^+ at $A_V = 3{-}4$, with minor contributions from $N + NH_2^+ \rightarrow H + N_2H^+$.

The primary formation route for CS across all models is via the dissociative recombination of $HCS^+ + e^- \rightarrow H + CS$ with $CH + S \rightarrow H + CS$ the secondary favoured route. In an O-rich environment with low nitrogen abundances (K2 chemistry files), the reaction,

$$C + SO \rightarrow O + CS \quad (5.16)$$

accounts for ~15% of reactions and is preferred over $CH_2 + S \rightarrow H_2 + CS$ and $C_2S^+ + e^- \rightarrow C + CS$ in N-enhanced (K3) chemistry. It can be seen in the models (Figures 5.2 and 5.3) that at $A_V = 5$, CS abundances are the same across all models, however at the second development phase ($A_V = 7{-}8$), CS does not rise as steeply lowering the overall column density. As noted above, SO_2 rises steeply in abundance from $A_V = 6$, and begins to plateau around $A_V = 15$. Between $A_V = 7$ and $A_V = 8$ a difference of two magnitudes is seen. N-rich chemistry appears to hinder the production of SO_2 as column densities are a factor of four higher in chemistry files with lower nitrogen abundances (K0 and K2). Similarities are seen above for CS formation with SO, in reaction 5.16, where this reaction is 10% less productive in nitrogen enriched chemistry. The dominant formation path for SO_2 is the same across all models and is limited to two reactions,

$$OH + SO \rightarrow H + SO_2 \quad \text{and} \quad (5.17)$$

$$O + SO \rightarrow SO_2 + \text{photon} \quad (5.18)$$

The neutral reaction of OH + SO accounts for ~55-65% of the formation process, whilst O + SO ~35-45%, through chemistry files K0 – K2. For K3 chemistry however,

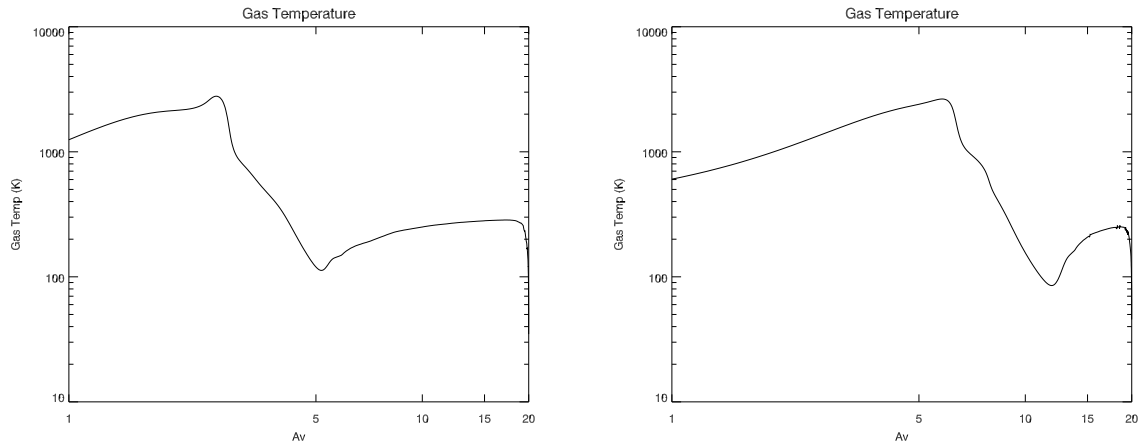

(a) Thermal profile of standard models

(b) Thermal profile of dense-cloud models

Figure 5.4: (a) Gas temperature with A_V in standard models (ModA). (b) Gas temperature with A_V in dense-cloud models (ModB)

the reverse is true, with reaction preferred above reaction . Regardless of enrichment, SO_2 is preferentially destroyed by photon interaction across all models.

5.3.2 X-ray Models (ModA2)

To explain the abundances of some species within PN, X-rays have been introduced into chemical models to ascertain their effect on the chemistry. This has been undertaken by Ali et al. (2001) and Kimura et al. (2012) for example, who suggest that modelled abundances can realistically approximate observational results *only* with the inclusion on an X-ray flux. An X-ray flux has been simulated by Ali et al. (2001) via enhancement to the cosmic ray ionisation rate within their models. This simplified approach was adopted because although X-ray ionisation can produce multiply charged ions such as C^{++}, ions produced in this manner undergo rapid charge exchange. The resulting species, such as H_2^+ and H_3^+ produced quickly by charge-transfer reactions are also the dominant ions produced by cosmic rays. Enhancement to the cosmic ray ionisation rate can be implemented effectively in the Meudon code and therefore the method by Ali et al. (2001) was adopted in this work to simulate an X-ray flux.

In models (ModA2) with enhanced X-ray emission (Figures 5.5 and 5.6), changes to column densities can be loosely grouped into two categories; species whose column densities increase by a factor of 1−2 and species which increase by a factor of $\gtrsim 4$. CN belongs to the former group, along with HCO^+ at $A_V = 7$. At $A_V = 8$ however, the differences with standard models is a factor of three higher. HNC, CS, N_2H^+ and H_2O all belong in the latter group, along with SO_2 having the biggest increase. For this molecule a difference of one order of magnitude at $A_V = 7$ and two orders of magnitude at $A_V = 8$ is seen, compared to the non X-ray enhanced counterparts. The one exception to the two groups is CO, which has slightly lower abundances across all chemistry files within the X-ray models.

In the standard models, the formation process for CN is largely unvarying across all chemistry files and this remains the case with the addition of an X-ray flux. Photodissociation of HCN to form CN remains a minor process, accounting for ~4% of reactions with CN preferentially destroyed by separate reactions with N and O. It would appear, therefore, that CN is relatively unaffected by X-ray emission in this modelled environment. Similarly, the primary and secondary formation paths for HCN and HNC remain unaltered with X-ray interaction. The favoured reaction of CH_2 + N accounts for ~55-63% of reactions for the formation of HCN and HNC respectively, whilst the dissociative recombination reaction of $HCNH^+ + e^-$ produces ~30-35%. This is contrary to the models of Kimura et al. (2012) and Ali et al. (2001), where $HCNH^+ + e^-$ is the main formation route for both HCN and HNC. Furthermore, the destruction routes in ModA2 models, of both species remain comparable with standard models (ModA), with photodissociation and collisions by C^+ the favoured methods.

The remaining species, H_2O, CS, N_2H^+ and SO_2 all have increased column density figures compared with standard models and are enhanced by a factor of five or more across all chemistry files (K0 to K3). Reaction pathways for all species do not deviate from standard conditions and neither do destructions routes. Interestingly, the column density for N_2H^+ with inclusion of psuedo X-ray emission is very closely matched to its observed column density, except for chemistry models K1 and K3, which are a factor of two higher. Detections of N_2H^+ are limited within PNe, with detections generally being constrained to younger objects. Cox et al. (1992) did not detect N_2H^+ in two evolved PNe, and accordingly used the negative result as a constraint to identify the evolution of PNe. High column densities of N_2H^+ were recorded by Zhang et al. (2008) in NGC 7027, a PN of similar evolutionary status to NGC 6302, with column densities $7-8$ orders of magnitude higher than predicted by their models. Although the models of Zhang et al. (2008) did not include the addition of an X-ray flux, the authors suggest a high formation rate of H_3^+ via either cosmic-ray or soft X-ray emission from the central star to account for the high formation rate of N_2H^+. As NGC 7027 is reported to emit strong X-ray emission it was thus deduced that more evolved PN with weaker X-ray emission would have little or no N_2H^+.

In the X-ray models (Figures 5.5 and 5.6), SO_2 is produced at lower extinctions which accounts for the large increase in column densities, otherwise formation and destruction paths remain unchanged in regards to standard models (Sternberg and Dalgarno 1995). X-ray photons have a significantly lower photoabsorption cross-section than UV photons and can hence penetrate greater distances within the nebula. Soft X-rays with an energy roughly in the range of 0.1 - 2 keV would be sufficient to fragment CO, if allowed to traverse the nebula unimpeded. In a mainly neutral gas, ionisation of H atoms by X-rays can produce secondary ionisation and excitations, thus inducing further reactions. X-ray (and cosmic ray) ionisation of H_2 produces H_2^+, which reacts rapidly to form,

$$H_2^+ + H_2 \rightarrow H_3^+ + H \text{ and } H_3^+ + e^- \rightarrow 3H \text{ or } H_2 + H \quad (5.19)$$

In low temperature environments, oxygen atoms do not react with hydrogen molecules, however, in the presence of the ions above, despite low temperatures, oxygen will react with H_3^+ to form $O + H_3^+ \rightarrow OH^+ + H_2$. OH^+ and H_2 can then produce,

$$OH^+ \xrightarrow{H_2} OH_2^+ \xrightarrow{H_2} OH_3^+ \quad (5.20)$$

OH_3^+ is then further modified through dissociative recombination with electrons to form $OH + H_2$ and $H_2O + H$ (Sternberg and Dalgarno 1995). HCO^+ and CO are both products of further ion-molecule reactions with H_2O and OH and the reactions are discussed §5.3.5.

To summarise, the modelled column density of CS and N_2H^+ compare most closely with observed column densities, when X-rays are introduced, otherwise, the inclusion of X-rays generally serves to increase column densities of most modelled species compared with standard models. The exceptions to this are CO, CN and HCO^+. X-ray emission does not significantly alter the formation or destruction pathways for these modelled species and no other overwhelming trend resulting from the inclusion of X-rays can be identified from these models.

5.3.3 Dense-Cloud Models (ModB)

In the wavelength range $3.5\ \mu\text{m} \geq \lambda \geq 0.125\ \mu\text{m}$, the optical/UV extinction curve can be approximated by an analytical formula derived by Cardelli et al. (1989), which depends on only one parameter, R_V the total-to-selective extinction coefficient ($R\ [= A(V)/E(B-V)]$. Dust grains along different lines of sight are composed of different size distributions and possibly, varying compositions. The value of R_V depends on the environment, with a smaller R_V found in lower-density regions, with the extinction having a steep far-UV rise and is associated with populations of small dust grains.

Larger R_V values on the other hand, are found in dense regions, with the extinction having a flatter far-UV rise due to larger grains. The standard models are constructed with a standard R_V of 3.1, however NGC 6302 has a high mass-loss rate, $\sim 1.5 \times 10^{-4}\ M_{\odot}$, resulting in a dense (average gas density of $\sim 2 \times 10^4$ cm^{-3}) and massive torus (Dinh-V-Trung et al. 2008) and is also suggested to contain a population of large grains (Molster et al. 2001). It is possible therefore that the standard R_V value of 3.1 does not reflect conditions in the torus of NGC 6302. A number of R_V values are available for selection within the Meudon code and a value of 5.5 was chosen to emulate a dense-cloud environment populated with large grains. This is the same value as the Orion Nebula, a PDR known for its anomalous dust emission (Le Petit et al. 2006).

The increased R_V value changes one significant aspect of the models, the temperature profile of the cloud, which in turn has a widespread affect on the chemistry. As can be seen in Figure 5.4, a larger R_V corresponds to lower extinction, consequently UV radiation penetrates deeper into the cloud. This results in higher temperatures at larger A_V in dense-cloud models compared to standard models. For example at $A_V = 7$ in dense-cloud models, the temperature is $\sim 740 - 770$ K compared with $\sim 150 - 170$ K for standard models. This change has a cascading effect on the molecular structure of the cloud, where a steep increase in column densities at $A_V \sim 3$ in standard models (see Figure 5.2 for example), marks the boundary of the molecular formation zone. This zone is now apparent at $A_V \sim 5.5$ for dense-cloud models, where column densities increase rapidly depending on the species, within a short A_V range. The second phase enhancement seen in standard models at $A_V \sim 7$, now occurs around $A_V = 12$ for some species (CO and CS), where a modest incline is seen. The remaining species, with the exception of CN and SO_2, plateau out and start to rise again around $A_V = 15$. The abundances of CN remains approximately constant and does not rise as per the standard models. The abundances of SO_2 on the other hand is markedly different. The production of SO_2 does not occur until around $A_V \sim 12$ in O-rich chemistry model. In the nitrogen enriched chemistry, and chemistry files with a lower initial oxygen abun-

dance, however, formation occurs around $A_V = 6$. In these models (K0 and K1) SO_2 rises sharply over a few orders of magnitude, remains level, then rises sharply again at $A_V = 14$.

The effects of an increased temperature at $A_V = 7$ also extends to reaction pathways. Carbon, which would be preferentially locked up in CO, is now available for reactions, which were not viable at the corresponding A_V in standard models. CS for example, was primarily formed via $HCS^+ + e^-$ in the standard models. In the dense-cloud models however, the dominant route is through $C_2S^+ + e^-$ whereby the former reaction now only accounts for ∼16−18%. The destruction paths similarly differ; in the standard models CS was destroyed via photon interaction, however in the dense-cloud models it is destroyed through the addition of atomic oxygen. Removal through photon interaction is now limited to ∼16% instead of ∼95% as in the standard models. The column density for CS is also particularly modified by extinction. CS is noted to be a dense gas tracer (Simon et al. 1997), and in the limit of these models, CS is nearly an order of magnitude more abundant at $A_V = 7$ and over a factor of 15 greater at $A_V = 8$, compared with standard models.

The production of CS is akin to that of SO_2 in the standard models; it is not produced until $A_V = 5$, then rises sharply to surpass all other species except CO. At $A_V = 12$, the column density of CS and CO are comparable, however at this point CO continues to rise, whereas CS plateaus. The development of CO is the same as the standard models, except its formation is repressed until $\sim A_V \sim 6$ and hence the column densities are greatly reduced. Whilst the main formation route for CO remains unchanged, the secondary production route now changes from C + OH or O + CN to $H + CO^+$.

The column densities in general for all species are reduced by a few factors at $A_V = 7$, compared with standard models. At $A_V = 8$ however, most models see a moderate increase, except for N_2H^+, SO_2 and CN. CN is lower by nearly two orders of mag-

nitude at $A_V = 7$ compared with the standard models and is similarly underproduced at $A_V = 8$. The evolution of CN mirrors that of standard models, with no second enhancement phase. Production of CN, starts at an earlier A_V compared to other species and once the formation zone $A_V \sim 6$ is reached, a steady increase is observed. As with other species, the formation and destruction routes are also different. The formation route CH + N → H + CN is still preferred for oxygen-rich chemistry, however in low oxygen and/or high nitrogen chemistry files, the primary pathway is now via $CNC^+ + e^-$. CN was removed through addition of either O or N atoms in standard models, in dense-cloud models CN is now destroyed predominantly through photon interaction, with a minor percentage via the neutral-neutral reaction with H_2.

The column densities of HCN and HNC on the other hand, are increased overall at both $A_V = 7$ and 8, except for K2 chemistry files at $A_V = 8$. K2 is oxygen-rich and HCN column densities in this chemistry file remain the lowest throughout its evolution to $A_V = 20$. HCN is now formed via $HCNH^+ + e^-$ across all chemistry files, with H_2 + CN a secondary preferred route. The HNC primary formation pathway follows that of HCN, however, its secondary route favours the previous primary production pathway, that of CH_2 + N.

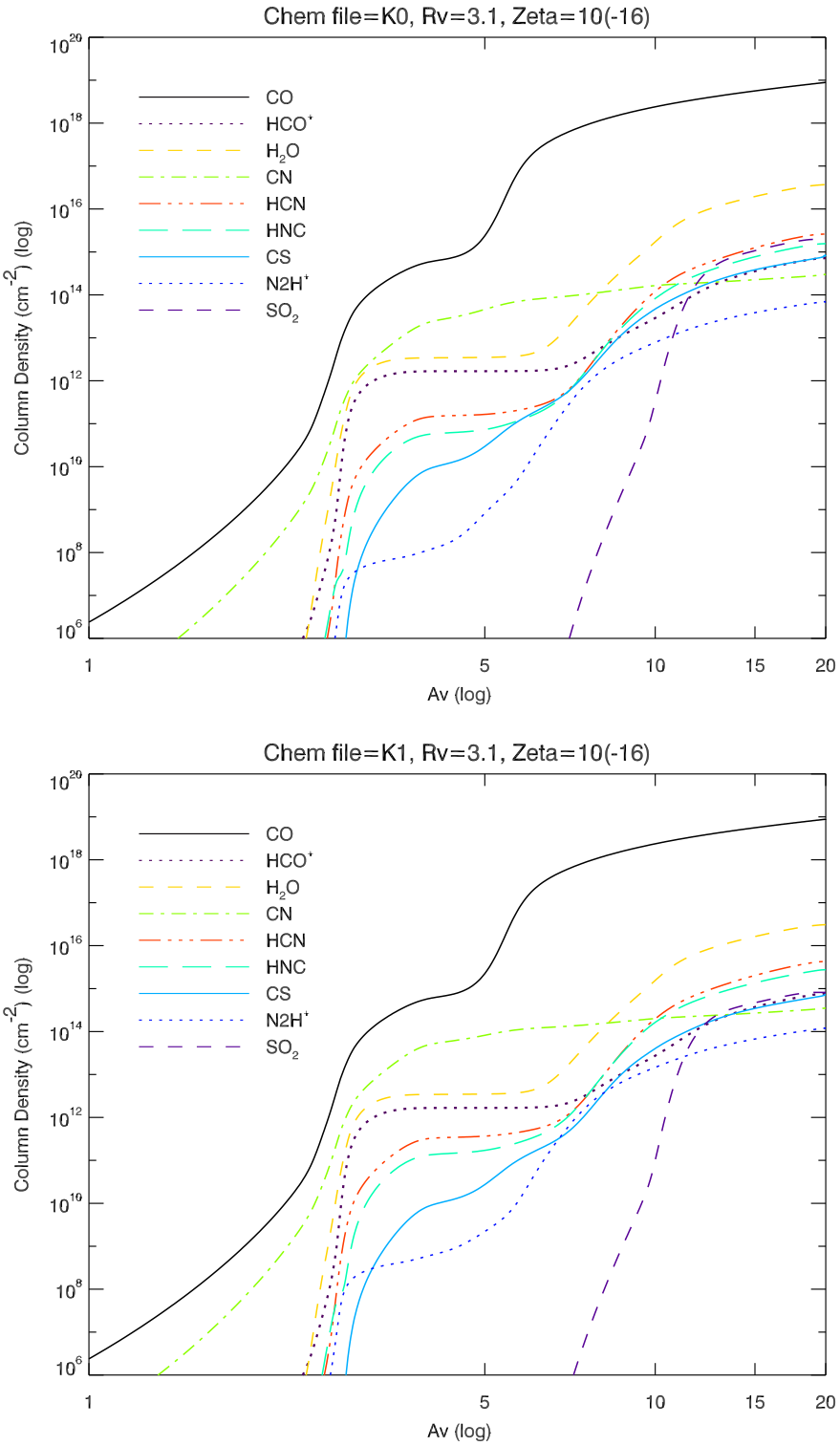

Figure 5.5: X-ray enhanced models, standard R_V (ModA2). Chemistry files K0 (upper) and K1 (lower).

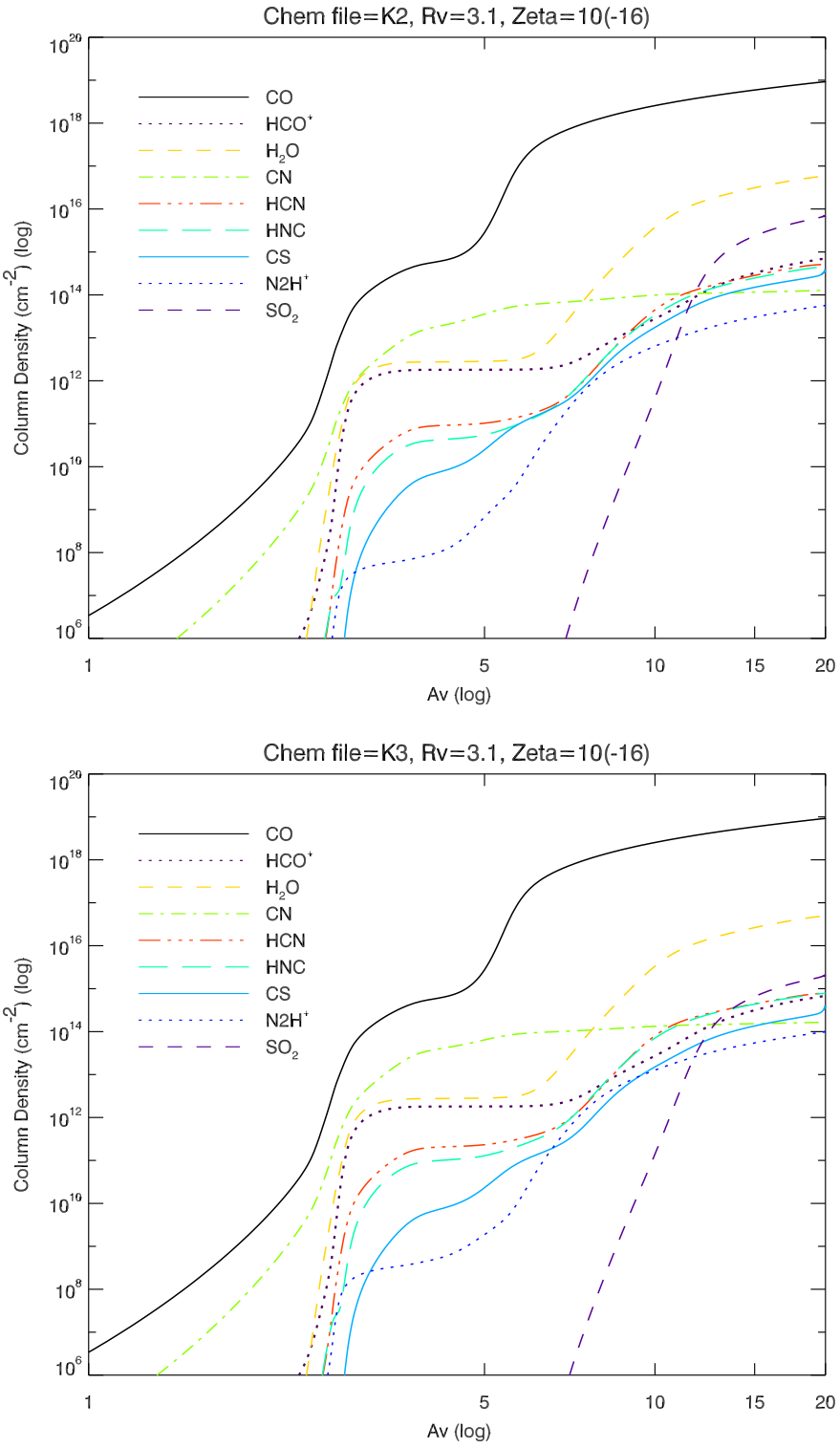

Figure 5.6: X-ray enhanced models, standard R_V (ModA2). Chemistry files K2 (upper) and K3 (lower).

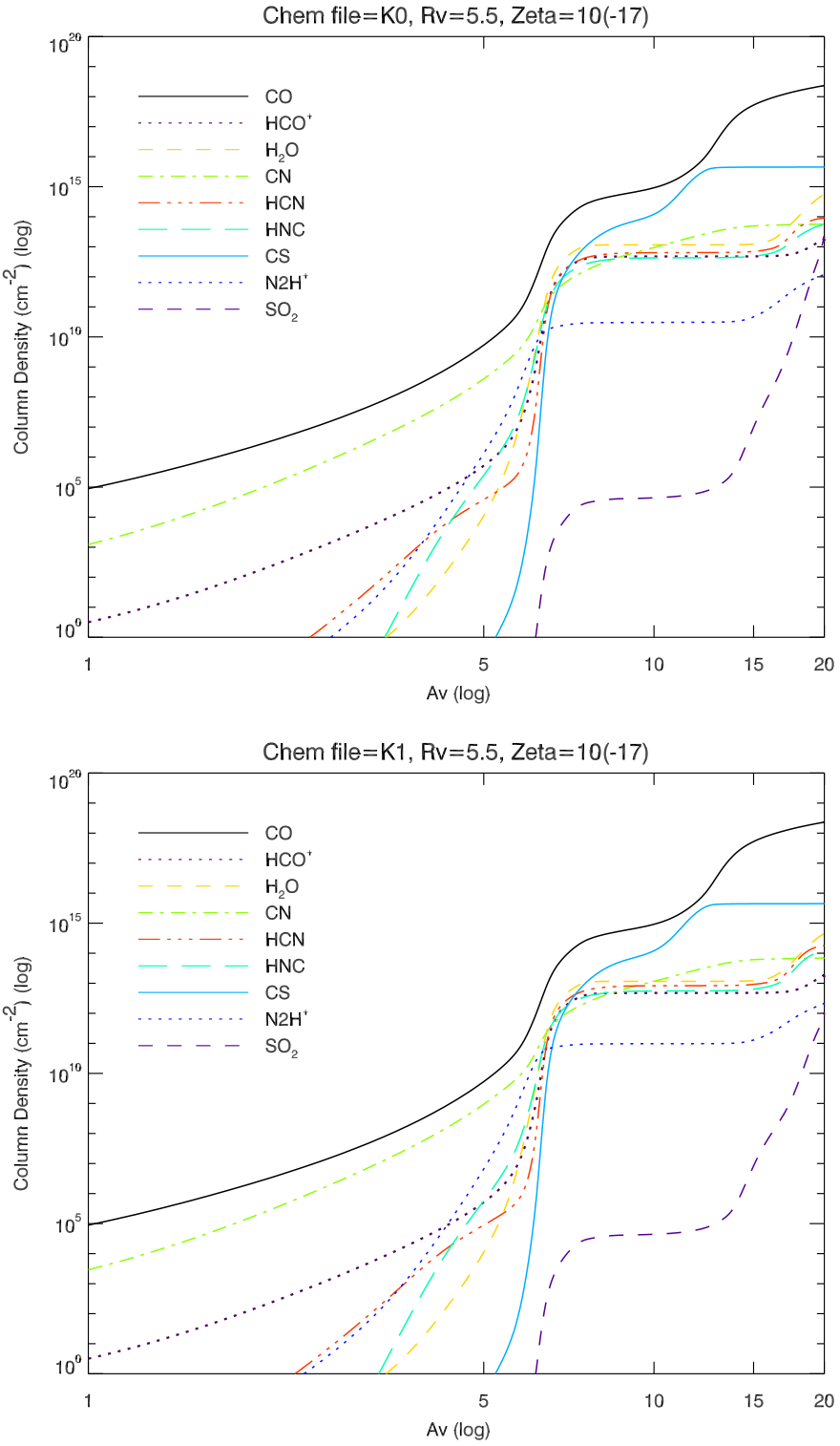

Figure 5.7: Dense-cloud models (ModB). Chemistry file K0 (upper) and K1 (lower).

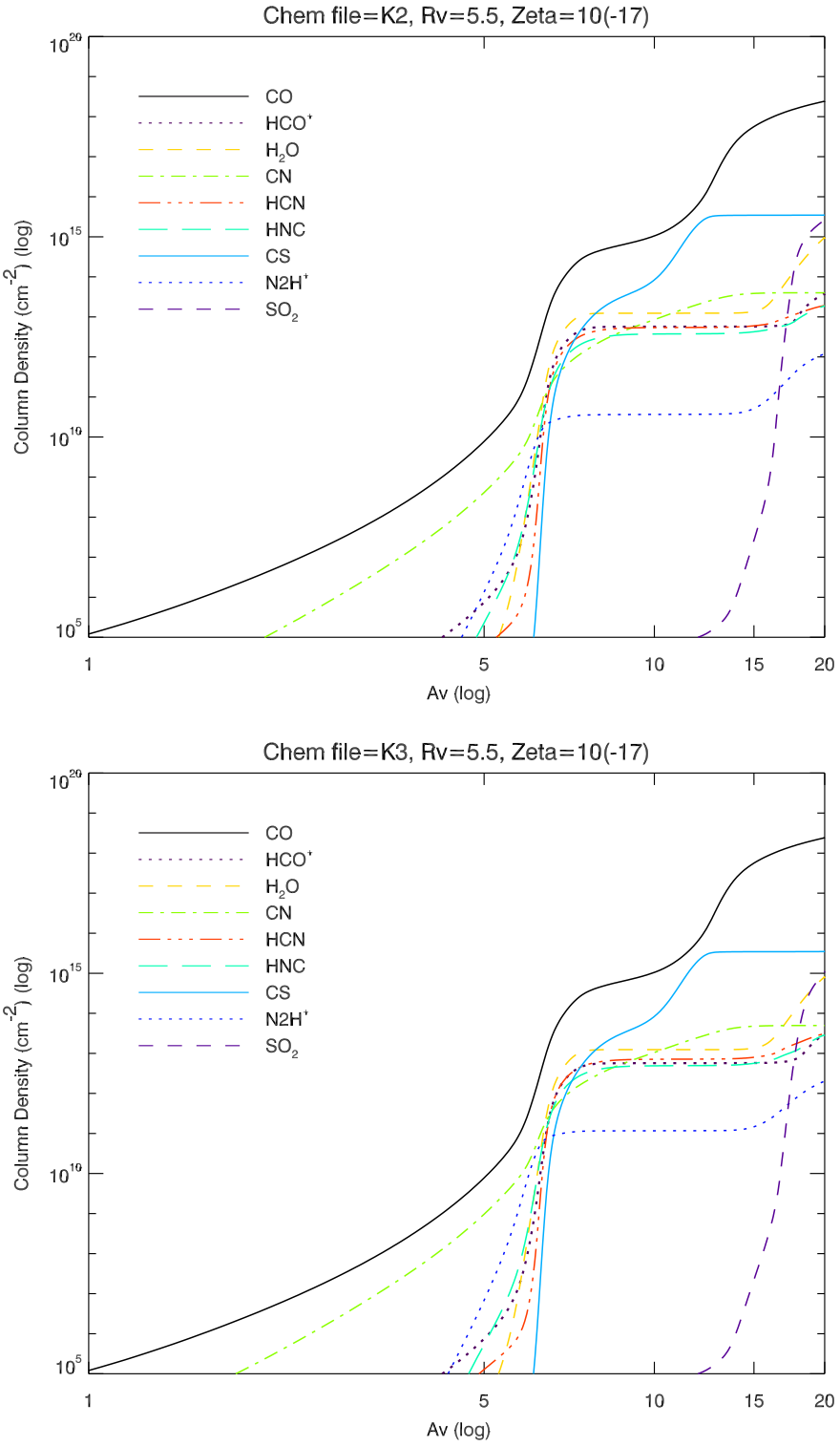

Figure 5.8: Dense-cloud models (ModB). Chemistry file K2 (upper) and K3 (lower).

The primary formation route for N_2H^+ in the standard models, does not even appear in dense-cloud models and the primary pathway is now via N_2 + HOC^+, followed by N_2 + OH^+. N_2H^+ is destroyed in the same manner through dissociative recombination but to a much larger degree when R_V is increased. Although N_2H^+ forms efficiently in dense-cloud models, column density figures remain lower than in the standard models.

The column densities of HCO^+ and H_2O are not significantly different from the equivalent standard models, however, like most other species, the formation and destruction routes are. As CO is dissociated at a larger A_V in the dense-cloud models compared with standard models, HCO^+ no longer forms via CO + H_3^+, but is predominantly produced by O + CH_2^+ and O + CH_3^+. Nonetheless, HCO^+ is still destroyed in the same manner as in the standard models. H_2O had only one formation route in the standard models, that of H_3O^+ + e^-. As this region in the dense-cloud models marks the zone where photons are able to dissociate the molecular hydrogen are mostly absorbed, H_2 is available for reactions. H_2O is now predominantly formed through the neutral-neutral reaction of H_2 + OH with the former reaction accounting for ~15% of production.

Overall, it would appear that dense-cloud conditions either negatively influences the column density of species (CN, N_2H^+, SO_2 and by quite a large margin, CO) or species flourish, namely CS, HCN and HNC. Others are indifferent, showing slight increases and decreases depending on the chemistry file used (HCO^+ and H_2O). Little distinction between formation and destruction pathways between the various chemistry files is seen, however, the pathways themselves are greatly affected compared with standard models. This is due to the temperature difference between the two models at the same A_V. The higher temperature allows H_2 to facilitate the hydrogenation or formation of some molecules, whilst CO is dissociated, thus permitting atomic O and C reactions to proceed at a much larger A_V.

5.3.4 Dense-Cloud with X-ray Models (ModB2)

The column density for the dense-cloud models with X-rays, exhibit minor differences compared with dense-cloud models alone. Indeed differences are negligible, with some species, CO, CS, HCO^+, H_2O and SO_2, showing less than 2% difference between models at both $A_V = 7$ and $A_V = 8$. CN, HCN and HNC on the other hand have increased column densities by a factor of 2 or 3. Contrary to these results N_2H^+ has a reduced column density by a factor of 2 in K0 chemistry files compared with K0 chemistry files in dense-cloud models. It is notable, that whilst X-ray emission in standard models increased N_2H^+ column densities, in a dense-cloud environment, X-rays have the opposing effect. Reaction routes also deviate from dense-cloud models for N_2H^+, whilst other species are unaffected. In dense-cloud models N_2H^+ is formed via,

$$N_2 + HOC^+ \rightarrow CO + N_2H^+ \quad \text{and} \tag{5.21}$$

$$N_2 + OH^+ \rightarrow O + N_2H^+ \tag{5.22}$$

with the latter reaction being the secondary favoured route. With the addition of X-ray emission into an dense-cloud environment, in high nitrogen chemistry (K1 and K3), reaction 5.21 remains the primary reaction, with $H_2 + N_2^+$ now being the secondary favoured reaction. In low nitrogen chemistry (K0 and K2), these reactions are reversed. Reaction 5.22 slips to third choice for all chemistry files. The 'unique' formation route in standard models (see §5.15) is not apparent in dense-cloud models and accounts for less than 4% of N_2H^+ production in dense-cloud with X-ray models. Conversely, reaction routes 5.21 and 5.22 do not feature in N_2H^+ production in standard models (modA) and X-ray models (modA2). It is worth stating again at this point however, that temperatures at $A_V = 7$ in ModB and ModB2 models are approximately 600 K higher than standard and X-ray models. These large variations in temperature undoubtably account for the difference in reaction routes.

SO_2 also shows a disparity in formation routes, though not to the extent of N_2H^+. In the standard models, SO_2 was formed via OH + SO (~58%) or O + SO (~42%), while in the dense-cloud models, the former reaction is now the only reaction for SO_2 formation.

5.3.5 HCO^+ models

The significant increase of HCO^+ at the onset of PN formation, is commonly discussed in molecular studies of PPN and PN. However, the mechanism responsible for the production of HCO^+ is still unclear. A number of authors (see discussion above §5.2) have suggested that X-ray emission from the central star may contribute to large abundances of H_3^+, thus forming HCO^+ by reaction 5.13. Whilst an enhancement of X-ray emission in chemical models can increase abundances, the column densities of HCO^+ are still below those observed. In the X-ray enhanced models of Ali et al. (2001), their calculated fractional abundances of HCO^+ are a factor of 5 less abundant compared with observations. In the models by Kimura et al. (2012) the $N(HCO^+)/N(CO)$ ratios could be explained by the presence of a hot star alone with a temperature of ~1.5 x 10^5 K. In this work, HCO^+ column densities are increased by a factor of 2−3 in X-ray models over standard models. However in comparison with observed column densities, HCO^+ is a factor of 12 lower across standard models and an order of magnitude lower in X-ray models (at A_V = 7). Similarly, a dense-cloud environment does not serve to increase HCO^+ column densities, instead, the observed column density more closely resembles that of the standard models.

Accordingly, from the contribution of models to date, it would suggest that an increase in X-ray emission is not required to produce large abundances of HCO^+. To ascertain if a specific chemical enhancement rather than an increased ionisation flux could contribute to the high column densities of HCO^+, a number of select reaction rates involving H_2O have been increased. These particular reactions have been manipulated

Table 5.6: Modified H_2O Reactions in K4All and K5All chemistry files.

Reaction	Standard Value	New Value
$C^+ + H_2O \rightarrow HCO^+ + H$	7.00 (-10)	2.70 (-09)
$H_2O + CN^+ \rightarrow HCO^+ + NH$	1.60 (-10)	2.70 (-09)
$H_2O^+ + CO \rightarrow HCO^+ + OH$	9.00 (-10)	0.31 (-09)
$H_2O + CO^+ \rightarrow HCO^+ + OH$	8.84 (-10)	0.90 (-09)
$H_2O + C_2N^+ \rightarrow HCO^+ + HCN$	7.00 (-10)	2.70 (-09)
$H_2O^+ + HCO \rightarrow HCO^+ + H_2O$	2.80 (-10)	2.70 (-09)
$H_2O + C_3H^+ \rightarrow HCO^+ + C_2H_2$	2.48 (-10)	2.70 (-09)
$H_2O + N_2^+ \rightarrow HCO^+ + OH$	5.00 (-10)	0.50 (-09)

as the presence of water-ice in NGC 6302 is well documented by Molster et al. (2001), in addition, gas-phase H_2O has also recently been detected by Bujarrabal et al. (2012). The exploration of gas phase H_2O in these models is twofold; firstly, does H_2O influence the production of HCO^+? Secondly, gas-phase models involving H_2O in PN is infrequently documented, whilst water vapour in circumstellar envelopes (CSEs) on the other hand, has recently witnessed a surge in interest due to the recent detection of gas phase water in the well studied carbon star IRC+10216. It is hoped therefore, that these models will contribute to the ongoing analysis of gas phase H_2O in extreme environments.

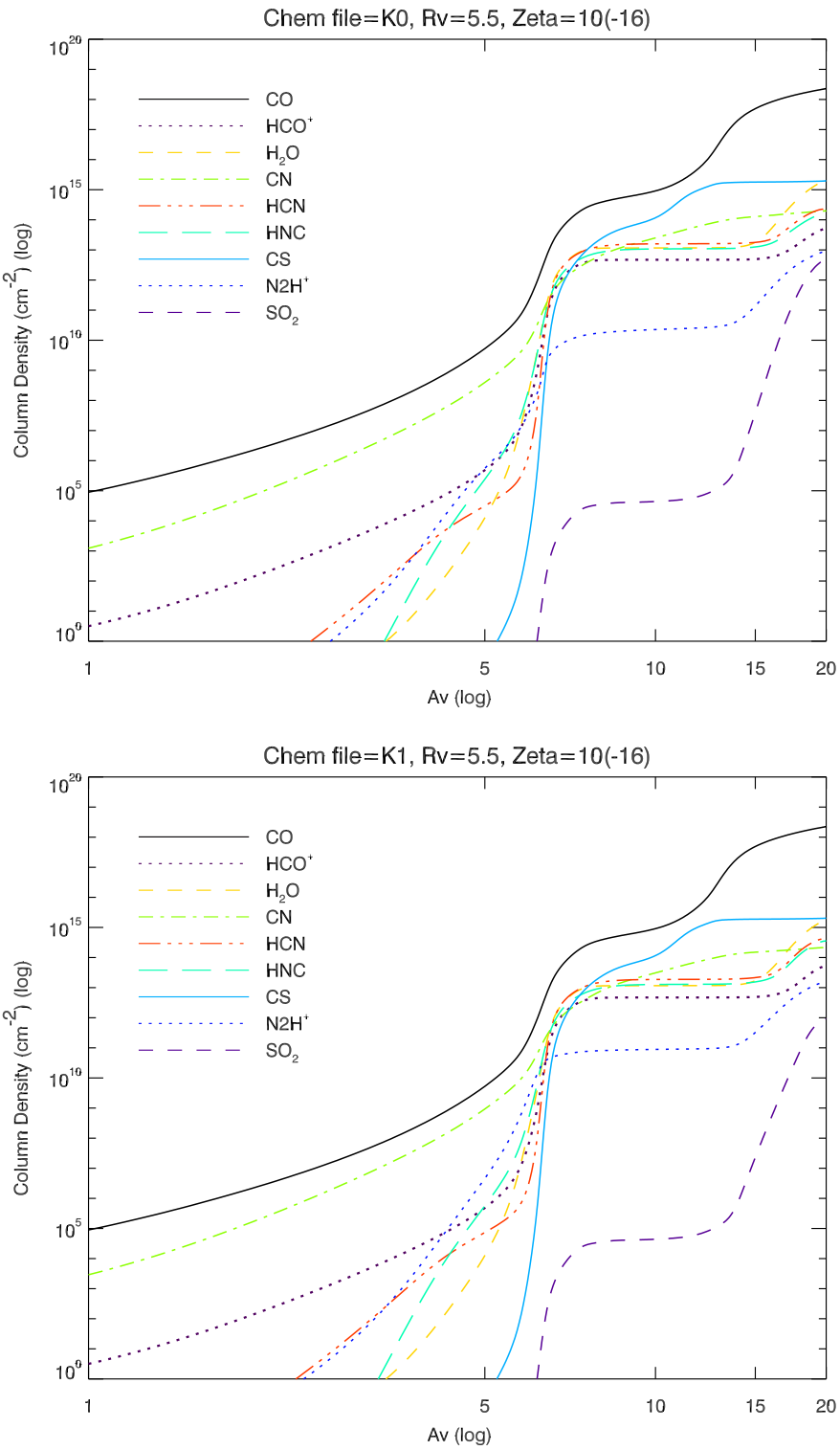

Figure 5.9: Dense-cloud with X-ray models (ModB2). Chemistry file K0 (upper) and K1 (lower).

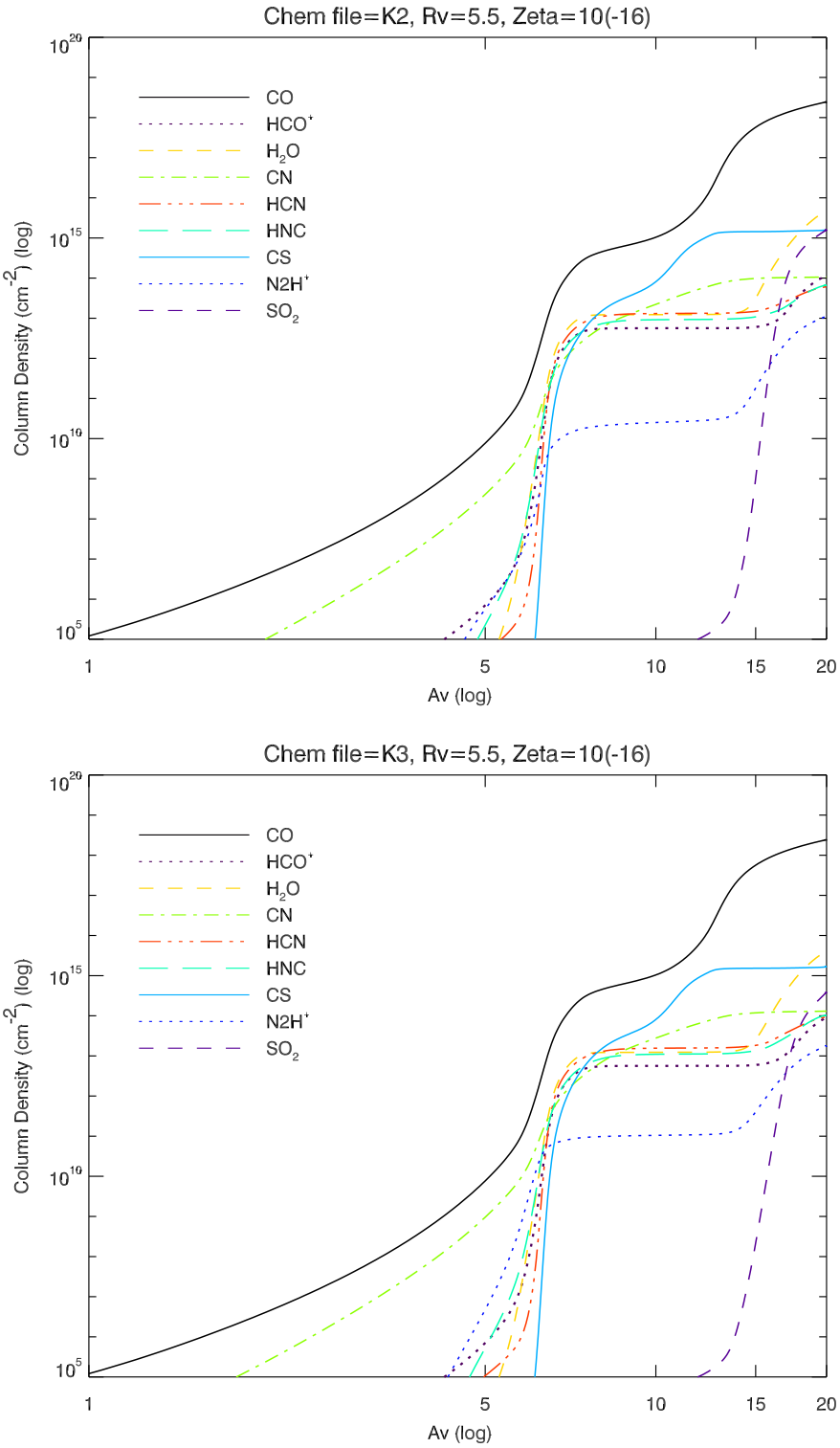

Figure 5.10: Dense-cloud with X-ray models (ModB2). Chemistry file K2 (upper) and K3 (lower).

The formation of H_2O in the gas phase through neutral-neutral reactions is slow at low temperatures, however in a moderately ionised medium, formation can occur more rapidly through ion-molecule reactions. In recent models by Meijerink et al. (2012), the authors explore the possibility of enhancing H_2O abundance in the gas phase in an X-ray exposed environment, using Monte Carlo and rate equation simulations to determine the efficiency at which oxygen is converted into OH and H_2O on dust grains. Interstellar carbonaceous dust grains were used as the catalyst and formation rates of both species were determined for temperatures T_{dust} = 10-60 K. The authors found that the fraction of H_2O released back to the gas phase after formation is 9% and the formation is dominated by the reaction OH + H $\rightarrow$ H_2O. However in the presence of a strong UV radiation field, water on the grain can be photodissociated and subsequently reformed in the gas phase, increasing the effective fraction of H_2O by a factor of 5. The efficiency of converting oxygen atoms arriving on the dust and released into the gas phase as H_2O is near 60% for T_{dust} = 15−40 K, with formation dependant on abundances of O and H (on the grain), and in the gas phase on O, H_2 and OH. Whilst the work was undertaken assuming bare carbon grains and no ice layers, the investigations assumed an O-rich environment with O and H abundances applicable to those in NGC 6302. Similarly the temperature range at which the grains most efficiently form H_2O in the gas phase are within the limits suggested for the torus temperature of NGC 6302.

With this in mind, a search of the literature was conducted for alternative HCO^+ formation rates through reactions with H_2O. It was found that experiments by Huntress and Anicich (1976) and Huntress et al. (1980) produced higher rates than those presented in the UMIST database for the same reactions, namely; $C^+ + H_2O \rightarrow HCO^+ + H$ (enhanced to 2.7×10^9 cm^3 s^{-1}) and $CO/CO^+ + H_2O^+/H_2O \rightarrow HCO^+ + OH$ (enhanced to $0.31/0.9 \times 10^9$ cm^3 s^{-1}). In addition to possibly enhancing HCO^+ abundances, H_2O reactions to produce N_2H^+ were also updated. As noted above, the formation of N_2H^+ occurs predominantly via one reaction path (discussed in §5.3.1) and as N_2H^+ is also associated with low temperature, dense environments, the reaction $N_2^+ + H_2O \rightarrow N_2H^+$

+ OH was enhanced to ascertain its affect on the chemistry. These increased reaction rates are included in the K4All and K5All chemistry files. In addition, the K5All chemistry has enhanced oxygen abundances, whilst K4All has standard abundances as per the K0 chemistry files. Initially, only the three aforementioned reactions were updated in the chemistry files, however, little discrimination was seen between the column densities with the enhanced rates and those with standard reaction rates. It was then decided that all reactions which included H_2O as a reactant in the formation of HCO^+ should be updated. If updated reaction rates could not be sourced in the literature, a value of 2.70×10^{-9} was adopted. Whilst this is a somewhat of an arbitrary value, it is the updated figure from Huntress and Anicich (1976) for the reaction $C^+ + H_2O \rightarrow HCO^+ + H$, which is the most common reaction for HCO^+ production with H_2O. A full list of reactions and rates is presented in Table 5.6.

Comparison with column densities from other chemistry files throughout the range of environments modelled above (Table 5.5), show that even with the full range of increased rates for H_2O, no significant affect on HCO^+ or N_2H^+ chemistry is seen. Little distinction between N_2H^+ column density figures is seen between K4All chemistry files and corresponding chemistry files with the same initial nitrogen abundances, K0 and K2, across all models. Similarly, K5All chemistry files which have the same initial nitrogen abundance as K1 and K3, also have approximately the same column density. The column density for HCO^+ on the other hand, remains roughly the same, regardless of any enhancement (N, O or increased H_2O rates). This pattern, for both HCO^+ and N_2H^+ column densities, is seen throughout all of the modelled environments.

In regards to the formation of HCO^+ via H_2O, the increased reaction rates do not produce substantially increased abundances of HCO^+, via any of the reactions listed in Table 5.6. The reaction $H_2O^+ + CO \rightarrow HCO^+ + OH$, for example, is endothermic and has an activation barrier of ~300 K (Cherchneff 2011). Temperatures at $A_V = 7$ in standard and X-ray models is $\sim$ 160K (see Figure 5.4) and hence is the likely reason

this specific reaction is not significant in HCO^+ production. Similarly, the precursors to H_2O formation are slow at low temperatures. The neutral-neutral reactions OH + $H_2 \rightarrow H_2O$ + H and O + $H_2 \rightarrow$ OH + H only contribute at temperatures T > 250−300 K due to activation barriers. H_2O *is* effectively produced in the Meudon models in all modelled environments and is primarily produced by $H_3O^+ + e^-$ at temperatures ∼200 K. H_2O column densities are one of the highest of all modelled species and are at maximum in X-ray models, so to, are column densities for HCO^+.

Throughout all of the chemistry files, the production of HCO^+ via H_2O is generated by only one reaction, that of $H_2O + C^+ \rightarrow H + HCO^+$. In chemistry files K0 − K3 (non-enhanced H_2O reaction files), this reaction is only found in K1 (N-rich) chemistry files for standard models (ModA), and in K0 through K3 chemistry files for X-ray models (ModA2) . This reaction is absent in K0 − K3 chemistry files throughout dense-cloud models (ModB) or in dense-cloud with X-ray models (ModB2). It is included however, in all K4All and K5All chemistry files regardless of the modelled environment. Production of HCO^+ via H_2O accounts for ∼3% in K0 − K3 files and around 6% in K4All and K5All chemistry files. Whilst formation of HCO^+ is doubled via $H_2O + C^+$, the main production route of HCO^+, does not differ from that described above; for standard and X-ray models, HCO^+ proceeds via CO + H_3^+, with CO + N_2H^+ as the secondary pathway. In the dense-cloud models HCO^+ is formed primarily by reactions O + $CH_2^+ \rightarrow$ H + HCO^+ which competes with reaction O + $CH_3^+ \rightarrow H_2 + HCO^+$ to dominate production. To summarise, within the framework of these models, enhanced H_2O reactions do not influence HCO^+ chemistry to any significant degree.

5.3.6 Comparison with Other Models

Whilst a growing portfolio of atomic, ionic and molecular species are observed within PN, a few core species are regularly observed and investigated, namely CO, HCO^+, CN, HCN and HNC. Perhaps unsurprisingly Kimura et al. (2012) limit their analysis

to these select molecules in order to compare their results with observational data. Indeed, as seen in Chapter 3, these species are most readily detected in NGC 6302 and form the core of our analysis. The work undertaken by Kimura et al. (2012) is similar to the models produced in this study and thus provides comparative data in which to assess the results here.

The numerical code (Aangaba) utilised by Kimura et al. (2012) is described by Aleman and Gruenwald (2011) (and references therein) and is thus only summarised here. The Aangaba code is similar to the Meudon Code whereby the incident radiation at a particular position in the nebula determines the thermal and chemical structure of the gas. The physical conditions of the gas (temperatures and densities) are hence calculated in an iterative manner as the simulation proceeds from the inner border of the nebula, and extends outwards. The chemical network consists of 95 molecules and 1693 reactions based on the UDFA 2006 catalog (Woodall et al. 2007). Rate coefficients are also taken from UDFA 2006, except for those of photo-processes and the H_2 network reactions. The energy source for the nebula is represented by a central star with additional radiation supplied by X-ray emission (0.3 - 2 keV) to simulate a hot bubble environment. The nebula is assumed to be spherical symmetric with an homogenous chemical composition throughout. Kimura et al. (2012) identify four main chemical regions in their PN structure; H^+, H^0, H_2 and CO, where CO is fully associated and locks up the lesser abundant C or O atoms. This region can be defined by the following characteristics; a low CO dissociation rate, oxygen preferentially in CO form, nitrogen is predominantly molecular (N_2) and heating of the nebula is primarily via cosmic rays. Kimura et al. (2012) note that the extent of the transition zones between regions depend upon the stellar and nebula characteristics and that such regions may impede or enhance molecular production due to the presence of one or more forms of a given element. The CO transition zone is apparent in the Meudon models around $A_V = 3$. As noted above, the models of Kimura et al. (2012) include an X-ray flux, which correspond to X-ray models (ModA2) in this work. A comparison of the column densities of HCO^+, CN,

HCN and HNC against CO is displayed in Figures 5.15.

As can be seen, the formation paths of HCN and HNC are tightly coupled in both models, however HCO^+ and CN follow somewhat different evolution routes in the two models. HCN and HNC column densities are roughly an order of magnitude greater and nearly an order of magnitude lower respectively, in the Meudon models compared with column densities of Kimura et al. (2012). HCO^+ is the only species which is comparatively similar for both sets of models, albeit it is slightly under produced in this work.

Kimura et al. (2012) discuss that for the HCO/CO ratio, the effects of X-rays on the models are comparatively negligible and results can be explained solely with the inclusion of a very hot central star. The CN/CO ratio on the other hand cannot be reproduced without the addition of a hot bubble X-ray emission. The Meudon code is adapted to *simulate* X-ray emission for this work, whereas the Aangaba code of Aleman and Gruenwald (2011), treats X-ray emission in a comprehensive manner by introducing a specific X-ray luminosity at 5 x 10^{31} ergs s^{-1}. This most certainly accounts for the differences in column density figures between the two sets of models.

In addition to X-rays, Kimura et al. (2012) state that the subsequent parameter to which molecular chemistry is most sensitive, is the dust to gas mass ratio (M_d/M_g. This parameter is varied throughout their grid of models between 10^{-2} and 10^{-3} but is fixed at 5 x 10^{-3} for their standard model. Kimura et al. (2012) suggest that the affect on molecular chemistry through interaction with dust is via absorption of radiation, as a catalyst for H_2 production and finally, through heating of the gas through the photoelectric effect. A higher dust to gas ratio corresponds to a smaller H^0 region and an increased H_2 region, which consequently produces a higher density of ionised species and increased production of ion-molecule reactions. The dense-cloud models in this work, are perhaps the most comparable to the findings of Kimura et al. (2012) in re-

spect to this aspect. Results from ModB models show, that despite the O-rich nature of the gas, alternative C and H_2 reactions which are not apparent in O-enhanced chemistry in standard models. These reactions proliferate due to higher gas temperatures at larger A_V (see §5.3.4). The larger R_V in the dense-cloud models produces reactions which are otherwise absent from standard R_V models.

Overall, whilst the addition of hot bubble X-ray emission may be required by Kimura et al. (2012) to reproduce the observed CN/CO ratio (obtained from the observational data of Bachiller et al. (1997) and Josselin and Bachiller (2003)), equivalent X-ray enhanced column densities for CN in the Meudon models, are too high. Standard models in this work provide consistently lower CN column densities, and hence are more comparable to the observed column density figure for CN (N_{tot} = 4.40 x 10^{13} cm^{-2}). This leads to the conclusion, that chemistry within NGC 6302 has not yet been affected by X-ray emission. This conclusion is agreeable with the recent *Chandra X-Ray Observatory* survey (CHANPLANS) by Kastner et al. (2012) who found no X-ray source within NGC 6302. The survey by Kastner et al. (2012) suggests that the presence of X-ray sources (either point-like or diffuse) within PN appears correlated with PN density structure, whereby molecule-rich, bipolar or ring-like nebula are less likely to display X-ray emission, compared with molecule-poor, elliptical nebula, which generally have detectable X-ray sources. The X-ray emission is categorised as either diffuse X-ray or point-like X-ray, with point-like sources further sub-grouped as soft X-ray sources (hot, ~ 100-200 kK, photospheric components) and hard X-ray sources (dominated by photons in the range ~0.6-1.0 keV). Of the 35 sampled objects (including archival data), Kastner et al. (2012) find an overall diffuse and/or point-like X-ray detection rate of ~70%. Diffuse X-ray sources are suggested to arise from strong shocks due to wind interaction ('hot bubbles') and are spatially confined within sharp-rimmed shells. Point-like soft X-ray sources are described as having a narrow range in PN radius (around ~0.1-0.4 pc) corresponding to a well-defined but short dynamical timespan. The epoch of detectable soft X-ray emission equates to a dynamical PN age of ~10^4

yr. Conversely, hard X-ray sources span a wide range of radii and suggest either a combination of short-lived and longer-timescale processes, intrinsic to the central star of the planetary nebulae (CSPN). Kastner et al. (2012) provide a description of these processes, however potential explanations involve CSPN with late-type companions or dynamical old PNe with binaries. NGC 6302 is suggested to not have a binary companion (Szyszka et al. 2009) and has a torus dynamical age of ~7500 yr (with the optical lobes possibly formed at a later stage) (Peretto et al. 2007). Based on the observations of Kastner et al. (2012), it is possible that the CSPN of NGC 6302 has not yet reached the timespan required to produce point-like X-rays. If NGC 6302 does have an X-ray source, it is too faint to be detected by (CHANPLANS).

5.3.7 Comparison with Observed Column Densities

The column densities calculated in this work are approximately the same order of magnitude as the model predictions, depending on the model and the species in question. The CN observed column density figure, for example, correlates most closely to standard model column densities. The chemistry file within ModA which provide the most comparable figures is K2 (high initial oxygen and low initial nitrogen abundances), however, N enriched chemistry models differ by only 2 to 3 factors. Similarly the K2 chemistry file in ModA2 models also provide comparative figures, whereas the rest of the chemistry files within ModA2 are a factor of 3−4 too high. On the other hand, column densities for HCN are nearly two orders of magnitude lower in standard models than the observed column densities and at $A_V = 7$ are an order of magnitude too low in X-ray models for N-rich chemistry. The observed column density for HCN correlates most closely with ModB2 models (dense-cloud with X-rays), with O-enhanced chemistry.

Whilst ^{13}CS is detected and calculated in this work, CS is the species modelled due to limitations in the Meudon chemistry file. The observed N_{tot} for ^{13}CS is 6.9×10^{12}

cm^{-2}. By adopting a $^{12}C/^{13}C$ ratio of 19 (see §4.3.3) and comparing with the modelled column density figures in Table 5.5, it can be seen that dense-cloud models at an A_V = 8 provide the closest comparison. Chemistry files of lower initial O abundances (K0, K1 and K4All) produce the highest figures at $\sim 2.41 \times 10^{13}$ cm^{-2}, however, these are still a factor of 5 too low. Column density figures for CS in standard models to not change significantly between A_V = 7 and A_V = 8 and are the most discrepant with observed N_{tot} for all modelled environments. The column densities for CS between A_V = 7 and A_V = 8 in X-ray models increase by a factor of seven, whilst those for dense-cloud models (and dense-cloud with X-rays) increase by over an order of magnitude. It would appear therefore, that to obtain high column densities for CS, either an increase in flux or increased gas temperatures in a dense-cloud environment is required to increase the abundances for this species.

Although this large difference in column densities for CS is seen between A_V = 7 and A_V = 8, for some species little deviation is seen over this range. For instance, N_2H^+ has a typical difference of less than a factor of 2 between A_V = 7 and A_V = 8 over dense-cloud and dense-cloud with X-ray models. For the standard and X-ray models however, a factor of 5−6 increase is seen across all chemistry files. HCO^+ has a smaller increase of a factor of 2−3 difference at A_V = 8 across all models, except for standard models, which produces little variation across the A_V range. Nonetheless, HCO^+ is still under produced in standard models compared with observed column densities by a factor of 12 at A_V = 7 and a factor of 10 at A_V = 8. This decreases in ModA2 models by a factor of 10 at A_V = 7 and a factor of 5 at A_V = 8.

Minimal variations in the column densities are seen between O-rich and N-rich chemistry files between all species. CS appears particularly unaffected by differing N and O abundances in ModB and ModB2 models. For HCN, a factor of 2 increase is seen in column densities for N-rich files compared with O-rich chemistry in standard models. When X-rays are introduced, N-rich column densities rise slightly by a factor of

3. A similar trend is observed in the column density figures for N_2H^+ in dense-cloud models (and the dense-cloud with X-ray models), and to a lesser degree in the standard models. CN also displays a larger column density (by a factor of 3) for N-rich chemistry files in standard conditions. This trend decreases in dense-cloud models at A_V = 7 by a factor less than 2 and in dense-cloud with X-ray models at A_V = 7, CN column densities across all chemistry models are approximately the same.

Table 5.7: Comparison of Observed Column Densities with Best-Fit Model Results

Species	Observed Column Density (cm^{-2})[a]	Modelled Column Density (cm^{-2})	Model Name / Chemistry file
HCO^+	2.13 (13)	5.99(12) (A_V = 8)	X-ray enhanced (ModA2) / K2
CN	4.40 (13)	5.97(13) (A_V = 7)	Standard (ModA) / K2
HCN	2.13 (13)	1.51 (13) (A_V = 8)	Dense-cloud with X-rays (ModB2) / K1
^{13}CS	1.38 (14)[b]	2.41(13) (A_V = 8)	Dense-cloud (ModB) / K0
N_2H^+	1.6 (12)	1.65(12) (A_V = 8)	X-ray enhanced (ModA2) / K0

[a] All rates/abundances in the form; a(b) = a x 10^b
[b] Taking into account a $^{12}C/^{13}C$ ratio of 19 as ^{13}CS is observed but CS is modelled

In summary, the observed column density figures are not represented comprehensively by one particular set of models, but rather a selection of modelled environments provides a reasonable comparison with observed column densities (see table 5.7 for a comparison of modelled results with observed column densities). X-ray models provide the closest comparison with observed column densities for HCO^+ and N_2H^+, whilst CN corresponds with standard model conditions. Dense-cloud conditions are preferred by HCN and CS, which shows a preference for all conditions except the standard ones.

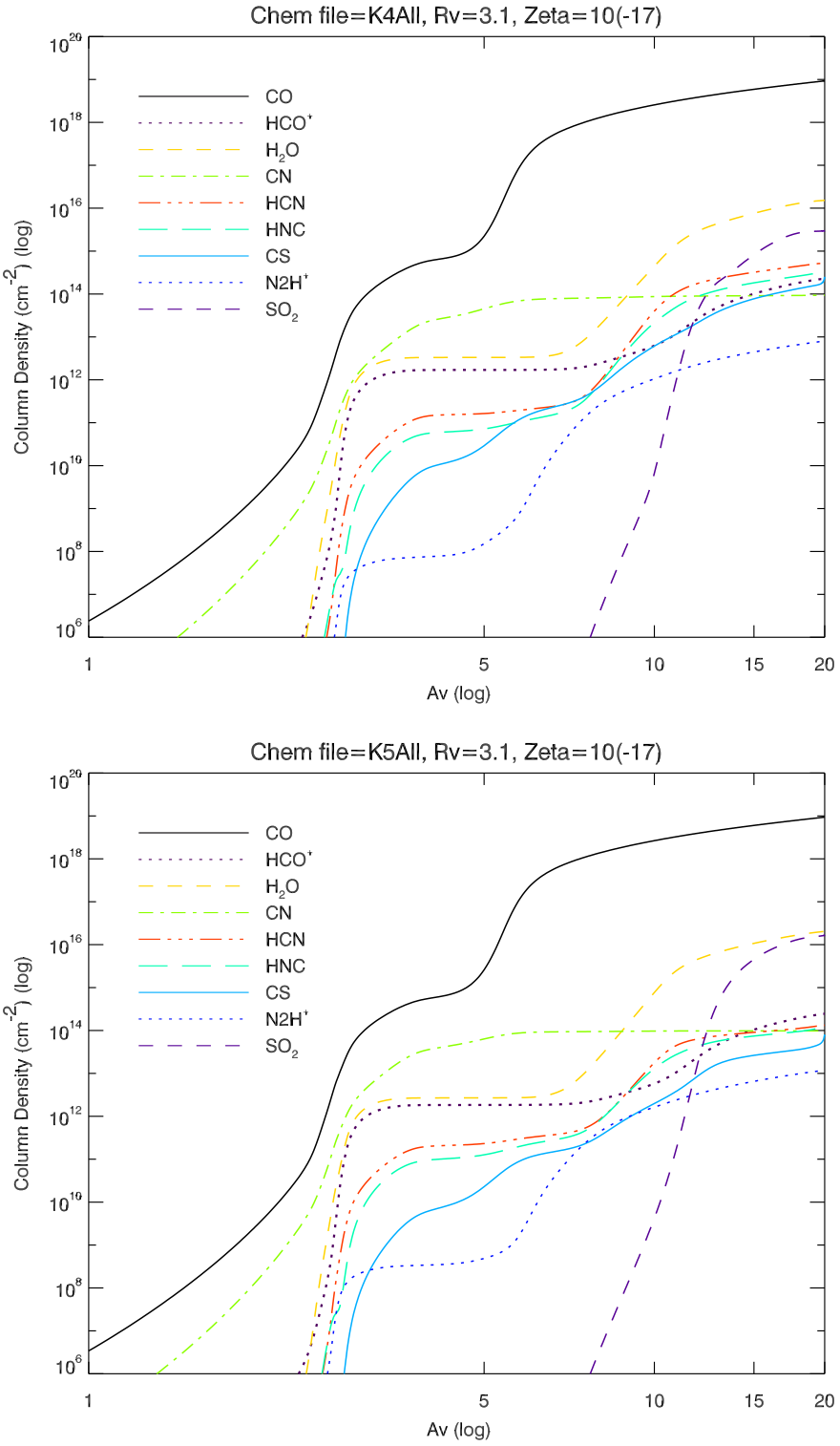

Figure 5.11: Standard models (ModA). Chemistry file K4All (upper) and K5All (lower). Both models include increased reaction rates for $N_2^+/C^+/CO$ with H_2O to form HCO^+.

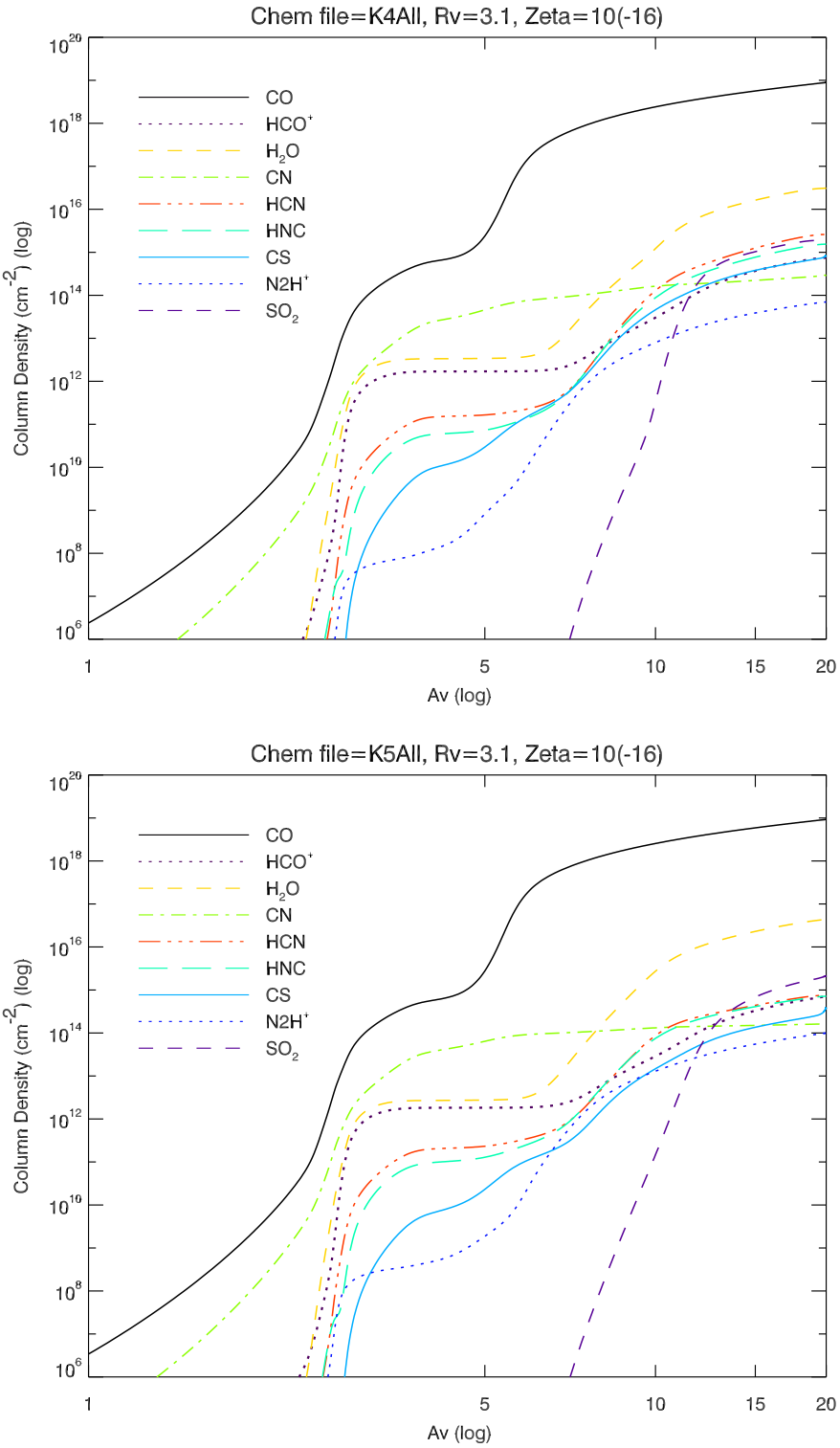

Figure 5.12: Excitation enhanced models (ModB). Chemistry file K4All (upper) and K5All (lower). Both models have increased reaction rates for $N_2^+/C^+/CO$ with H_2O.

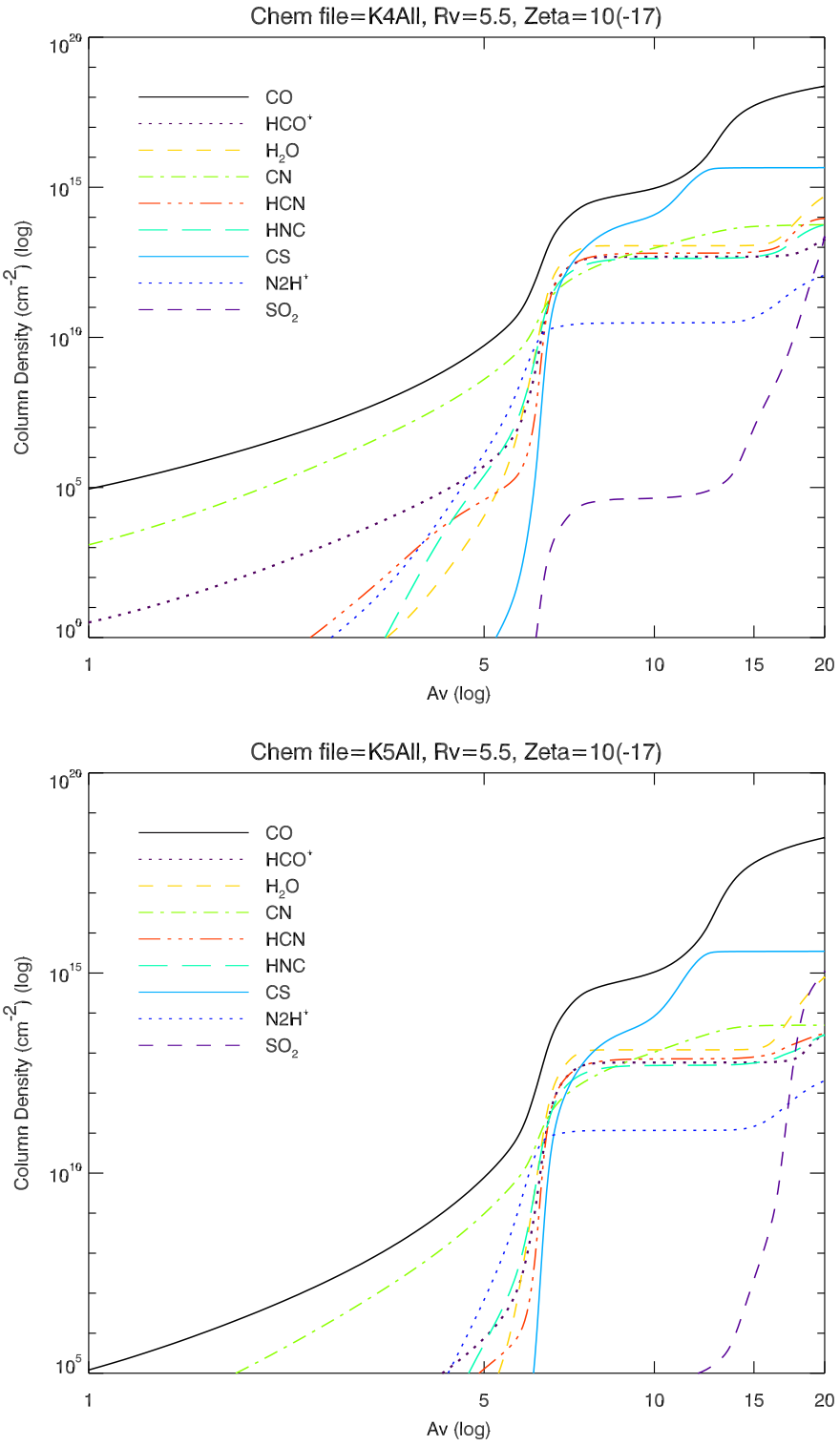

Figure 5.13: Dense-cloud models (ModB). Chemistry file used K4All (upper) and K5All (lower). Both models have increased reaction rates for $N_2^+/C^+/CO$ with H_2O.

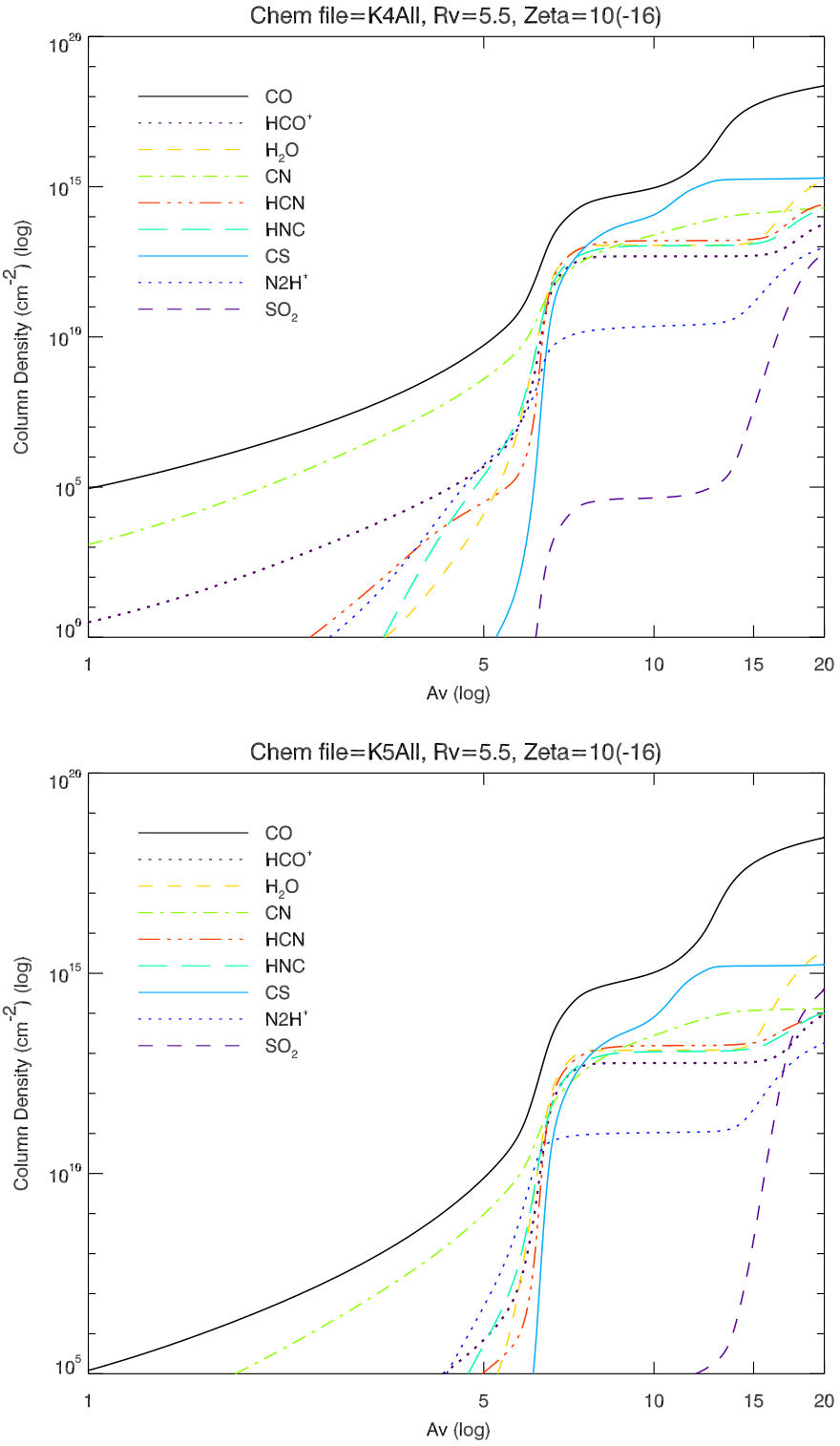

Figure 5.14: Dense-cloud with excitation models (ModB2). Chemistry file used K4All (upper) and K5All (lower). Both models have increased reaction rates for $N_2^+/C^+/CO$ with H_2O.

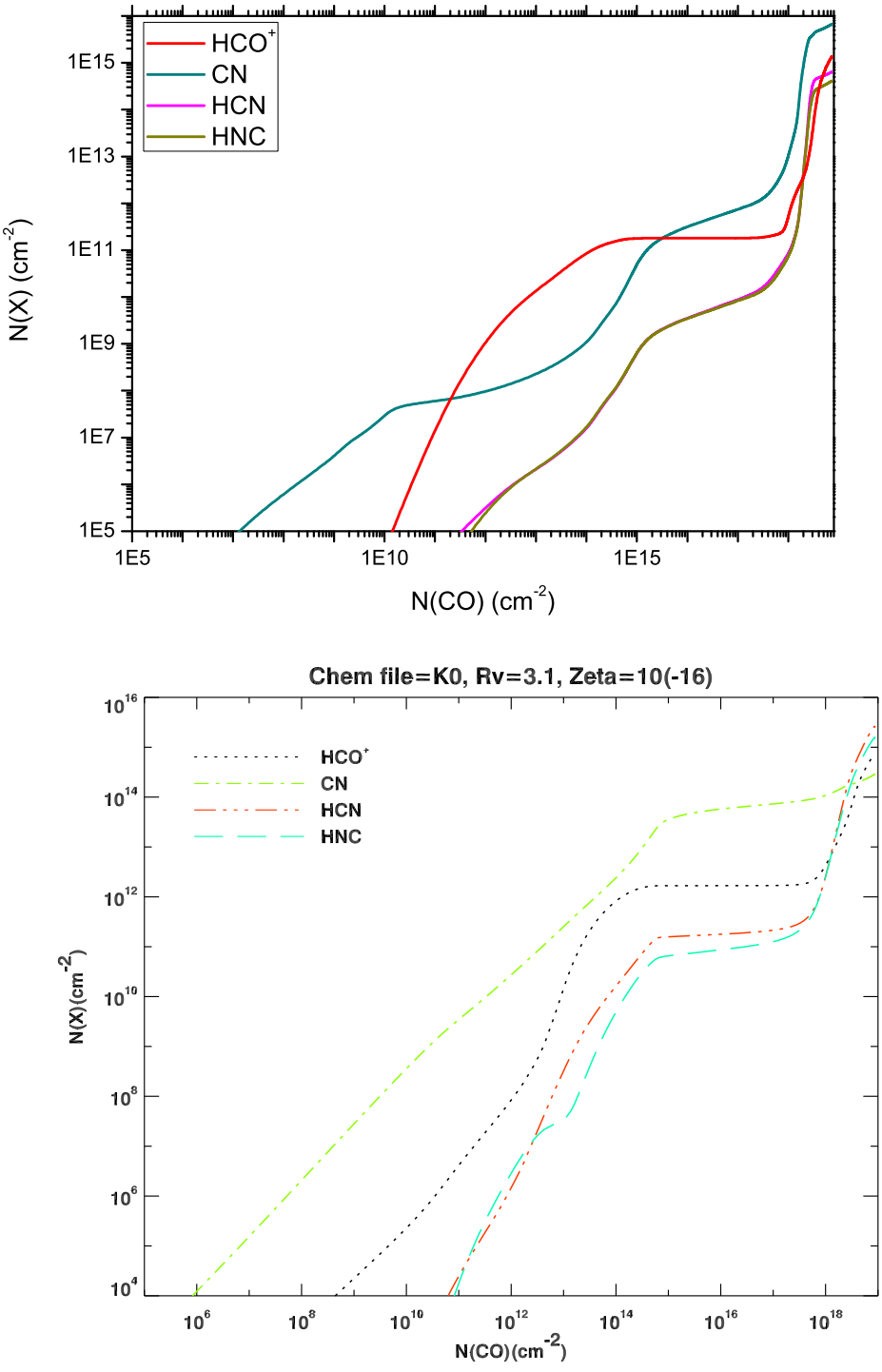

Figure 5.15: Comparisons of column densities from Kimura et al. (2012) (upper) (private communication) and from this work (lower). Model parameters in this work include simulated X-ray emission (ModA2) and are based on standard chemistry (K0 chemistry file).

6

Discussion

It would appear that the basic structure of NGC 6302 is quite well delineated and can be crudely separated into two components; a cold, dense, equatorial torus and warm, extensive bipolar lobes. This model is supported by numerous observations but in particular by Kemper et al. (2002) and via Peretto et al. (2007) from their CO observations which trace the torus. Through analysis of the full ISO spectrum Kemper et al. (2002) derived the mineralogical composition of the dust and distinguished a warm component at 100 K containing C-rich dust and a cool component containing the bulk of the material at 50 K, dominated by oxygen-rich material. This latter feature shows strong emission from crystalline silicates, water ice and carbonates and is argued to originate from a central torus. The former describes material predominantly in the bipolar optical lobes. Confirmation of a cool dust component is also presented by Molster et al. (2001) who identify features at 91 μm and infer the existence of a stable disk, promoting the growth of large, and therefore, cold grains. Recent submillimeter observations by Bujarrabal et al. (2012) of CO, OH, NH_3, and H_2O also suggest a temperature of ~40 K.

Confirmation that a rich molecular chemistry is thriving within the torus of NGC 6302 is presented in the observations themselves. The images of all the observed species discussed in chapter 3 are all within the confines of the ^{12}CO, thus confirming their

association with the torus. Emission for all the species show strong correlation with the brightest peaks of ^{12}CO, with the exception of SiO, however, the spatial distribution of individual species is markedly different, thus giving some indication as to the mechanisms involved in producing the emission. It can be seen that the majority of species are extended in the less-dense southern section of the torus, with most species also showing extended emission towards the east, in the direction of the eastern bipolar lobe. The HCN medium velocity component is elongated to the southwest whereas the high velocity component is enhanced to the east. ^{13}CS similarly extends to the east, as do the $v = 0$ and $v = 1$ transitions of SiO, whose maser-like emission is concentrated on the eastern edge of the respective medium and high velocity components. HCO^+ is prominent in the south, along with CN which also extends to the east. The peak of ^{13}CN is shifted to the west, whilst N_2H^+ is centred completely on the inner CO emission. This perhaps is to be expected as N_2H^+ is typically associated with dense gas (Johnstone et al. 2010) and observations of this species in planetary nebulae are limited.

The column densities for species observed in this work were calculated with an excitation temperature, T_{ex}, of 25 K, however as previously noted (§4.3) it was found that increasing the excitation temperature to 100 K had little effect on column density figures. Nonetheless, comparison with the various models constructed utilising the Meudon code show an agreeable fit to these calculations, indicating that a rich and varied chemistry is flourishing in NGC 6302, despite the extreme input parameters used to model the chemistry (§5.3).

6.1 Methods of Excitation

The HST and VLT images of Matsuura et al. (2005) provide perhaps the most coherent images of the whole of the compacted structure of NGC 6302 (i.e. neglecting the

extended emission of the northwestern lobe, which at the farthest extent reaches 3.′0 from the central star). In Figure 14 of Matsuura et al. (2005), evidence for multiple orientated axes are presented, whilst their Figure 8 shows a number of filaments, edges of the south-south-east and northeast outflows and a central cavity on the eastern edge of the central dark lane (also shown as Figure 1.4a in this work). Matsuura et al. (2005) state that the central region shows evidence for interaction between the dense gas and the fast stellar wind, resulting in thin shock fronts, whilst the bi-polar outflows are constrained by equatorial density enhancements. Matsuura et al. (2005) also identify a significant north-south extinction gradient within the dark lane, where the highest values are found to the north of the ionised inner shell. The elongated emission of both the HCO^+ and HCN medium velocity components in this work (Figures 3.7 and 3.2 respectively) are possibly an indication of the density gradient of the nebula. Both species show broadened emission in the south compared for instance with N_2H^+ emission, which is a compact structure centred on the brightest ^{12}CO emission. N_2H^+ is considered a dense gas tracer (Johnstone et al. 2010) and emission in NGC 6302 does not extend beyond the inner contours of ^{12}CO emission, thus suggesting a region of dense gas. On the other hand, HCN and HCO^+ are high-dipole moment species and require an excitation mechanism (Sahai et al. 1994), if the torus does have an extinction gradient, UV photons will be less attenuated in regions of decreased dust and gas i.e. the south region of the torus. Consequently the increased ionisation will heat the gas and drive the photo-chemistry required for the HCO^+ and HCN emission.

Further evidence of HCO^+ enhancement by excitation, can be seen in the low velocity component emission (Figure 3.6) when compared with the low velocity component of Peretto et al. (2007). The ^{12}CO low velocity component of Peretto et al. (2007) (Figure 3.5), is a double peaked structure, with the brighter peak offset from the continuum peak by $\sim 7''$ to the south. When overlaid on the Hα image of Matsuura et al. (2005) (Fig 3.5 in this work and Figure 5a in Peretto et al. (2007)), it can be seen that brightest CO peak is coincident with the bright emission of the eastern lobe, and is located on

the edge of the south-south-east outflow. The peak of HCO^+ emission in the HCO^+ low velocity component traces the brightest peak of ^{12}CO only and is elongated northwards, in the direction of increased Hα emission. The positioning of both bright peaks (CO and HCO^+) would hence suggest some affiliation with the outflows of the eastern lobe and Hα emission. The positioning of the lower, less-bright peak of the ^{12}CO low velocity component, also correlates with ^{12}CO emission observed by Dinh-V-Trung et al. (2008). Observations by Dinh-V-Trung et al. (2008) of NGC 6302, detect ^{12}CO emission at more extreme velocities ($\gtrsim$15 km s^{-1}) at redshifted (-18 to -10 km s^{-1}) and blueshifted velocities (-75 to -48 km s^{-1}). Within these ranges, Dinh-V-Trung et al. (2008) advise that the emission appears as discrete knots in their maps, and attribute some to molecular bullets, a type of compact, high velocity outflow seen in other young PNe. Examples of such knots are detected at -64 km s^{-1} and at -16 km s^{-1} (see Figure 1 in Dinh-V-Trung et al. (2008)). After examination of the knots by the authors, Dinh-V-Trung et al. (2008) argue that the knots in the blueshifted high-velocity part of the envelope show a linear velocity gradient. These knots flow in an east-west direction and are offset from the major nebula axis. The authors also note that these components are located within the optical bi-polar lobes of the nebula. The knot at -64km s^{-1} is located close to the lower, less-bright peak of the ^{12}CO low velocity component and at -60 km s^{-1}, the ^{12}CO emission of Dinh-V-Trung et al. (2008) resembles the double peaked structure identified by Peretto et al. (2007). If this is an outflow, the low velocity HCO^+ component could be associated with this phenomena and the two could have a common underlying excitation mechanism.

It would appear in this instance that photoionisation from a shock or UV radiation or from outflow rather than a chemical enhancement is responsible for HCO^+ emission. The case for enhanced HCO^+ column densities via chemical enhancement of H_2O is discussed below, but is not favoured.

Multiple bipolar outflows in NGC 7027, responsible for HCO^+ and HCN emission

have recently been presented by Huang et al. (2010). HCO^+ and HCN show a very similar structure to those presented here, with fast redshifted and blueshifted components tracing an expanding equatorial torus. These fast components, identified by wings in the spectra, are similar in location and velocity to previously observed high-velocity CO emission (Huang et al. (2010) and references therein). The HCO^+ and HCN fast components are identified by the authors as likely products of two kinematically different bipolar outflows, which possibly originate from accelerated molecular material (by unseen collimated jets) impinging into the molecular envelope of the nebula. Huang et al. (2010) also state that the flow axes of HCN and HCO^+ are not aligned with the major axis of the central HII region and the envelope of NGC 7027 and hence could represent a single (or multiple) jets that changes its direction. The HCO^+ emission from the rim-brightened torus of NGC 7027 on the hand, is attributed to photochemistry in a PDR. Huang et al. (2010) suggest that either a chemical enhancement (by PDR or shock chemistry) or high densities or temperatures (similarly arising from a shock or UV heating) causing localised, favourable excitation conditions could explain the enhancement of strong HCO^+ emission in NGC 7027. Alternatively all of these scenarios could be contributory factors. HCO^+ emission arising from shocks was discarded as a possible cause due to previous observations of AFGL 2688, a PPN with shocked molecular regions but no ionised region and no HCO^+ emission (Huang et al. 2010). Evidence of shock ionisation from strong winds and energetic outflows have already been presented for NGC 6302 (see for example Lame and Ferland (1991) and Meaburn and Walsh (1980)), nonetheless, observations of these phenomena are confined to the high-ionisation region of the nebula and do not appear associated with the central torus.

It is possible therefore, that while the HCO^+ and HCN medium velocity component emission in NGC 6302 is most likely attributed to enhancement by UV photons, the excitation mechanism for the HCO^+ low velocity component is unclear. The compact nature of its emission, coincident with one bright peak of a double peaked ^{12}CO com-

ponent, could be indicative of excitation by an outflow associated with the edge of the main bipolar lobes or a as yet unseen, smaller more collimated outflow.

Emission of a number of species is either located on the eastern side of the torus, edging towards the eastern bipolar lobe, or elongated in that direction. The HCN high velocity component, CS emission and tentative detection of $^{29}SiC_2$ are elongated, whilst SiO is on the eastern side of the torus. SiO emission from PPN or PNe is rare, so much so that observations by Bachiller et al. (1997) concluded that this species disappears in the PPN phase and should not be detected in PN. It is interesting then, that not only have two transitions of SiO (J=5-4 V=0 and V=1) been observed in this work, but also, the emission displays a sharp, narrow peaked emission, reminiscent of maser emission (Figure 3.13). SiO maser detections in PN are even more rare and accordingly are not present in the literature. Detections of SiO masers are confined primarily to O-rich AGB stars (with OH and H_2O masers), and a few PPN (see for example Nyman et al. (1998)). All three types of masers are usually found around stars presently losing mass and are located in the circumstellar envelopes, with SiO generally located closest to the star. When mass-loss ceases, SiO and H_2O masers disappear first, whilst OH masers can remain active throughout the post-AGB (Kwok 2011).

SiO, however, is also a species associated with warm gas. It can be produced by shocks and can be significantly enhanced at the heads of, and along the axes of, outflows (Bachiller 1996). At the high temperatures in postshock regions, the hydroxyl radical (OH) is formed in large concentrations and through addition with Si, forms SiO via the reaction Si + OH $\rightarrow$ SiO + H (Hartquist et al. 1980). Depending on the formation route, however, the reactions producing OH, have large activation barriers, ~4480 K for O + H_2 and ~9300 for O_2 + H_2. OH can also be formed via H_2S + O $\rightarrow$ HS + OH at ~915 K, however H_2S can be removed through the rapid reaction H_2S + H (Hartquist et al. 1980). SiO production via grain destruction has been addressed by Ziurys et al. (1989), who undertook observations of SiO to ascertain its formation

in a number of cold and dark clouds. Si released through grain destruction in a hot gas allows SiO to form when silicon would otherwise be depleted. Formation via this route was however, dismissed as the main production pathway by Ziurys et al. (1989), as the velocities required to destroy silicate-type grains ($\geq$ 40km s^{-1}) were not present in their objects. Nonetheless, evidence of silicaceous dust being destroyed in the inner nebula of NGC 6302 was discussed by Groves et al. (2002), who found unusually strong recombination lines of Si ([SIII] λ 3862.60 Å, λ 5041.0 Å, and [Si III] λ 3956.64 Å). Coupled with the extraordinary strength of the 1.96 μm [Si VI] and 2.486 μm [Si VII] lines in the infrared, Groves et al. (2002) concluded that the smaller grains found in their observations were probably formed as a result of grain−grain collisions which led to grain shattering. Is SiO in NGC 6302 the result of collisionally pumped material in an outflow, giving rise to maser emission, or is SiO excited due to shock chemistry? The compact nature of the emission in both the high and medium velocity components would suggest localised enhancement indicative of an outflow rather than a shock. If a shock is responsible, then the large volumes of OH expected in postshock gas would be available for additional reactions such as, OH + $H_2 \rightarrow H_2O$ + H, CS + OH $\rightarrow$ OCS + H, S + OH $\rightarrow$ SO + H and SO + OH $\rightarrow$ SO_2 + H. SO_2 observations were undertaken in this work, however, the line was not clearly detected.

CN (along with HCN and SiO) is another species which can be enhanced by shocks, UV photons and X-rays. The medium and high velocity components of CN in this work, however do no intuitively suggest one mechanism over another, as extended emission beyond the ^{12}CO emission is roughly symmetrical in all directions, except northwards. No broad emission in the south is seen and no extended emission towards the eastern lobe is evident either. The higher dissociation energy of CN requires photons of shorter wavelengths, and such photons are absorbed by dust more efficiently. Although X-ray photons have a significant lower photoabsorption cross-section than UV photons and can hence travel greater distances within the nebula, excitation by X-ray for CN emission was not selected based on the observed column density. As the

CN column density is calculated from its hyperfine components, these column density figures are considered accurate. Whilst other authors require the addition of hot bubble X-ray emission to reproduce the observed CN/CO ratio (see Kimura et al. (2012) for models based on observations by Bachiller et al. (1997) and Josselin and Bachiller (2003)), compared with standard excitation models in this work, column densities in X-ray enhanced models are higher than the observed column densities. It is therefore suggested that X-rays have not yet modified the chemistry within NGC 6302, as the CSPN has not yet evolved to the timescale required for X-ray emission (see section 5.3.6).

Observations of N_2H^+ in PN are scarce, however, a recent detection of N_2H^+ in the Red Spider Nebula (Edwards and Ziurys 2013) adds to the somewhat limited observations of this species within PN. It is also observed in NGC 7027 where abundances are described as abnormally high (2×10^{13} cm^{-2}) (Zhang et al. 2008), whilst in the Red Spider nebula, N_2H^+ is the least abundant species observed ($N_{tot} \sim 7 \times 10^{11}$ cm^{-2}) (Edwards and Ziurys 2013). Observed abundances for NGC 6302 in this work sit in between these figures at $N_{tot} \sim 1.6 \times 10^{12}$ cm^{-2} (see Table 4.4). Previous models have been problematic in attaining column densities similar to observed values. Models by Hasegawa et al. (2000) for N_2H^+ column densities in NGC 7027 for example, were several orders of magnitude too low ($N_{tot} \sim 3 \times 10^5$ cm^{-2}) compared with the observations of Zhang et al. (2008). To account for these large differences Zhang et al. (2008) invoke an X-ray flux to produce large abundances of H_3^+, which subsequently result in enhanced N_2H^+ production through the 'unique' reaction $H_3^+ + N_2 \rightarrow N_2H^+ + H_2$. Interestingly, the observed column density of N_2H^+ correlates most closely with X-ray enhanced models in this work (at $A_V = 8$), and indeed the primary contributor for N_2H^+ production in these models is via the aforementioned reaction. However, N_2H^+ in the confines of NGC 6302, is a compact structure located close to the continuum peak, with outer contours that extend into regions of higher density (Figure 3.17). This suggests affiliation with a region of dense gas unaffected by X-rays. If X-

rays had penetrated the densest regions of the torus, column densities for other species would be also be modified. Also, N_2H^+ is not enhanced towards the lower density regions of the eastern optical lobe, like other species noted above, where shocks and outflows could possibly modify column densities as well. The description of N_2H^+ as being associated with dense gas does not fit with modelled column densities however. N_2H^+ in dense-cloud models (ModB models) is over an order of magnitude lower compared with standard models and X-ray models. Nonetheless, differences in the reaction pathways for N_2H^+ are considerably modified in dense-cloud models and the 'unique' reaction as discussed by Zhang et al. (2008) is no longer significant. The primary formation route now proceeds via N_2 + HOC^+, followed by N_2 + OH^+. In dense-cloud with X-ray models (ModB2), production occurs primarily with H_2 + N_2^+ and then via N_2 + HOC^+. Production via N_2 + H_3^+ in ModB2 models accounts for just ∼4%. If N_2H^+ is associated with a dense gas environment, modelled column densities suggest this region should have a high nitrogen abundance and production is likely to occur via reactions produced in ModB models, with a contribution from H_2 + N_2^+. If H_3^+ does contribute to N_2H^+ production via N_2 + H_3^+, it is anticipated to form through interaction with cosmic rays rather than X-rays within NGC 6302.

6.2 'Model' Chemistry

The chemistry files (K0 – K3) used within the various models constructed in this work, reflect the nitrogen and oxygen-rich nature of NGC 6302, with initial abundances of these two species varied in the differing files; K0 and K2 are essentially O-rich, whilst K1 and K3 are N-rich. Within a single modelled environment, however, the column density for most species differs by $\lesssim$ a factor of two (at the same A_V) between the different chemistry files. For example, in standard models, CO, HCO^+, H_2O, CS, and SO_2 have approximately the same column density, regardless of N or O enrichment. This is also seen in X-ray models. In dense-cloud models and dense-cloud with X-ray models, variations between column densities in the different chemistry files becomes

more apparent. Generally, oxygen enhanced chemistry files (K2 and K3) have larger column densities for species such as CO and SO_2, compared with nitrogen enriched chemistry files (K0 and K1). Conversely K0 and K1 chemistry files have larger column densities for species such as N_2H^+. Nevertheless, column densities for some species in ModB and ModB2 models, such as HCO^+, H_2O, and CS, remain similar between all chemistry files. For species such as CN, HCN (and HNC in some models), the reverse is true. CN and HCN have higher column densities in N-enriched chemistry files compared with O-enriched chemistry files in standard and X-ray models. However in dense-cloud models and dense-cloud with X-ray models, column densities become approximately the same.

Whilst a number of factors can influence the chemistry of PNe, shocks and X-rays for example, the one undoubted mechanism which will impact the chemistry, is the strong UV flux from the central star. The density gradient of the nebula, as noted above, also coincides with diminishing CO emission in the southern end of the torus. The incident FUV radiation field will be less attenuated in this lower density region, thus maintaining rapid molecular photoionisation and photodissociation. Consequently, a large electron density is available for dissociative recombination with species such as H^+, C^+ and S^+. As carbon is easily photoionised, it is expected that a large fraction of gaseous carbon is in the form of C^+ when not locked up in CO (Cox et al. 1992). Indeed, at $A_V = 1$, the reaction C + photon $\rightarrow C^+ + e^-$ accounts for ~89% of C^+ formation. This drops significantly to ~20% at $A_V = 3$, whereby reaction $H + CH^+ \rightarrow H_2 + C^+$ is the dominant reaction forming C^+. C^+ is thus available to react with H_2 to form $CH^+ + H$, initiating a sequence of carbon-hydrogen reactions. A large CH^+ density with NH densities can lead to the effective production of species such as CN^+, HCN^+, CN and HCN. Oxygen is primarily in atomic form in the hot HII/HI interface and molecular hydrogen transition layer and similarly reacts with H_2 to form OH + H, again activating an oxygen orientated chemistry. A large OH density in turn efficiently produces H_3^+, H_2O, HCO^+ and SiO^+.

A large OH density is responsible for the synthesis of SO_2 in this work. SO_2 was tentatively detected in NGC 6302 in the SMA observations, however poor signal to noise prevented the spectrum from being included in the final analysis. SO_2 was however incorporated into the Meudon models to ascertain its likely formation in a PNe. It can be seen in Section 5.2, that in standard models (ModA and ModA2), the evolutionary path for SO_2 does not deviate significantly between O-rich and N-rich chemistry files. In dense-cloud and dense-cloud with X-ray models however (ModB and ModB2), SO_2 shows considerable differences. In these latter models, production of SO_2 does not occur until around A_V = 12 in O-enhanced chemistry, whilst in nitrogen enriched chemistry, and chemistry files with a lower initial oxygen abundance, formation occurs around A_V = 6. Whilst the differing chemical abundances determine the onset of formation for SO_2, reaction pathways are comparable throughout all models. In ModA and ModA2 (standard extinction) models, SO_2 is formed via OH + SO (~58%) or O + SO (~42%), whereas in ModB and ModB2 models, the former reaction is now the only reaction for SO_2 formation. Temperatures in the dense-cloud models are around 600 K higher at the same A_V in standard models. Chemistry thus starts to emulate that of the hot HII/HI interface and molecular hydrogen transition layer whereby any free oxygen in dense-cloud environments preferentially reacts with hydrogen to form OH and H_2O.

Further examples of modified chemistry can be seen in other reaction pathways. HCO^+ for example is primarily produced via CO + H_3^+ in standard models, but changes to O + CH_2^+ and O + CH_3^+ in dense-cloud models. H_2O had but one formation route in standard models, that of $H_3O^+ + e^-$. H_2O is predominantly formed through the neutral-neutral reaction of H_2 + OH in dense-cloud models due to the availability of H_2, which is not accessible in the equivalent A_V in standard models. CN and HCN reactions are also transformed. The primary formation route for CN, CH + N → H + CN is still preferred for oxygen-rich chemistry, however in low oxygen and/or high nitrogen chemistry files, the primary pathway is now via $CNC^+ + e^-$. HCN is now formed via the dissociative

recombination reaction $HCNH^+ + e^-$ across all chemistry files, instead of via CH_2 + N.

As discussed above, initial N and O abundances do not notably alter the chemistry within the various models constructed. For some species (HCO^+ for example), little difference between column density figures can be seen across the spread of models. The inclusion of X-rays on the other hand, can enhance column densities for some species by a factor of ∼5−8, (CS, and N_2H^+ for example) nonetheless, reaction pathways between UV and X-ray enhanced models remain largely unaffected. Dense-cloud models however, have a profound effect on reactions for nearly all species. A higher R_V produces greater temperatures at larger A_V compared with standard models, which thus changes the dynamics of the chemistry. A large electron density becomes available for dissociative recombinations in dense-cloud models at $A_V = 7$ and atomic oxygen that would be locked up in CO, is free to react with hydro-carbon species or hydrogen to form hydroxyl. This initiates a sequence of reactions normally found in standard models at a lower A_V (∼ 3). Similarly, column densities are significantly affected for a few species. Compared with standard models, CO is reduced by over four orders of magnitude, with values for SO_2 and CN also reduced, but by a much smaller margin. HCN, HNC, and CS on the other hand, have increased column densities in dense-cloud environments compared with standard and X-ray models.

Comparison of the observed column densities with the modelled values shows that a selection of modelled environments provides a reasonable comparison with observed column densities and that molecular species are not represented comprehensively by one particular set of models. This is perhaps to be expected, as PN environments are not homogenous throughout, but instead are comprised of a clumpy medium, with varying excitation mechanisms to excite different species. Some species are enhanced with the addition of X-rays (HCO^+ and N_2H^+), whilst CN favours standard model conditions. Dense-cloud conditions are preferred by HCN, whereas CS is quite versatile and has high column densities in all conditions except standard ones.

6.3 Water, Water Ice and HCO^+

The rapid increase of HCO^+ from the PPN to PN phase by around two orders of magnitude, has led to many discussions on its formation route (see for example Bachiller et al. (1997) and Cox et al. (1992)). X-ray emission from the central star may contribute to large abundances of H_3^+, thus forming HCO^+ by reaction 5.13 (see §5.2). Whilst an enhancement of X-ray emission in chemical models can increase abundances, column densities for HCO^+ still appear under produced. To ascertain if a specific chemical enhancement rather than an increased ionisation flux could increase HCO^+ column densities, a number of select reaction rates involving H_2O have been increased to ascertain its influence on the production of HCO^+ (see §5.3.5). These particular reactions were manipulated as gas-phase H_2O has recently been detected by Bujarrabal et al. (2012) in NGC 6302. Water-ice in also present and is discussed by Molster et al. (2001).

The detection of gaseous H_2O in PN is otherwise infrequently documented. Aside from the recent detections by Bujarrabal et al. (2012), the majority of observations of gaseous H_2O are centred around H_2O masers. Gas-phase models of H_2O within PN is similarly uncommon in the literature. The recent Herschel/HIFI observations however have starting to address this issue, with Bujarrabal et al. (2012) presenting H_2O detections in a number of objects. Nonetheless, gas phase H_2O in PN has yet to attract the attention applied to water vapour in circumstellar envelopes (CSEs), which has recently witnessed a surge in interest due to its detection in the well studied carbon star IRC+10216. This detection challenged the knowledge of current CSE chemistry, as H_2O was predicted to be almost absent in these environments (Willacy and Cherchneff 1998). Consequently the formation process of H_2O in a C-rich CSE has been highly debated, with a number of different mechanisms postulated to account for the observed abundances. Decin et al. (2010) suggest that warm water vapour could be formed via photochemistry with UV photons deeply penetrating a clumpy CSE. This method is also favoured by Agúndez et al. (2010), however they require moderately low mass-

loss rates (10^{-7} $M_{\odot}$ yr^{-1}) for their modelled abundances. Photochemistry models are dismissed by Cherchneff (2011) as this approach suggests that the dust formation process is hampered by deeply penetrating interstellar UV photons, penetrating as deep as 2 $R_{\star}$ through the clumpy winds. Instead shock-induced chemistry in the inner wind is invoked as the preferred method. All authors use reactions 6.1 and 6.2 (below) as the likely chemical reactions to form H_2O. However for those who favour photochemistry as the dominant process, atomic oxygen is liberated via the photodissociation of ^{13}CO and SiO, whilst shock methods invoke collisional dissociation of ^{12}CO. The formation process of H_2O in an O-rich CSE is not discussed in the literature to the same extent as H_2O in C-rich envelopes. It is noted however that the same reactions (6.1 and 6.2) are proposed as the reaction routes for the formation of H_2O in O-rich CSEs as well (for example see Mamon et al. (1987)).

The models by Cherchneff (2011) propose that H_2O forms in high abundances with respect to H_2 (between 1 x 10^{-6} and 1 x 10^{-4}) close to the star. At a radius of r $\geq$ 5 $R_{\star}$ abundances chemically freeze out gradually to 1.4 x 10^{-7}. The efficiency of the non−equilibrium chemistry is due to periodic shocks in the inner winds and inner envelopes of stars ensuring the formation of O-bearing species in carbon stars and C-bearing species in O-rich Miras. The chemistry is initiated by CO and H_2 which are both destroyed in the post-shock gas (at radius 1.2 $R_{\star}$). Atomic oxygen then reacts with H_2 to form hydroxyl,

$$O + H_2 \rightarrow OH + H \tag{6.1}$$

The high post-shock gas temperatures close to the star ensures that reaction 6.1, with an energy barrier of ~3200 K, proceeds efficiently. Hydroxyl subsequently reacts with H_2 to form;

$$OH + H_2 \rightarrow H_2O + H \tag{6.2}$$

which allows for the formation of H_2O at lower temperatures, due to the faster rate and lower energy barrier of reaction 6.2. In the models by Cherchneff (2011) the formation of H_2O is coupled to that of SiO as both consume OH in their formation (SiO via Si + OH → SiO + H).

Water ice growth around O-rich evolved stars has been extensively modelled by Dijkstra et al. (2003) and Dijkstra et al. (2006), revealing that water ice is an important component in CSEs, and is expected to exist even in the PN phase. Dijkstra et al. (2003) focus on growth methods and sputtering, whilst Dijkstra et al. (2006) study the formation and spectral appearance of water ice as a function of stellar evolution (from AGB to PN phase) whereby the initial mass of the star is 5 $M_{\odot}$. Water ice is produced via gas phase condensation on pre-existing silicate grains in both models. To summarise, Dijkstra et al. (2003) argue that for a given grain size, mass-loss rates govern the ice formation process. Significant ice formation is expected with small dust grain sizes (0.01 μm), favoured due to the reduction of sputtering, coupled with mass-loss rates of 10^{-5} to 10^{-4} $M_{\odot}$ / yr. In models run by Dijkstra et al. (2006), an increase in mass-loss rate is again highly favoured, together with high gas densities and low temperatures. Indeed the model which best suits water ice formation is that described by Dijkstra et al. (2006) as a typical AGB setting (i.e. L = 10^4 $L_{\odot}$, M = 10^{-4} $M_{\odot}$ / yr, υ_{exp} = 15 km s^{-1}) and is used as their default model. This model predicts that 18% of the water vapour will be removed from the gas phase at the outer radius of the envelope. However the depletion can be as high as 60% and 70% for models with extremely high mass loss rate (10^{-3} $M_{\odot}$ /yr) and low gas outflow velocities (~5 km s^{-1}), respectively. Axisymmetric mass loss is also favoured to increase abundances as the formation of an equatorial density enhancement provides suitable conditions for the creation and preservation of water ice growth. It is suggested that the location of observed water ice in the post-AGB star M 1-92, is within a dusty torus, where the outer regions of the torus are found to be free of ice (Dijkstra et al. 2006).

Water ice displays a number of distinct spectral features at infrared wavelengths, including 3 μm (O-H stretch) often seen in absorption (Dijkstra et al. 2006), strong bands at 43 μm and 62 μm and a weak shoulder feature at 52 μm. The latter features, namely 43, 52 and 62 μm are all present in NGC 6302 and according to Molster et al. (2001), these features cannot be explained by enstatite and/or diopside emission alone. Coupled with a cold environment as suggested above (Hoare et al. 1992), the presence of water ice thus becomes a robust identification (Molster et al. 2001). In addition gas-phase H_2O has also recently been detected by Bujarrabal et al. (2012). The H_2O spectra in Bujarrabal et al. (2012) show the distinct main peak and wing feature seen in HCN and HCO^+ and are representative of the medium and high velocity components identified in this work. Unfortunately however, integrated intensity maps are not present in Bujarrabal et al. (2012) for H_2O, to thus establish if the spatial distribution is coincident with these or other species and hence give an indication as to the mechanism involved in producing the emission.

If H_2O and HCO^+ are coexistent in the same nebula in large quantities, does the presence of one species influence the formation of the other, considering H_2O can form HCO^+ through a number of reactions? To date, the significant increase of HCO^+ at the onset of PN formation is discussed mainly in terms of a excitation enhancement by UV photons or X-rays. Cox et al. (1992), who observe HCO^+ in two evolved PNe, suggest a possible formation route for HCO^+ via reaction $H_3^+ + CO \rightarrow HCO^+ + H_2$. However, as dissociative recombination destroys H_3^+ before it can react with CO, this process is not thought to be efficient. H_3^+ is predominantly produced by cosmic rays whereas photons produce C^+ as the major ion, accordingly a high ionisation rate by cosmic rays and/or X-rays is also attributed to HCO^+ production. In gas-phase models of evolved planetary nebulae, Ali et al. (2001) suggest that a high ionisation rate, most likely due to X-ray emission from the hot central star can explain the high abundances of HCO^+. Nonetheless, in models by Kimura et al. (2012) the $N(HCO^+)/N(CO)$ ratios could be explained by the presence of a hot star alone with a temperature of $\sim 1.5 \times 10^5$

K. In the models constructed in this work, HCO^+ is efficiently formed in all models, regardless of chemistry. However it was also found that the increased reaction rates listed in Table 5.6 provide no significant increase in the production of HCO^+ by enhanced H_2O rates (see §5.3.5). The observed column density of HCO^+ in NGC 6302, correlates most closely with those of X-ray models, although only by a narrow margin compared with the remaining models. Observations of HCO^+ in NGC 6302 point to possible excitation by an outflow and/or an increased UV flux (see above §6.1) and not enhancement by H_2O. Whilst H_2O may not increase the abundances of HCO^+, it is also effectively produced in the Meudon models in all modelled environments and is only produced in standard models and X-ray models (ModA and ModA2 respectively) by $H_3O^+ + e^-$ at temperatures ~155−170 K. Reaction 6.2 is only apparent in dense-cloud models (ModB and ModB2) at temperatures ~750 K, and becomes the primary production pathway accounting for ~85% of H_2O formation.

6.4 Conclusions

It is apparent from the models produced in this work, and reinforced by the literature related directly to NGC 6302, that the central torus of this nebula harbours a dense and dusty environment capable of producing a rich and varied chemistry. This is supported by the SMA observations in this work and by the modelled molecular species using the Meudon PDR code, which provide comparable column densities to those observed. The observed column densities of CN and its isotopomer ^{13}CN have been examined using the inherent hyperfine structures within this species, providing a robust method in which to quantify the results. Of the models constructed using the Meudon code, standard models (ModA) correlate most favourably with calculated column densities for CN. CN abundance typically increases with increasing stellar radiation, as the central star of a planetary nebula evolves from its AGB phase to the developing PN. Models thus predict that CN column densities should be an order of magnitude higher than HCN, as the increasing UV radiation photodissociates HCN to form CN Cox et al.

(1992). CN and HCN observed column densities in this work are of the same order of magnitude however, and it thus suggested that the UV flux is highly attenuated by the dusty environment. Accordingly HCN is not fully photodissociated producing the excess CN seen in other PN. Whilst regions of the torus are possibly heavily obscured by dust, the torus is observed to have a north-south density gradient in the nebula (Matsuura et al. 2005). The integrated intensity maps of observed species such as HCO^+ correlate with the density gradient, which display extended emission in this region due to an increase in photoionisation to the south. Contributions from outflows and shocks could also influence the chemistry and are potentially identified by molecular markers such as ^{13}CS and possibly, SiO.

In theoretical models produced by Natta and Hollenbach (1998) of H_2 evolution in the neutral gas of PN, it is suggested that central stars of a planetary nebula (CSPN) with high mass (upper limit of their models = 0.86 $M_\odot$), temperatures > 100, 000 K are reached quickly and soft X-rays will heat and partially ionise the neutral gas. For PN with stars at the upper mass limit, this phase can be present after only 1000 yrs. NGC 6302 conforms to both aspects i.e. high mass and high temperature and is approximately ~1700 yrs old, but the models indicate that X-rays have not yet influenced the chemistry. This is supported by recent findings by Kastner et al. (2012), who have performed an X-Ray survey on a number of PN including NGC 6302. It was concluded by the authors however, that no X-ray emission was detected in this source.

To summarise, the main points identified in this work are;

- A number of molecular species has been observed in NGC 6302 including HCN, HCO^+, CN and ^{13}CN, along with a number of species not typically observed in PN, such as ^{13}CS, SiO and N_2H^+. Tentative detections of $^{29}SiC_2$ and $Si^{13}CC$ have also been observed.

- An indication of outflows within NGC 6302 is highlighted by broadened HCN

and HCO^+ emission.

- SiO emission could be the product of maser emission, however further observations are required to confirm this suggestion. Analysis of the emission with better angular resolution or with increased frequency resolution (to determine the time variation of the spectrum) are two possible methods to ascertain the emission mechanism.

- Observed column densities for most molecular species correlate closely with modelled column densities constructed using the Meudon code. Of the various environments modelled, standard models and dense-cloud models compare most favourably with the majority of observed column densities. Deviations between standard models and X-ray enhanced modelled column densities are not significantly different.

- Reaction pathways in dense-cloud models differ significantly than those of standard models due to greater temperatures at larger A_V.

- The identification of water ice and gas-phase water in NGC 6302 (by Molster et al. (2001) and Bujarrabal et al. (2012) respectively), does not contribute to increased HCO^+ abundances through enhanced H_2O reactions.

- The $^{12}C/^{13}C$ ratio obtained from the $^{12}CN/^{13}CN$ column density calculations in this work, is 18.9 ($\pm$ 10). This figure is four higher than that calculated by Peretto et al. (2007) for NGC 6302 and over four times higher than the The Red Spider Nebula recently measured by Edwards and Ziurys (2013).

- Gas phase H_2O in circumstellar envelopes (CSEs) is produced by reaction OH + $H_2 \rightarrow H_2O$ + H. However in PN, H_2O is primarily formed via $H_3O^+ + e^-$ in standard models. In dense-cloud models, H_2O is primarily formed via the same reaction found in CSEs.

- SO_2 could be a potential tracer of nitrogen rich, dense-cloud regions at a low A_V.

- The models predict that whilst X-rays do enhance column densities for certain species (HCO^+ and N_2H^+ for example), X-rays have yet to influence the chemistry in the torus of NGC 6302.

6.5 Future Work

The integrated intensity maps presented in this work, have yielded significant information as to the excitation mechanisms involved in producing extended emission for a number of species. Equally, spatial distributions of compact emission for other species, has provided an insight as to the nature of the molecular species in question. It is clear that whilst an optically thick torus fosters the growth of the molecules observed here, some species thrive in regions of extreme excitation. However, whilst species observed in this work have contributed to existing knowledge on molecular behaviour in PN, full molecular surveys of planetary nebula are rare and hence the limited "trends" identified in previous papers have remained trends, due to the lack of comprehensive observations to contradict otherwise. This is slowly being addressed with recent observations such as The Red Spider Nebula by Edwards and Ziurys (2013), who suggest that molecular species not observed previously are not dependant on the evolutionary stage of the object, but prosper due to inherent properties of the physical and chemical conditions in the nebula. Further high resolution observations are required to continue our understanding of molecular survival and formation within PN which harbour a central torii. Physical conditions in the neutral gas within PN change rapidly during formation, the increased resolution at millimeter wavelengths obtained with ALMA, however, will not only transform our view of molecular formation and survival in objects such as these, but will also provide direct imaging of the dust condensation zone for AGB stars. Consequently, the detailed study of photochemistry in these environments permitted with ALMA, will revolutionise our view of objects such as OH231.8+4.2, an early-type PPN recently observed to contain OH masers (Leal-Ferreira et al. 2012), as it evolves to the nascent stages of a PN.

The Meudon models constructed in this work show that X-rays have not yet influenced the molecular chemistry within the torus of NGC 6302. XDR modelling in PN environments is still in its infancy, with the majority of models focusing on a few common molecular species and a select subset of PN. However, the identification of a number of suitable objects for further analysis has been improved by a recent study conducted by Kastner et al. (2012). In the *Chandra* Planetary Nebula Survey (ChanPlaNS) of 35 PN, the authors established that molecule-poor, elliptical nebulae are more likely to display X-ray emission (either diffuse or point-like) than molecule-rich, ring-like or bipolar nebulae. One or two PN (NGC 6445 for example) who have been observed with X-ray emission, have also been identified with a bright central ring or torus. Molecular surveys on a number of these objects both with and without X-ray emission could increase our understanding of the affects of an X-ray flux on the chemistry within PN.

PAH emission is destroyed by strong UV radiation but PAH emission has been identified in NGC 6302 within the bipolar lobes, however a local (PAH) peak is present near the northern spur (Matsuura et al. 2005). It is possible that the precursors to PAHs are present in or close to the torus of NGC 6302 and have yet to be observed. Benzene (C_6H_6), the smallest aromatic hydrocarbon and perhaps a foundering component in PAH formation has been observed in the dense torus of CRL 618 (Woods and Willacy 2007). The formation of gas phase benzene is dependant on differing physical and chemical environments; in the highly ionised region of CRL 618 for example, reactions with acetylene (C_2H_2) and various ions, HCO^+, $C_2H_3^+$ and $C_2H_2^+$ are stipulated as the probable formation route (Woods and Willacy 2007). As PAH's have already been detected in NGC 6032 and so now has HCO^+, it would help ascertain whether production of benzene in PN's is a common occurrence or specific to certain PN's. If detected the extent of other aromatic species could be identified and specific PAH's could be inferred in NGC 6302's expanding torus.

Part I

Appendices

Appendix A

First Appendix

A.1 Observations Continued

Displayed below (Fig A.1) is the spectrum of a tentative detection of $^{29}SiC_2$ (J = 10 − 9). Despite the low signal to noise, an integrated intensity map was produced by integrating just two channels over a velocity range of V_{LSR} = -44 to -42 km s^{-1} and is displayed in Figure A.2. It can be seen that the peak of emission for $^{29}SiC_2$ is not coincident with ^{12}CO medium velocity component but lies to the east, in the direction of the eastern bipolar lobe. The extended emission is elongated westwards towards the brightest ^{12}CO, however, the $^{29}SiC_2$ emission in general does not correlate with the structure of the ^{12}CO medium velocity component and appears to originate from the eastern bipolar lobe.

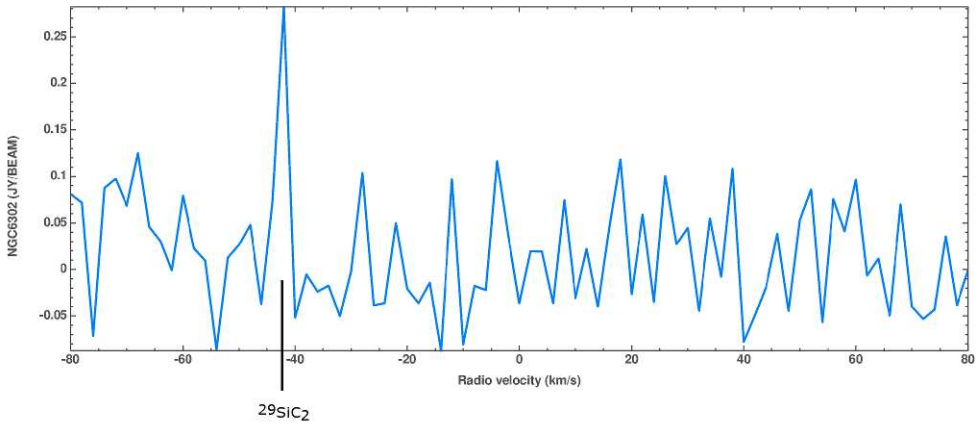

Figure A.1: $^{29}SiC_2$ (J = 10 − 9) spectrum showing the low signal to noise of this species. As with all other species, the spectrum for $^{29}SiC_2$ is obtained from the central pixel located within the brightest region, i.e the peak of emission. The main peak is centred around -42 km s^{-1}.

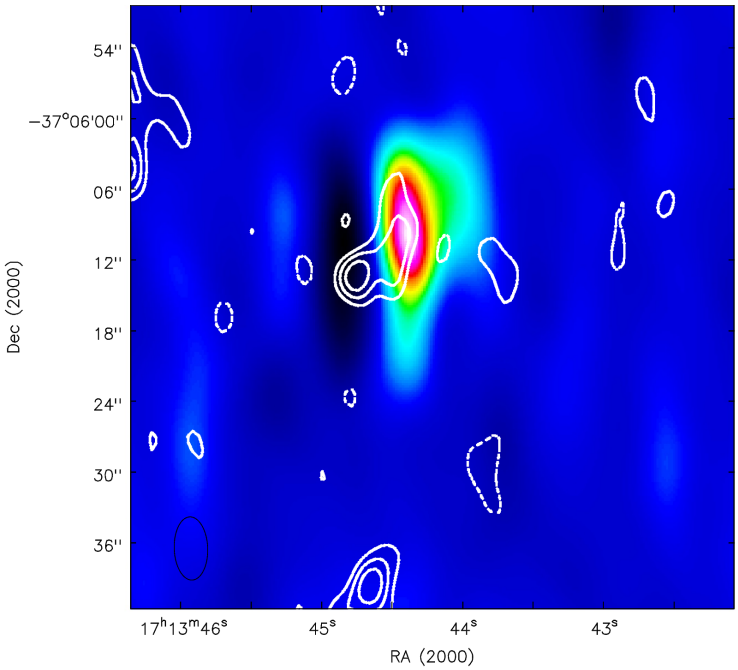

Figure A.2: $^{29}SiC_2$ (J = 10 − 9) medium velocity component integrated intensity map (contours) overlaid on ^{12}CO medium velocity component integrated intensity map (colours). The $^{29}SiC_2$ integrated intensity map spans just two channels in a velocity range of -44 to -42 km s^{-1} with a peak value of 0.714 (K km s^{-1}). Contours are from 40 to 80% in steps of 20% of the peak value. Negative contours are in dashed lines and are at -40% of the main peak value.

References

H. Abgrall, E. Roueff, and I. Drira. Total transition probability and spontaneous radiative dissociation of B, C, B' and D states of molecular hydrogen. *A&AS*, 141: 297–300, January 2000. doi: 10.1051/aas:2000121.

M. Agúndez, J. Cernicharo, and M. Guélin. Photochemistry in the Inner Layers of Clumpy Circumstellar Envelopes: Formation of Water in C-rich Objects and of C-bearing Molecules in O-rich Objects. *ApJL*, 724:L133–L136, December 2010. doi: 10.1088/2041-8205/724/2/L133.

M. Akyilmaz, D. R. Flower, P. Hily-Blant, G. Pineau Des Forêts, and C. M. Walmsley. The depletion of NO in pre-protostellar cores. *A&A*, 462:221–230, January 2007. doi: 10.1051/0004-6361:20066131.

I. Aleman and R. Gruenwald. H_2 infrared line emission from the ionized region of planetary nebulae. *A&A*, 528:A74, April 2011. doi: 10.1051/0004-6361/201014978.

A. Ali, O. M. Shalabiea, M. S. El-Nawawy, and T. J. Millar. Gas-phase models for the evolved planetary nebulae NGC 6781, M4-9 and NGC 7293. *MNRAS*, 325:881–885, August 2001. doi: 10.1046/j.1365-8711.2001.04513.x.

L. H. Aller, J. E. Ross, B. J. Omara, and C. D. Keyes. A spectroscopic study of the high excitation nebula NGC 6302. *MNRAS*, 197:95–106, October 1981.

M. C. B. Ashley and A. R. Hyland. Detection of highly ionized silicon in the planetary nebulae NGC 6302 and NGC 6537. *ApJ*, 331:532–538, August 1988. doi: 10.1086/166578.

R. Bachiller. Molecular observations of shocks and outflows. In E. F. van Dishoeck, editor, *Molecules in Astrophysics: Probes & Processes*, volume 178 of *IAU Symposium*, page 103, 1996.

R. Bachiller, T. Forveille, P. J. Huggins, and P. Cox. The chemical evolution of planetary nebulae. *A&A*, 324:1123–1134, August 1997.

E. L. O. Bakes and A. G. G. M. Tielens. The photoelectric heating mechanism for very small graphitic grains and polycyclic aromatic hydrocarbons. *ApJ*, 427:822–838, June 1994. doi: 10.1086/174188.

M. J. Barlow. in Flower D. R., ed.,. In Kluwer and Dordrecht, editors, *Planetary Nebulae*, volume 103 of *IAU Symposium*, page 105, 1983.

D. A. Beintema and S. R. Pottasch. The ISO spectrum of the planetary nebula NGC 6302. I. Observations. *A&A*, 347:942–948, July 1999.

J. H. Black. Molecules in planetary nebulae. *ApJ*, 222:125–131, May 1978. doi: 10.1086/156128.

V. Bujarrabal, J. Alcolea, R. Soria-Ruiz, P. Planesas, D. Teyssier, J. Cernicharo, L. Decin, C. Dominik, K. Justtanont, A. de Koter, A. P. Marston, G. Melnick, K. M. Menten, D. A. Neufeld, H. Olofsson, M. Schmidt, F. L. Schöier, R. Szczerba, and L. B. F. M. Waters. Herschel/HIFI observations of molecular emission in proto-planetary nebulae and young planetary nebulae. *A&A*, 537:A8, January 2012. doi: 10.1051/0004-6361/201117646.

B. F. Burke and F. Graham-Smith. *An Introduction to Radio Astronomy: Second Edition*. April 2002.

J. A. Cardelli and G. C. Clayton. Absolute extinction and the influence of environment - Dark cloud sight lines toward VCT 10, 30, and Walker 67. *AJ*, 101:1021–1032, March 1991. doi: 10.1086/115744.

J. A. Cardelli, G. C. Clayton, and J. S. Mathis. The relationship between infrared, optical, and ultraviolet extinction. *ApJ*, 345:245–256, October 1989. doi: 10.1086/167900.

S. Casassus, P. F. Roche, and M. J. Barlow. The coronal line regions of planetary nebulae NGC 6302 and 6537: 3-13μm grating and echelle spectroscopy. *MNRAS*, 314:657–671, June 2000. doi: 10.1046/j.1365-8711.2000.03208.x.

P. Caselli, C. M. Walmsley, A. Zucconi, M. Tafalla, L. Dore, and P. C. Myers. Molecular Ions in L1544. II. The Ionization Degree. *ApJ*, 565:344–358, January 2002. doi: 10.1086/324302.

I. Cherchneff. Water in IRC+10216: a genuine formation process by shock-induced chemistry in the inner wind. *A&A*, 526:L11, February 2011. doi: 10.1051/0004-6361/201016035.

P. Cox, A. Omont, P. J. Huggins, R. Bachiller, and T. Forveille. Chemistry in the

molecular envelopes of the planetary nebulae NGC 6072 and IC 4406. *A&A*, 266: 420–428, December 1992.

L. Decin, M. Agúndez, M. J. Barlow, F. Daniel, J. Cernicharo, R. Lombaert, E. De Beck, P. Royer, B. Vandenbussche, R. Wesson, E. T. Polehampton, J. A. D. L. Blommaert, W. De Meester, K. Exter, H. Feuchtgruber, W. K. Gear, H. L. Gomez, M. A. T. Groenewegen, M. Guélin, P. C. Hargrave, R. Huygen, P. Imhof, R. J. Ivison, C. Jean, C. Kahane, F. Kerschbaum, S. J. Leeks, T. Lim, M. Matsuura, G. Olofsson, T. Posch, S. Regibo, G. Savini, B. Sibthorpe, B. M. Swinyard, J. A. Yates, and C. Waelkens. Warm water vapour in the sooty outflow from a luminous carbon star. *Nature*, 467: 64–67, September 2010. doi: 10.1038/nature09344.

C. Dijkstra, C. Dominik, S. N. Hoogzaad, A. de Koter, and M. Min. Water ice growth around evolved stars. *A&A*, 401:599–611, April 2003. doi: 10.1051/0004-6361:20030102.

C. Dijkstra, C. Dominik, J. Bouwman, and A. de Koter. Water ice growth around evolved stars. II. Modeling infrared spectra. *A&A*, 449:1101–1116, April 2006. doi: 10.1051/0004-6361:20054053.

Dinh-V-Trung, V. Bujarrabal, A. Castro-Carrizo, J. Lim, and S. Kwok. Massive Expanding Torus and Fast Outflow in Planetary Nebula NGC 6302. *ApJ*, 673:934–941, February 2008. doi: 10.1086/524373.

B. T. Draine. Photoelectric heating of interstellar gas. *ApJS*, 36:595–619, April 1978. doi: 10.1086/190513.

B. T. Draine and H. M. Lee. Optical properties of interstellar graphite and silicate grains. *ApJ*, 285:89–108, October 1984. doi: 10.1086/162480.

B. T. Draine, W. G. Roberge, and A. Dalgarno. Magnetohydrodynamic shock waves in molecular clouds. *ApJ*, 264:485–507, January 1983. doi: 10.1086/160617.

J. L. Edwards and L. M. Ziurys. The Remarkable Molecular Content of the Red Spider Nebula (NGC6537). *ApJL*, 770:L5, June 2013. doi: 10.1088/2041-8205/770/1/L5.

K. H. Elliott and J. Meaburn. Line profiles from the ionized and neutral gas in the peculiar nebula NGC 6302. *MNRAS*, 181:499–507, November 1977.

D. Emerson. *Interpreting Astronomical Spectra*. June 1996.

S. R. Federman, A. E. Glassgold, and J. Kwan. Atomic to molecular hydrogen transition in interstellar clouds. *ApJ*, 227:466–473, January 1979. doi: 10.1086/156753.

E. L. Fitzpatrick and D. Massa. An analysis of the shapes of ultraviolet extinction

curves. III - an atlas of ultraviolet extinction curves. *ApJS*, 72:163–189, January 1990. doi: 10.1086/191413.

B. P. Flannery, W. Roberge, and G. B. Rybicki. The penetration of diffuse ultraviolet radiation into interstellar clouds. *ApJ*, 236:598–608, March 1980. doi: 10.1086/157778.

J. R. Goicoechea and J. Le Bourlot. The penetration of Far-UV radiation into molecular clouds. *A&A*, 467:1–14, May 2007. doi: 10.1051/0004-6361:20066119.

M. Gonzalez Garcia, J. Le Bourlot, F. Le Petit, and E. Roueff. Radiative transfer revisited for emission lines in photon dominated regions. *A&A*, 485:127–136, July 2008. doi: 10.1051/0004-6361:200809440.

W. Gordy and R.L Cook. *Microwave Molecular Spectra (3rd Edition)*. 1984.

B. Groves, M. A. Dopita, R. E. Williams, and C.-T. Hua. The Internal Extinction Curve of NGC 6302 and its Extraordinary Spectrum. , 19:425–442, 2002. doi: 10.1071/AS02010.

T. W. Hartquist, A. Dalgarno, and M. Oppenheimer. Molecular diagnostics of interstellar shocks. *ApJ*, 236:182–188, February 1980. doi: 10.1086/157731.

T. Hasegawa, K. Volk, and S. Kwok. A Chemical Model of the Neutral Envelope of the Planetary Nebula NGC 7027. *ApJ*, 532:994–1005, April 2000. doi: 10.1086/308610.

M. G. Hoare, P. F. Roche, and R. E. S. Clegg. Millimetre and submillimetre continuum observations of planetary nebulae. *MNRAS*, 258:257–269, September 1992.

D. A. Howe, T. J. Millar, and D. A. Williams. Chemistry in a protoplanetary nebula. *MNRAS*, 255:217–226, March 1992.

D. A. Howe, T. W. Hartquist, and D. A. Williams. Molecules in Dense Globules in Planetary Nebulae. *MNRAS*, 271:811, December 1994.

Z.-Y. Huang, T. I. Hasegawa, Dinh-V-Trung, S. Kwok, S. Muller, N. Hirano, J. Lim, C. Muthu Mariappan, and A. Lyo. Detection of Multiple Bipolar Flows in NGC 7027 with Submillimeter Array. *ApJ*, 722:273–280, October 2010. doi: 10.1088/0004-637X/722/1/273.

S. Huettemeister, G. Dahmen, R. Mauersberger, C. Henkel, T. L. Wilson, and J. Martin-Pintado. Molecular gas in the Galactic center region. III. Probing shocks in molecular cores. *A&A*, 334:646–658, June 1998.

P. J. Huggins, R. Bachiller, P. Cox, and T. Forveille. CO in the cometary globules of

the Helix nebula. *ApJL*, 401:L43–L46, December 1992. doi: 10.1086/186666.

P. J. Huggins, R. Bachiller, P. Cox, and T. Forveille. The molecular envelopes of planetary nebulae. *A&A*, 315:284–302, November 1996.

W. T. Huntress, Jr. and V. G. Anicich. Laboratory studies of ion-neutral reactions in interstellar regions - Gas-phase equilibrium between HCN and NH3 in dense clouds. *ApJ*, 208:237–244, August 1976. doi: 10.1086/154600.

W. T. Huntress, Jr., V. G. Anicich, M. J. McEwan, and Z. Karpas. Laboratory studies of some of the major ion-molecule reactions occurring in cometary comae. *ApJS*, 44:481–488, December 1980. doi: 10.1086/190701.

D. Johnstone, E. Rosolowsky, M. Tafalla, and H. Kirk. Dense Gas Tracers in Perseus: Relating the N_2H^+, NH_3, and Dust Continuum Properties of Pre- and Protostellar Cores. *ApJ*, 711:655–670, March 2010. doi: 10.1088/0004-637X/711/2/655.

E. Josselin and R. Bachiller. The chemistry of compact planetary nebulae. *A&A*, 397: 659–666, January 2003. doi: 10.1051/0004-6361:20021516.

K. Justtanont, L. Decin, F. L. Schöier, M. Maercker, H. Olofsson, V. Bujarrabal, A. P. Marston, D. Teyssier, J. Alcolea, J. Cernicharo, C. Dominik, A. de Koter, G. Melnick, K. Menten, D. Neufeld, P. Planesas, M. Schmidt, R. Szczerba, R. Waters, T. de Graauw, N. Whyborn, T. Finn, F. Helmich, O. Siebertz, F. Schmülling, V. Ossenkopf, and R. Lai. A HIFI preview of warm molecular gas around χ Cygni: first detection of H_2O emission toward an S-type AGB star. *A&A*, 521:L6, October 2010. doi: 10.1051/0004-6361/201015092.

K. Justtanont, T. Khouri, M. Maercker, J. Alcolea, L. Decin, H. Olofsson, F. L. Schöier, V. Bujarrabal, A. P. Marston, D. Teyssier, J. Cernicharo, C. Dominik, A. de Koter, G. Melnick, K. M. Menten, D. Neufeld, P. Planesas, M. Schmidt, R. Szczerba, and R. Waters. Herschel/HIFI observations of O-rich AGB stars: molecular inventory. *A&A*, 537:A144, January 2012. doi: 10.1051/0004-6361/201117524.

J. H. Kastner. X-ray Emission from Planetary Nebulae and their Central Stars: a Status Report. In *Asymmetrical Planetary Nebulae IV*, June 2007.

J. H. Kastner, R. Montez, Jr., B. Balick, D. J. Frew, B. Miszalski, R. Sahai, E. Blackman, Y.-H. Chu, O. De Marco, A. Frank, M. A. Guerrero, J. A. Lopez, V. Rapson, A. Zijlstra, E. Behar, V. Bujarrabal, R. L. M. Corradi, J. Nordhaus, Q. A. Parker, C. Sandin, D. Schönberner, N. Soker, J. L. Sokoloski, M. Steffen, T. Ueta, and E. Villaver. The Chandra X-Ray Survey of Planetary Nebulae (CHANPLANS):

Probing Binarity, Magnetic Fields, and Wind Collisions. *AJ*, 144:58, August 2012. doi: 10.1088/0004-6256/144/2/58.

K. I. Kellermann and G. L. Verschuur. *Galactic and extragalactic radio astronomy (2nd edition)*. 1988.

F. Kemper, F. J. Molster, C. Jäger, and L. B. F. M. Waters. The mineral composition and spatial distribution of the dust ejecta of NGC 6302. *A&A*, 394:679–690, November 2002. doi: 10.1051/0004-6361:20021119.

R. K. Kimura, R. Gruenwald, and I. Aleman. Molecular chemistry and the missing mass problem in planetary nebulae. *A&A*, 541:A112, May 2012. doi: 10.1051/0004-6361/201118429.

R. L. Kingsburgh and M. J. Barlow. Elemental abundances for a sample of southern galctic planetary nebulae. *MNRAS*, 271:257–299, November 1994.

S. Kwok. *The Origin and Evolution of Planetary Nebulae*. August 2007.

S. Kwok. Molecular Evolution from AGB Stars to Planetary Nebulae. In J. Cernicharo and R. Bachiller, editors, *IAU Symposium*, volume 280 of *IAU Symposium*, pages 203–215, December 2011. doi: 10.1017/S1743921311024987.

N. J. Lame and G. J. Ferland. NGC 6302 - Ionized by a very hot star or by a wind? *ApJ*, 367:208–212, January 1991. doi: 10.1086/169619.

A. Laor and B. T. Draine. Spectroscopic constraints on the properties of dust in active galactic nuclei. *ApJ*, 402:441–468, January 1993. doi: 10.1086/172149.

F. Le Petit, C. Nehmé, J. Le Bourlot, and E. Roueff. A Model for Atomic and Molecular Interstellar Gas: The Meudon PDR Code. *ApJS*, 164:506–529, June 2006. doi: 10.1086/503252.

M. L. Leal-Ferreira, W. H. T. Vlemmings, P. J. Diamond, A. Kemball, N. Amiri, and J.-F. Desmurs. Rotten Egg nebula: the magnetic field of a binary evolved star. *A&A*, 540:A42, April 2012. doi: 10.1051/0004-6361/201118303.

G. A. Mamon, A. E. Glassgold, and A. Omont. Photochemistry and molecular ions in oxygen-rich circumstellar envelopes. *ApJ*, 323:306–315, December 1987. doi: 10.1086/165828.

J. Martin-Pintado, P. de Vicente, A. Fuente, and P. Planesas. SiO Emission from the Galactic Center Molecular Clouds. *ApJL*, 482:L45, June 1997. doi: 10.1086/310691.

J. S. Mathis. Dust Models with Tight Abundance Constraints. *ApJ*, 472:643, December

1996. doi: 10.1086/178094.

J. S. Mathis, W. Rumpl, and K. H. Nordsieck. The size distribution of interstellar grains. *ApJ*, 217:425–433, October 1977. doi: 10.1086/155591.

M. Matsuura, A. A. Zijlstra, F. J. Molster, L. B. F. M. Waters, H. Nomura, R. Sahai, and M. G. Hoare. The dark lane of the planetary nebula NGC 6302*†. *MNRAS*, 359 : 383 – −400, *May*2005. *doi* : 10.1111/ *j*.1365 – 2966.2005.08903.*x*.

J. Meaburn and J. R. Walsh. Direct evidence for an energetic stellar wind in NGC 6302. *MNRAS*, 191:5P–11P, April 1980.

J. Meaburn, J. A. López, W. Steffen, M. F. Graham, and A. J. Holloway. The Hubble-Type Outflows from the High-Excitation, Polypolar Planetary Nebula NGC 6302. *AJ*, 130:2303–2311, November 2005. doi: 10.1086/496978.

R. Meijerink and M. Spaans. Diagnostics of irradiated gas in galaxy nuclei. I. A far-ultraviolet and X-ray dominated region code. *A&A*, 436:397–409, June 2005. doi: 10.1051/0004-6361:20042398.

R. Meijerink, M. Spaans, and F. P. Israel. Irradiated ISM: Discriminating between Cosmic Rays and X-Rays. *ApJL*, 650:L103–L106, October 2006. doi: 10.1086/508938.

R. Meijerink, M. Spaans, and F. P. Israel. Diagnostics of irradiated dense gas in galaxy nuclei. II. A grid of XDR and PDR models. *A&A*, 461:793–811, January 2007. doi: 10.1051/0004-6361:20066130.

R. Meijerink, S. Cazaux, and M. Spaans. Enhanced H_2O formation through dust grain chemistry in X-ray exposed environments. *A&A*, 537:A102, January 2012. doi: 10.1051/0004-6361/201117700.

R. Minkowski and H. M. Johnson. The Peculiar Nebula NGC 6302. *ApJ*, 148:659, May 1967. doi: 10.1086/149188.

F. J. Molster, T. L. Lim, R. J. Sylvester, L. B. F. M. Waters, M. J. Barlow, D. A. Beintema, M. Cohen, P. Cox, and B. Schmitt. The complete ISO spectrum of NGC 6302. *A&A*, 372:165–172, June 2001. doi: 10.1051/0004-6361:20010465.

T. J. T. Moore, S. L. Lumsden, N. A. Ridge, and P. J. Puxley. The near-infrared extinction law in regions of high A_V. *MNRAS*, 359:589–596, May 2005. doi: 10.1111/j.1365-2966.2005.08923.x.

A. Natta and D. Hollenbach. The evolution of the neutral gas in planetary nebulae: theoretical models. *A&A*, 337:517–538, September 1998.

L.-A. Nyman, P. J. Hall, and H. Olofsson. SiO masers in OH/IR stars, proto-

planetary and planetary nebulae. *A&AS*, 127:185–200, January 1998. doi: 10.1051/aas:1998343.

F. Palla, R. Bachiller, L. Stanghellini, M. Tosi, and D. Galli. Measurements of $^{12}C/^{13}C$ in planetary nebulae: Implications on stellar and Galactic chemical evolution. *A&A*, 355:69–78, March 2000.

H. E. Payne, J. A. Phillips, and Y. Terzian. A young planetary nebula with OH molecules - NGC 6302. *ApJ*, 326:368–375, March 1988. doi: 10.1086/166098.

M. Peimbert and S. Torres-Peimbert. Type I planetary nebulae. In D. R. Flower, editor, *Planetary Nebulae*, volume 103 of *IAU Symposium*, pages 233–241, 1983.

N. Peretto, G. Fuller, A. Zijlstra, and N. Patel. The massive expanding molecular torus in the planetary nebula NGC 6302. *A&A*, 473:207–217, October 2007. doi: 10.1051/0004-6361:20066973.

R. A. Perley, F. R. Schwab, A. H. Bridle, and R. D. Ekers. *Synthesis imaging. Course notes from an NRAO summer school, held at Socorro, New Mexico, USA, 5 - 9 August 1985*. 1986.

S. R. Pottasch and D. A. Beintema. The ISO spectrum of the planetary nebula NGC 6302. II. Nebular abundances. *A&A*, 347:975–982, July 1999.

D. Prialnik. *An Introduction to the Theory of Stellar Structure and Evolution*. October 2009.

M. P. Redman, S. Viti, P. Cau, and D. A. Williams. Chemistry and clumpiness in planetary nebulae. *MNRAS*, 345:1291–1296, November 2003. doi: 10.1046/j.1365-2966.2003.07047.x.

W. G. Roberge. The spherical harmonics solution for the radiation field in plane-parallel clouds with embedded sources. *ApJ*, 275:292–306, December 1983. doi: 10.1086/161533.

R. Sahai, A. Wootten, H. E. Schwarz, and W. Wild. Multiple outflows in the bipolar planetary nebula M1-16: A molecular line study. *ApJ*, 428:237–249, June 1994. doi: 10.1086/174235.

A. H. Saleck, R. Simon, and G. Winnewisser. Interstellar CN rotational spectra: (12)C(15)N. *ApJ*, 436:176–182, November 1994. doi: 10.1086/174890.

E. Sarrasin, D. B. Abdallah, M. Wernli, A. Faure, J. Cernicharo, and F. Lique. The rotational excitation of HCN and HNC by He: new insights on the HCN/HNC abundance ratio in molecular clouds. *MNRAS*, 404:518–526, May 2010. doi:

10.1111/j.1365-2966.2010.16312.x.

C. Savage, A. J. Apponi, L. M. Ziurys, and S. Wyckoff. Galactic $^{12}C/^{13}C$ Ratios from Millimeter-Wave Observations of Interstellar CN. *ApJ*, 578:211–223, October 2002. doi: 10.1086/342468.

R. Simon. *Multiline CN Observations of Star Forming Regions*. 1997.

R. Simon, J. Stutzki, A. Sternberg, and G. Winnewisser. Chemical stratification in the Orion Bar region: CN and CS submillimeter observations. *A&A*, 327:L9–L12, November 1997.

A. Sternberg. PDRs and XDRs: Theory and Observations. In D. C. Lis, G. A. Blake, and E. Herbst, editors, *Astrochemistry: Recent Successes and Current Challenges*, volume 231 of *IAU Symposium*, pages 141–152, August 2005. doi: 10.1017/S1743921306007137.

A. Sternberg and A. Dalgarno. Chemistry in Dense Photon-dominated Regions. *ApJS*, 99:565, August 1995. doi: 10.1086/192198.

C. Szyszka, J. R. Walsh, A. A. Zijlstra, and Y. G. Tsamis. Detection of the Central Star of the Planetary Nebula NGC 6302. *ApJL*, 707:L32–L36, December 2009. doi: 10.1088/0004-637X/707/1/L32.

A. G. G. M. Tielens. *The Physics and Chemistry of the Interstellar Medium*. August 2005.

A. G. G. M. Tielens and D. Hollenbach. Photodissociation regions. I - Basic model. II - A model for the Orion photodissociation region. *ApJ*, 291:722–754, April 1985. doi: 10.1086/163111.

J. C. Weingartner and B. T. Draine. Dust Grain-Size Distributions and Extinction in the Milky Way, Large Magellanic Cloud, and Small Magellanic Cloud. *ApJ*, 548: 296–309, February 2001. doi: 10.1086/318651.

K. Willacy and I. Cherchneff. Silicon and sulphur chemistry in the inner wind of IRC+10216. *A&A*, 330:676–684, February 1998.

J. Woodall, M. Agúndez, A. J. Markwick-Kemper, and T. J. Millar. The UMIST database for astrochemistry 2006. *A&A*, 466:1197–1204, May 2007. doi: 10.1051/0004-6361:20064981.

P. M. Woods and K. Willacy. Benzene Formation in the Inner Regions of Protostellar Disks. *ApJL*, 655:L49–L52, January 2007. doi: 10.1086/511680.

N. J. Wright, M. J. Barlow, B. Ercolano, and T. Rauch. A 3D photoionization model of

the extreme planetary nebula NGC 6302. *MNRAS*, 418:370–389, November 2011. doi: 10.1111/j.1365-2966.2011.19490.x.

M. Yan, S. R. Federman, A. Dalgarno, and J. E. Bjorkman. Theoretical Modeling of ISO Results on Planetary Nebula NGC 7027. *ApJ*, 515:640–648, April 1999. doi: 10.1086/307047.

Y. Zhang, S. Kwok, and Dinh-V-Trung. A Spectral Line Survey of NGC 7027 at Millimeter Wavelengths. *ApJ*, 678:328–346, May 2008. doi: 10.1086/529428.

L. M. Ziurys, P. Friberg, and W. M. Irvine. Interstellar SiO as a tracer of high-temperature chemistry. *ApJ*, 343:201–207, August 1989. doi: 10.1086/167696.